Dissertation zur Erlangung des Doktorgrades der
Fakultät für Chemie und Pharmazie
der Ludwig-Maximilians-Universität München

SSNA-1 self-assembly regulates centriole formation

Lorenzo Agostini

aus

Giulianova, Italy

2024

Erklärung

Diese Dissertation wurde im Sinne von § 7 der Promotionsordnung vom 28. November 2011 von Herrn Prof. Dr. Veit Hornung betreut.

Eidesstattliche Versicherung

Diese Dissertation wurde eigenständig und ohne unerlaubte Hilfe erarbeitet.

München, 22/02/2024

_____
Lorenzo Agostini

Dissertation eingereicht am: 29/02/2024

1. Gutachterin / 1. Gutachter: Prof. Dr. Veit Hornung

2. Gutachterin / 2. Gutachter: Prof. Dr. Elena Conti

Mündliche Prüfung am: 25/07/2024

Table of Contents

1 Summary *6*

2 Introduction *8*

2.1 Microtubules (MTs) and microtubule-binding proteins (MTBPs) **8**

2.1.1 Microtubule dynamics **8**

2.1.2 Regulators of microtubules **10**

2.1.3 Lattice binding proteins **10**

2.1.4 Plus-end tracking proteins (+TIPs) **11**

2.1.5 Minus-end tracking proteins (-TIPs) **13**

2.2 Microtubule organizing centers (MTOCs) **16**

2.2.1 Centrosome **16**

2.2.2 Cilia, flagella, and basal bodies **22**

2.3 Additional MTOCs and/or microtubule-based structures **23**

2.3.1 Mitotic spindle **23**

2.3.2 Midbody **23**

2.4 Sjögren's syndrome nuclear autoantigen 1 (SSNA1) **23**

..... **24**

2.5 Transmission electron microscopy in structural biology **27**

2.5.1 Negative staining EM, and cryo-EM for single particle analysis **28**

3 Aim of the thesis *31*

4 Materials and methods *32*

4.1 Laboratory equipment **32**

4.2 Genes preparation **33**

4.3 Protein preparation and purification **37**

4.4 Protein sequences alignment and structural prediction **40**

4.5 Protein characterization through negative staining, and cryo-electron microscopy **40**

4.5.1 Negative staining electron microscopy **40**

4.5.2 Cryo-EM sample preparation, data collection, and image processing **40**

4.5.3 Model building **42**

4.6 Sedimentation assay **42**

4.7 Circular dichroism (CD) spectroscopy **43**

4.8 Dynamic light scattering (DLS) **44**

4.9 *C. elegans* strain preparation, and maintenance **44**

4.9.1 CRISPR-Cas9 genome editing **44**

4.10 Embryonic viability assay **44**

4.11 Fixed and live imaging 45

5 Results ***48***

5.1 SSNA-1 (*C. elegans*) shares high similarity with other homologues 48

5.2 Cryo-EM analysis of SSNA-1 reveals dimeric coiled-coils connecting through triple-stranded helical junctions 49

5.3 SSNA-1 head-to-tail self-assembly requires both N- and C-termini 56

5.5 SSNA-1 knock-out results in reduced viability and morphological defects in *C. elegans* embryos 62

5.6 SSNA-1 knock-out reveals cell division defects in *C. elegans*, with multipolar spindle being the most prevalent 63

5.6.1 Extra poles contain SPD-2, ZYG-1, and SAS-4 65

5.7 Mutations interfering with SSNA-1 oligomerization affect *C. elegans* viability 67

5.8 Microtubules and ZYG-1 bind SSNA-1 *in vitro* 68

5.9 SSNA-1 novel satellite-like structures reside at about 750 nm from the center of centrioles 72

5.10 SSNA-1 is a microtubule remodeling factor *in vitro* 73

5.11 SSNA-1 satellite-like phenotype appears to be microtubule dependent 76

6 Discussion ***78***

7 Outlook ***82***

8 References ***84***

Acknowledgements ***95***

1 Summary

SSNA1, also known as NA14 or DIP13, is a filamentous protein found in many eukaryotic species such as mammals, fishes, insects, protozoan parasites and green algae. It localizes at the so called MTOCs (microtubule organizing centers), including centrosomes as well as basal bodies, and it is characterized as microtubule remodeling factor. Although findings have described SSNA1 involvement in microtubule-based structures, the molecular mechanism underlying its polymer formation and how it regulates the centrosome remain unclear. In my PhD thesis, we report the molecular and genetic analyses of SSNA-1 (*C. elegans* homolog) using *in vitro* biochemical, biophysical, and structural biology approaches complemented with *in vivo* analyses in *C. elegans*.

Cryo-EM and AlphaFold prediction of SSNA-1 revealed a self-assembled filamentous structure in which every fibril is composed of antiparallel coiled-coils. The connection between individual coiled-coil dimers is made through an unusual triple-stranded coiled-coil that acts as polymerizing junction point. We found that the N-terminus of SSNA-1 is required for both microtubule binding and microtubule branching *in vitro*. Such activities were impaired when SSNA-1 lacked amino acids at the N-terminus which were required for its self-assembly. In contrast, C-terminal truncations that abolished self-assembly still retained microtubule binding. The point mutation analysis of SSNA-1 further validated its N-terminus as critical region for microtubule binding and microtubule branching activity. These insights collectively disclose the molecular mechanism of SSNA-1 self-assembly and indicate that SSNA-1 induced microtubule binding and branching activity do not rely on SSNA-1 self-assembly exclusively.

The functional analysis of SSNA-1 in *C. elegans* was conducted in collaboration with Dr. Jason Pfister and Dr. Kevin O'Connell at the Laboratory of Biochemistry & Genetics at the National Institute of Diabetes and Digestive and Kidney Diseases (NIH-NIDDK). In *C. elegans*, we find that SSNA-1 localization is restricted to centrioles during embryonic development's first cell cycle. The deletion of SSNA-1 or the loss of either 17 residues at N-terminus or 6 residues at the C-terminus, which were required for the formation of the filamentous bundles in vitro, triggered a significant decrease of embryonic viability, compared to wild-type worms. The phenotype analysis of viability reduced worms showed predominantly multipolar spindles defects, likely arising from centriole overduplication or fragmentation. We observed that the

absence of SSNA-1 altered centriolar composition in worms, such that centriole have less ZYG-1 and more SAS-6 protein levels. According to these observations, our in vitro analysis further characterized SSNA-1 as a binding protein of the Polo-like kinase ZYG-1. After the first cell cycle during embryonic development in *C. elegans*, we find that SSNA-1 becomes dynamic and it also localizes to novel satellite-like structures that surround the pericentriolar material (PCM). Point mutations at the SSNA-1 N-terminus, a region critically involved in microtubule recognition, abolished the formation of SSNA-1 satellites in vivo. The nematode strains carrying such point mutations of SSNA-1 didn't show decrease in viability compared to wild-type worms, suggesting that SSNA-1's role in regulating centriole biogenesis is relegated to its centriolar localization and those satellites might be involved in other roles. These insights collectively disclose that SSNA-1 self-assembly activity is required for the proper formation of centrioles, such as the correct number and/or molecular composition, ensuring spindle formation during embryonic development in *C. elegans*.

Taken together, our findings have led to new molecular insights of SSNA-1 acting as critical regulator of centriole formation and, therefore, we provided novel molecular basis of physiological processes occurring at the centrosome, an essential MTOC.

2 Introduction

2.1 Microtubules (MTs) and microtubule-binding proteins (MTBPs)

2.1.1 Microtubule dynamics

As cytoskeletal filaments, MTs are molecular machineries conserved throughout eukaryotes, including dividing and some differentiated cell types, and are involved in essential biological processes [1,2]. In non-dividing cells, MTs organize the cell architecture by positioning the nucleus and organelles contributing to cell polarity. They can act as a roadway for intracellular trafficking, as well as orchestrate the architecture of cilia and flagella facilitating cell motility. MTs are dynamic polymers that along with actin and intermediate filaments provide the backbone within the cytoplasm maintaining cell shape.

During cell division, the mitotic spindle is built by an array of dynamic MTs, which provide a mechanical influence over the segregation process [1]. In cells, MTs can be nucleated from the centrosome, which was originally thought to be the only MT organizing center (MTOC). However, emerging research has found that nucleation of MTs can occur in several other locations [3-13]. Notable examples of non-centrosomal MTOCs during cell division comprise MTs built from spindle MTs, the proximity of chromatin and kinetochores [3-6]. Other examples of non-centrosomal MTOCs during interphase comprise MTs that are formed from the Golgi apparatus, the plasma membrane, the nuclear envelope and/or pre-existing MTs [7-13].

In the last decades, microtubule-based structures have gained interest for their involvement in cancer, such as breast, lung, ovarian, prostate, and colorectal cancers, as well as neurological disorders like Alzheimer's diseases [14,15]. For instance, drugs like taxanes and vinca alkaloids target MTs to inhibit their dynamics, causing mitotic arrest and cell death in cancer cells. Hence, studying these molecular machineries is important to further understand the underlying biological mechanisms and ultimately create targeted therapies.

To regulate this variety of cellular processes, the assembly and orientation of MTs must be tightly organized [1,2,14,16]. The structure of MTs appears as hollow tubes that are characterized by 25 nm in diameter. The assembly of these filaments occurs by interactions between the α/β-tubulin heterodimer subunits (Figure 1.1). Specifically, linearly assembled protofilaments of such heterodimeric subunits align and form a sheet-like lattice that further folds itself to form a tubular structure. The microtubule lattice generally consists of two types of interactions.

While longitudinal interactions occur between tubulin heterodimers that make single protofilaments, the lateral interactions occur between different protofilaments [1,14,16]. The number of MT protofilaments that can be nucleated *in vitro* is between 9 and 17 [17 - 19], but in majority they consist of 14 protofilaments when using mammalian tubulin [19]. Despite a few exceptions, MTs created from centrosomes and axonemes, both *in vivo* and *in vitro*, predominantly consists of 13 protofilaments [1].

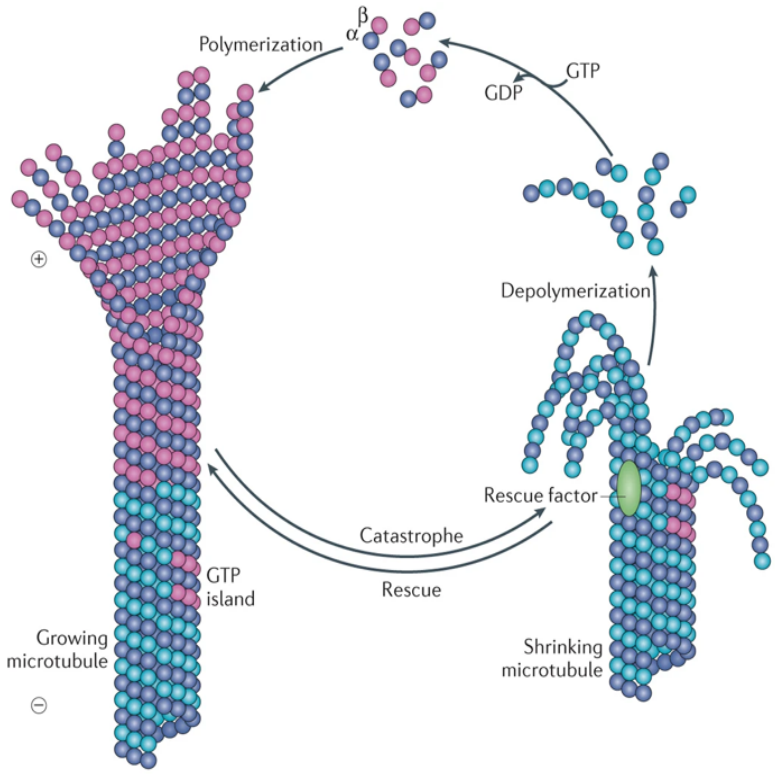

Figure 1.1| Polymerization and depolymerization of tubulin. The cycle is regulated with the hydrolysis of GTP. Image is adopted from Akhmanova and Steinmetz, 2015.

MTs are highly dynamic and to understand the mechanism by which they regulate the cells in space and time it is critical to know how they polymerize and depolymerize (Figure 1.1). MTs are polarized structures as α- and β-tubulin have opposite orientations during polymerization. These different orientations ultimately form MTs with β-tubulin at one end, the plus-end, and α-tubulin at the other end, the minus-end [1,14,16]. During polymerization of MTs, tubulin heterodimers containing GTP can be recruited at the plus-end. However, when the GTP of the β-tubulin is hydrolyzed to GDP MTs undergo shrinkage and depolymerization, leading to a process called catastrophe. In contrary, the GTP of α-tubulin can't be exchanged and it is not hydrolyzed. Therefore, the plus- and minus-ends of MTs have different dynamic properties [14]. In order to explain the dynamic instability of microtubules, researchers have proposed the GTP-cap model. In this model, MTs can grow when GTP-tubulin heterodimers are added at plus-

end and GTP isn't hydrolyzed, forming a stabilized GTP-cap. Contrarily, when GTP is hydrolyzed there is loss of the cap, leading to MT shrinkage and tubulin depolymerization (catastrophe). The presence of the GTP-cap maintains the MT structure through its lattice bonds. In opposite, the GTP hydrolysis triggers the weakening of lateral contacts between protofilaments by increasing the strain on lattice integrity, leading to a global lattice rearrangement. The shrinking process of MTs could occasionally be rescued by specific factors.

The dynamic instability of MTs can be used by cells to apply forces required for mechanical processes. It also enables MTs to explore the cytoplasm that contains other machineries, such as vesicles and organelles [14,16].

2.1.2 Regulators of microtubules

Inside the cell, the dynamic instability of MTs and how they dictate various processes are regulated by many proteins, which are called microtubule-binding proteins (MTBPs). MTBPs are widespread in all eukaryotes, others differ by organism and/or cell type. In addition, the term microtubule-associated proteins (MAPs) can be used to describe some MTBPs that co-sediment with MTs during cycles of MTs polymerization and depolymerization *in vitro* [20] (Figure 1.2).

MTBPs can be classified into many groups according to the cellular functions they control or how they interact with MTs [14]. The MTBPs are characterized on how they interact with MTs and are classified as lattice binding proteins, plus-end tracking proteins (+TIPs), and minus-end tracking proteins (-TIPs). Alternatively, the MTBPs characterized by activity are classified as stabilizers, destabilizers, bundlers and/or cross-linkers, capping proteins, and cytoskeletal integrators [14,20].

Here, we describe MTBPs classified on how they interact with MTs.

2.1.3 Lattice binding proteins

Lattice binding proteins interact with the surface of MTs, excluding the MT plus- and minus-ends [20]. Well studied proteins of this MTBP group are tau, MAP2 and MAP4, all contributing to the stability and dynamics of MTs. While the proteins tau (Figure 1.2) and MAP2 are present in neuronal cells and interact with MTs located at axons and dendrites, respectively, the protein

MAP4 can be found throughout many other cell types [21]. Other notable examples of proteins binding to MT lattices are spastin and katanin, which are considered MTs destabilizers that induce depolymerization and/or severing activities [22].

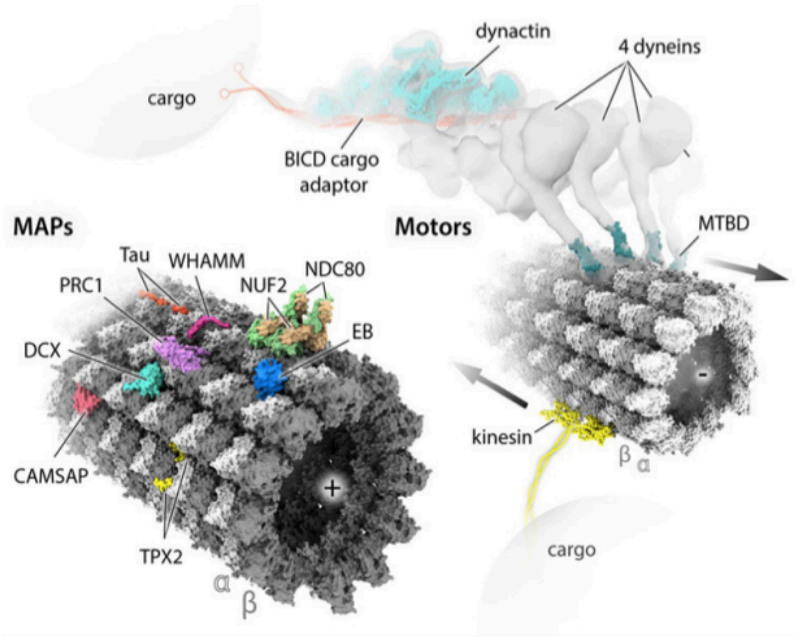

Figure 1.2| Notable examples of MAPs, including molecular motors. The image represents cryo-EM structures of MT lattices, MTBPs, MTs-binding polypeptide regions of MAPs, and molecular motors. Image is adopted from Szymon W. Manka et al, 2018.

2.1.4 Plus-end tracking proteins (+TIPs)

Another group of MTBPs is represented by the plus-end tracking proteins (+TIPs). This group of heterogeneous proteins dynamically track the growing plus-ends of MTs and regulate various cellular activities (Figure 1.3) [14,23,24]. +TIPs can act as "autonomous tip trackers" or "hitchhikers". While the "autonomous tip trackers" bind to the ends of MTs directly, the "hitchhikers" concentrates at the ends of MTs indirectly binding to an autonomous tip tracker. In addition, the +TIPs could be classified depending on the conserved structural elements that allow binding to those proteins with MTs or other +TIPs (Figure 1.3), ultimately contributing to the formation of intricate +TIPs networks.

The end-binding (EB) proteins are considered the master regulators of +TIPs networks. They interact with the growing ends of MTs tracking the GTP-cap [14,23,24]. Notable examples of EB proteins are EB1 and EB2 (in mammals). Structurally, the EB protein family contains a conserved N-terminal calponin homology domain (CH domain) [14,25], a variable linker region,

and a coiled-coil domain (Figure 1.3) [14]. The coiled-coil domain, important to regulate their homo and/or hetero-dimerization [25,26], further extends with a four-helix bundle and a disordered C-terminal EEY/F motif (Figure 1.3) [25,26]. EB proteins' EEY/F motif allows the interaction with numerous +TIPs including the CAP-Gly proteins [28]. The four-helix bundle and the C-terminal tail is called EB homology domain (EBH domain) (Figure 1.3), and allows the interaction with proteins containing the SxIP motif [27,28,29].

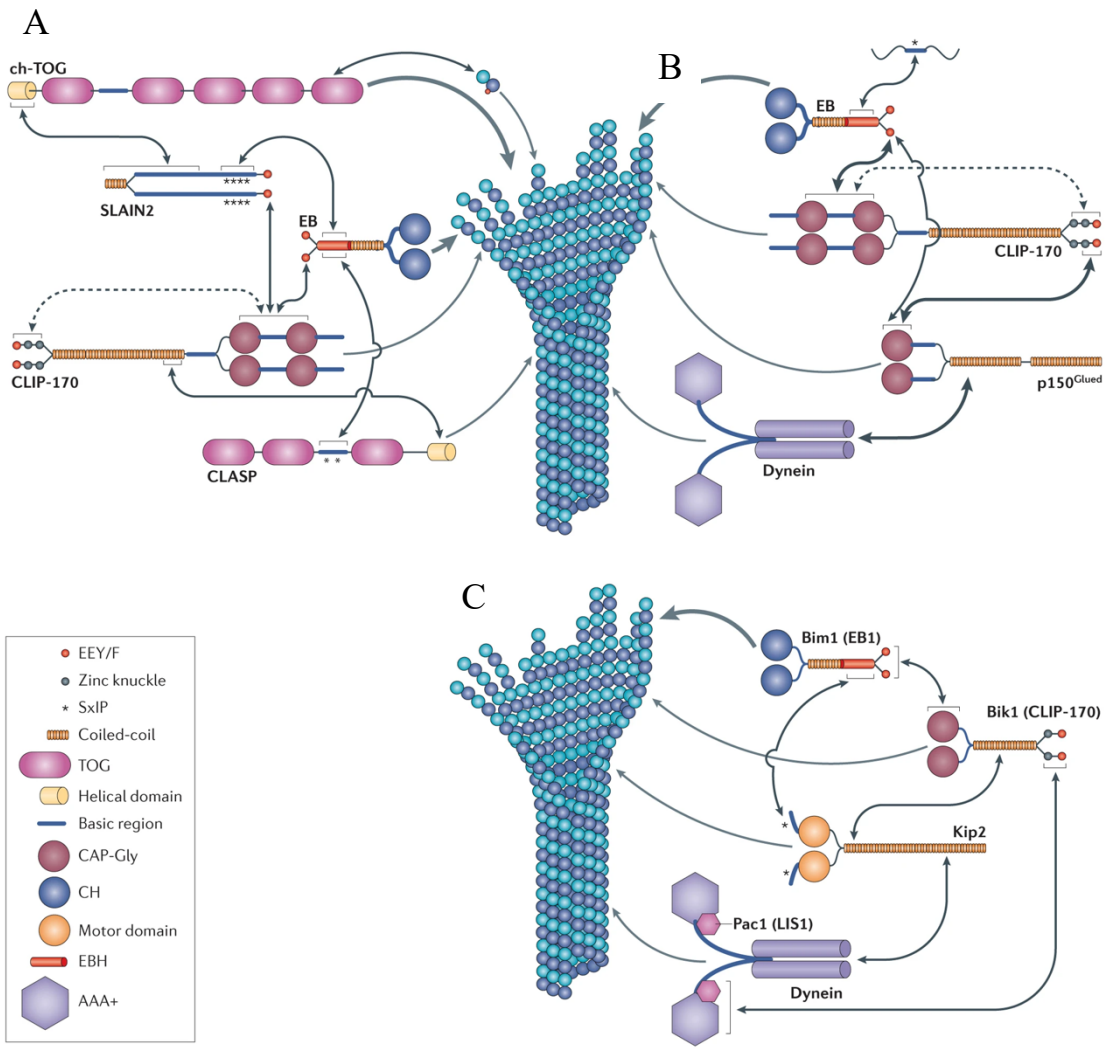

Figure 1.3| Microtubule plus-end tracking proteins (+TIPs) networks and +TIPs structural domains. A| +TIP network schematic representation containing a dynamic microtubule, ch-TOG, SLAIN2, EB, CLIP-170, and CLASP. **B|** +TIPs network schematic representation containing a dynamic microtubule, EB, CLIP-170, p150Glued, and dynein. **C|** +TIPs network schematic representation (in yeast) with a dynamic microtubule, Bim1, Bik1, Kip2, Pac1, and dynein. Most of the +TIPs share the same structural domains (represented at the bottom left list) and mode of interaction between them. The arrows indicate inter- and intra-molecular interactions between regions or domains of different and/or same proteins. Image is adopted from Akhmatova and Steinmetz, 2015.

The CAP-Gly domain (cytoskeleton-associated protein glycine-rich) is a structured domain that bind to the EEY/F motif through a conserved hydrophobic cavity rich in glycine residues (Figure 1.3) [28]. The CLIP family and the p150glued domain are the most characterized CAP-Gly domain containing proteins [14].

The large number of +TIPs also have proteins with a Ser-x-Ile-Pro (SxIP) polypeptide motif (Figure 1.3) [29]. This motif is rich of positively charged residues [25,29] and allows the interaction with the EBH domains. Examples of these proteins regard the adenomatous polyposis coil (APC) tumor suppressor and the stromal interaction molecule 1 (STIM1) [29].

Another class of +TIPs is characterized by the proteins with the tumor overexpression gene (TOG) domains (Figure 1.3). The most notable examples include XMAP215 and CLASPS family proteins [14]. Structurally arranged in tandem, TOG domains bind curved tubulin heterodimers and function as promoters of MTs polymerization [30-32].

The majority of the +TIPs can bind to MTs, other +TIPs, and/or oligomerize themselves, ultimately allowing the formation of a highly dynamic network, which is essential to regulate MTs structure and function under specific physiological states [14,25,27,32]. This network is mostly dictated by interactions of domains and motifs, including CH, coiled-coils, EBH, CAP-Gly, EEY/F, and SxIP (Figure 1.3).

2.1.5 Minus-end tracking proteins (-TIPs)

The main function of minus-end tracking proteins (-TIPs) is to determine the spatial organization of MTs (Figure 1.4) [14,25,33-41]. Among the well characterized -TIPs, there is the γ-tubulin ring complex (γ-TURC), a cone-shaped structure mainly formed by the γ-tubulin complex proteins (GCPs) bound to γ-tubulin [35]. This complex acts as a MT minus-end cap and a machinery to nucleate MTs (Figure 1.4) [33,34]. In vivo and/or in vitro, the γ-TURC complex can associate with additional proteins through direct or indirect binding [33]. A notable example is the protein augmin, known as HAUS in mammals, which interacts with γ-TURC and promote the nucleation of MTs from pre-existing MTs [36]. Another well characterized -TIP is the calmodulin-regulated spectrin-associated protein family (CAMSAP) [38,39]. For example, CAMSAP2 contains three structural domains, such as a N-terminal CH domain, a central coiled-coil domain, and a C-terminal CKK motif (Figure 1.4) [12,39]. CAMSAP proteins recognized the minus-end of MTs regulating its dynamics [37-40]. An

additional example of -TIP is KANSL3, a component of the interphase chromatin-associated protein complex (KANSL) [41].

A

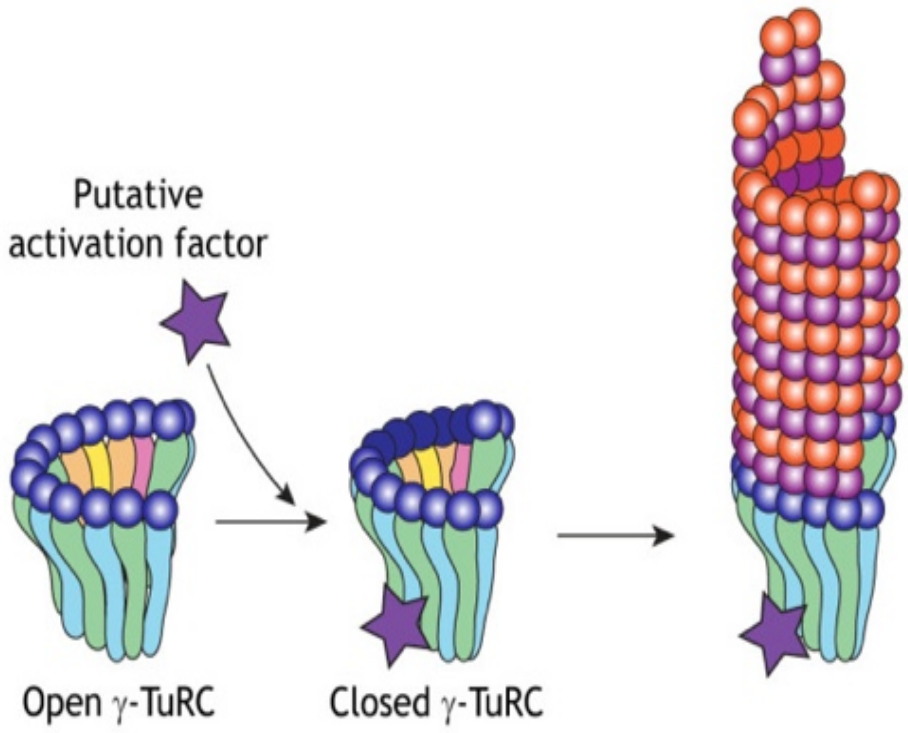

B

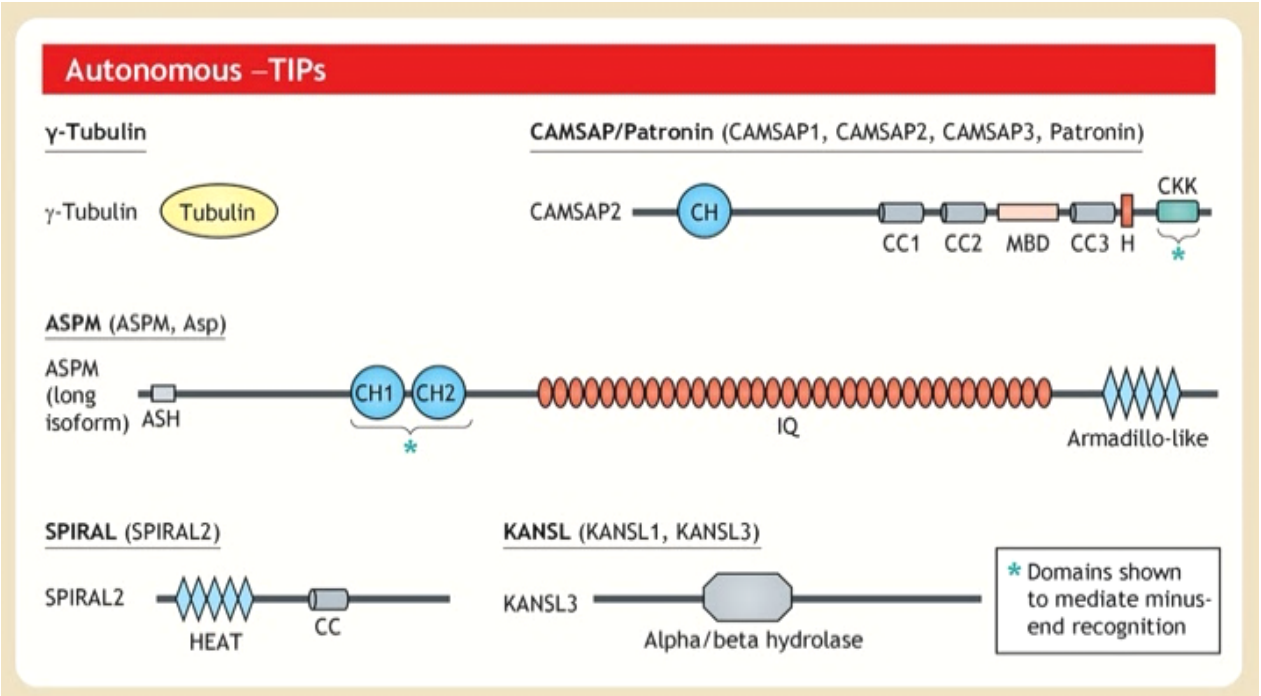

C

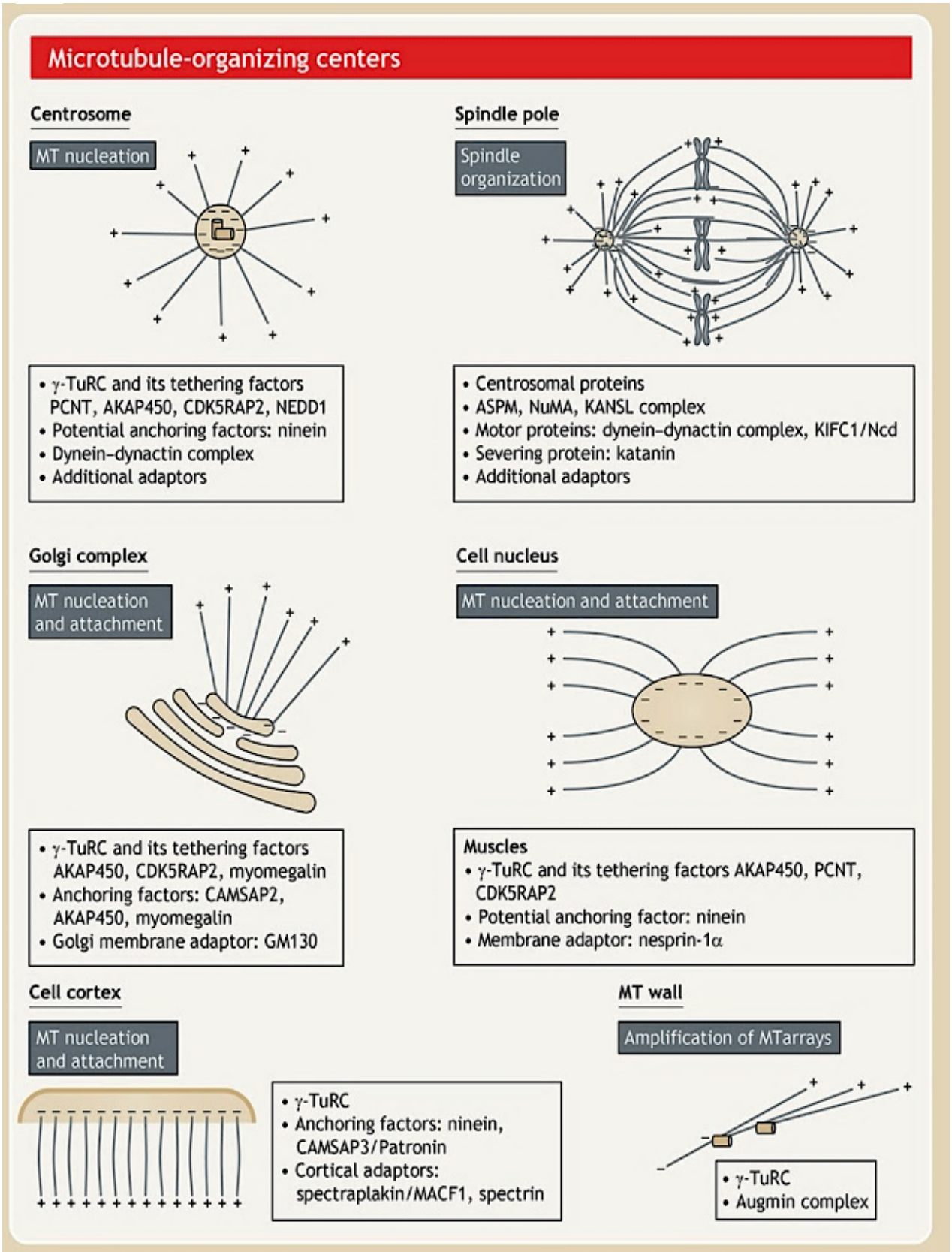

Figure 1.4| Microtubule minus-end tracking proteins (-TIPs) and example of microtubules organizing centers (MTOCs). A| Schematic model of γ-TURC activation: an activation factor binds to the pre-nucleation

conformation of γ-TURC (open conformation) and induces a change into a closed conformation. The closed γ-TURC could nucleate MTs. Image is adopted from Thawani and Petry, 2021. **B|** Schematic representation of +TIPs proteins and their structural domains, including γ-tubulin, CAMSAP2, ASPM, and SPIRAL. Image is adopted from Akhmanova and Steinmetz, 2019. **C|** Schematic representation of some microtubule organizing centers (MTOCs), including centrosome, spindle pole, Golgi complex, cell nucleus, cell cortex, and MT wall. Image is adopted from Akhmanova and Steinmetz, 2019.

2.2 Microtubule organizing centers (MTOCs)

Despite maintaining cellular architecture and morphology, MTs participate in many biological processes depending on the specific physiological context, including intracellular trafficking, cellular motility through cilia and flagella, as well as spindle formation during cell division. This complexity can be achieved as MTs are a highly dynamic, self-organized and regulated machineries. The cellular structures where MTs can be nucleated are called microtubule organizing centers (MTOCs), and include centrosomes in animal cells, non-centrosomal assemblies, as well as spindle pole bodies in fungi [20]. In metazoans, the major component of most MTOCs is the nucleating machinery γ-TURC [42,43] (Figure 1.4). These nucleating machineries are further enriched by many other proteins that recruit or are recruited at different MTOCs depending on the organisms, cell state and/or types [20,42,43].

2.2.1 Centrosome

A relevant MTOC in dividing cells is the centrosome, which is formed of two centrioles and the pericentriolar material (PCM). The membrane-less centrosome is involved in cell division as being responsible for MTs nucleation, as well as for stabilization and anchorage of MTs minus-ends (Figure 1.4) [42,43,44].

Centrioles are structures characterized by a 9-fold symmetric array of MTs as well as other structural proteins [44,45,46]. This MTs arrangement can contain singlets, doublets, or triplets. While most eukaryotic organisms have triplets, exceptions are found in *Drosophila* embryos with 9 doublets, as well as in nematodes with 9 singlets. Centrioles are formed as perpendicularly oriented pairs (the old one and the new one, named mother and daughter) and are surrounded by the PCM [44,45,46]. The PCM is composed of layers of fibers and/or matrix proteins. Centriole replication and PCM assembly are synchronized to the mitotic cycle and any miscoordination between these processes can result in chromosomal missegregation and cancer [47]. Centrioles are also essential structures of cilia and flagella [48]. Alterations in cilia can contribute to ciliopathies [49,50].

The molecular composition of centrioles was recently determined through pioneering work in *C. elegans* [52-59]. There are five core centriolar proteins, including ZYG-1 [51], SPD-2 [52,53], SAS-4 [54,55], SAS-5 [56] and SAS-6 [57]. All these proteins are conserved in the majority of ciliated cells (Figure 1.5) [45,49].

In *C. elegans*, centriole duplication is started when the divergent Polo-like kinase 4 (Plk4) called ZYG-1 is recruited by SPD-2 (Figure 1.6), a protein that localize at both centriole and PCM [52,53]. The electrostatic interaction between SPD-2 N-terminus (short acidic stretch) and the CBP domain of ZYG-1 is a conserved mode of interaction (Figure 1.6) [60], including *H. sapiens* [61,62] and *D. Melanogaster* [60].

Homo sapiens	**Function**	***Drosophila melanogaster***	***Caenorhabditis elegans***
PLK4	Centriole duplication	Plk4 (Sak)	ZYG-1
SAS6	Centriole duplication	Sas6	SAS-6
STIL	Centriole duplication	Ana2	SAS-5
CPAP	Centriole assembly	Sas4	SAS-4
CEP135	Centriole assembly	Cep135	–
CEP152	PLK4 recruitment	Asl	–
CEP192	PLK4 recruitment, PCM assembly	Spd2	SPD-2
CDK5RAP2	PCM assembly	Cnn	SPD-5
CEP295	PCM assembly	Ana1	–

Figure 1.5| Nomenclature of the main centriolar proteins and their conservation across species. Image is adopted from Nigg and Holland, 2018.

The SPD-2 human homolog, known as Cep192, cooperates with the protein Cep152 to allow the recruitment of Plk4 [61-64] (Figure 1.5). *C. elegans* lacks a Cep152 ortholog (Figure 1.5) [47,59]. In *Drosophila*, the only centriole receptor for Plk4 is the Cep152 ortholog called Asterless [47,60] (Figure 1.5). While *in silico* analysis indicates that SPD-2/Cep192 orthologues are composed of an unstructured N-terminus, a short coiled-coil domain, and a long beta-strand-rich C-terminus [45], Asterless/Cep152 orthologues are predicted as coiled-coils [45].

In *C. elegans*, the Plk4 kinase called ZYG-1 localizes at centrioles peaking in anaphase [51,57]. While ZYG-1 and Plk4 show divergence in their protein sequence, they share a similar structure consisting of the N-terminal kinase domain, the central cryptic polo box (CPB) domain, and the C-terminal single polo-box (PB3) domain [45].

Once ZYG-1 is at the site of centriole assembly (Figure 1.6), it recruits the proteins SAS-5 and SAS-6 (Figure 1.7) [59]. The SAS-5 fly and human orthologs are known as Ana2 [65, 66] and STIL [67], respectively (Figure 1.5). SAS-5 and SAS-6 build a cytoplasmatic structure [58] that

is incorporated at centrioles undergoing assembly through direct interactions of ZYG-1 and the coiled-coil region of SAS-6 [68] (Figure 1.7). The ZYG-1's phosphorylation activity is required to stably incorporate the SAS-5/SAS-6 complex [59,68]. The human and flies Plk4, similarly to worm ZYG-1, recruits SAS-5 orthologues STIL/Ana2 and SAS-6, though molecular details of the incorporation may differ [69-74].

When the SAS-5/6 complex is present at the nascent centriole site, it forms the central tube which is a structure with a characteristic 9-fold symmetry (Figure 1.7). This structure, also known as cartwheel, becomes stabilized with the incorporation of singlets MTs through a process dependent on the coiled-coil protein SAS-4, that ultimately forms the outer tube [75-78].

A

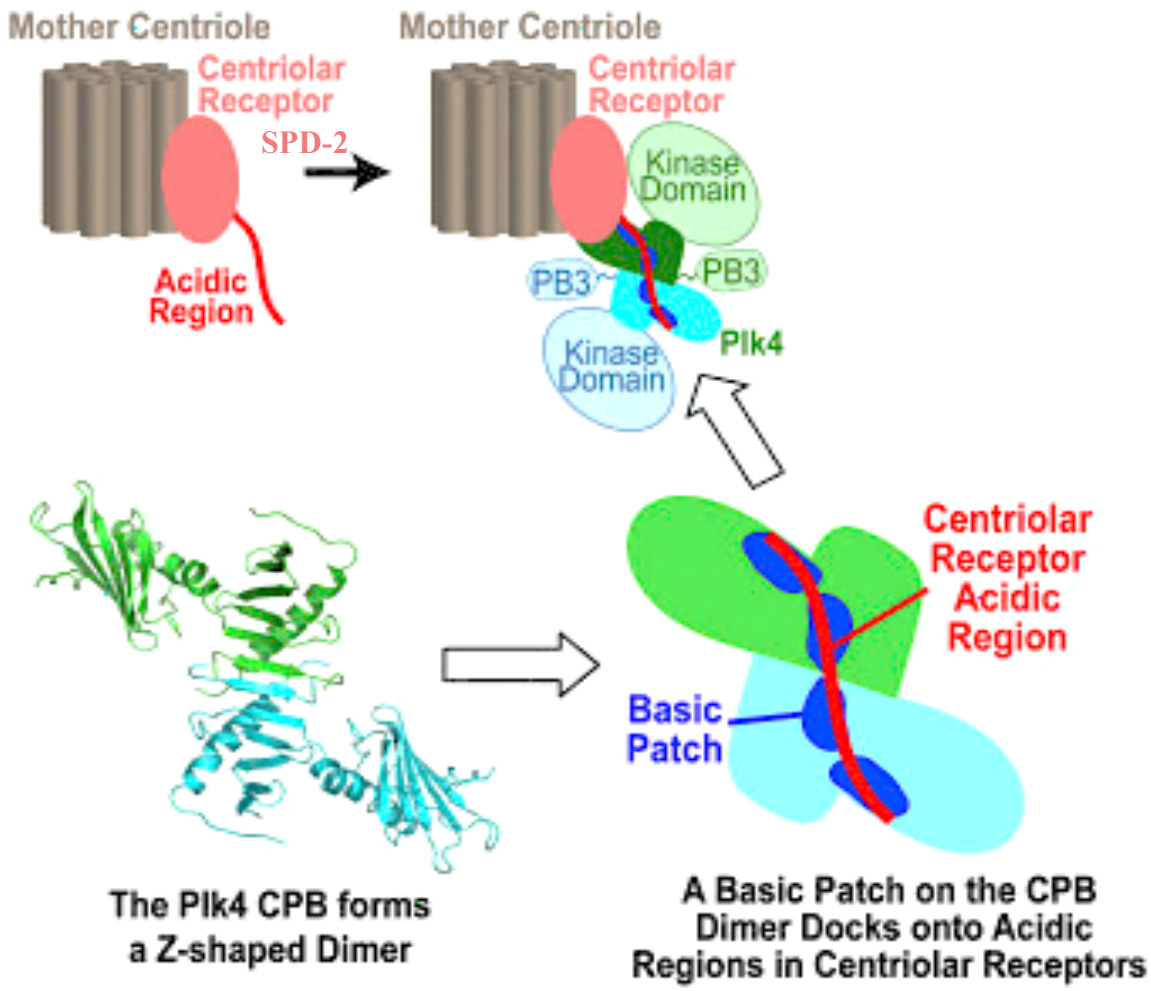

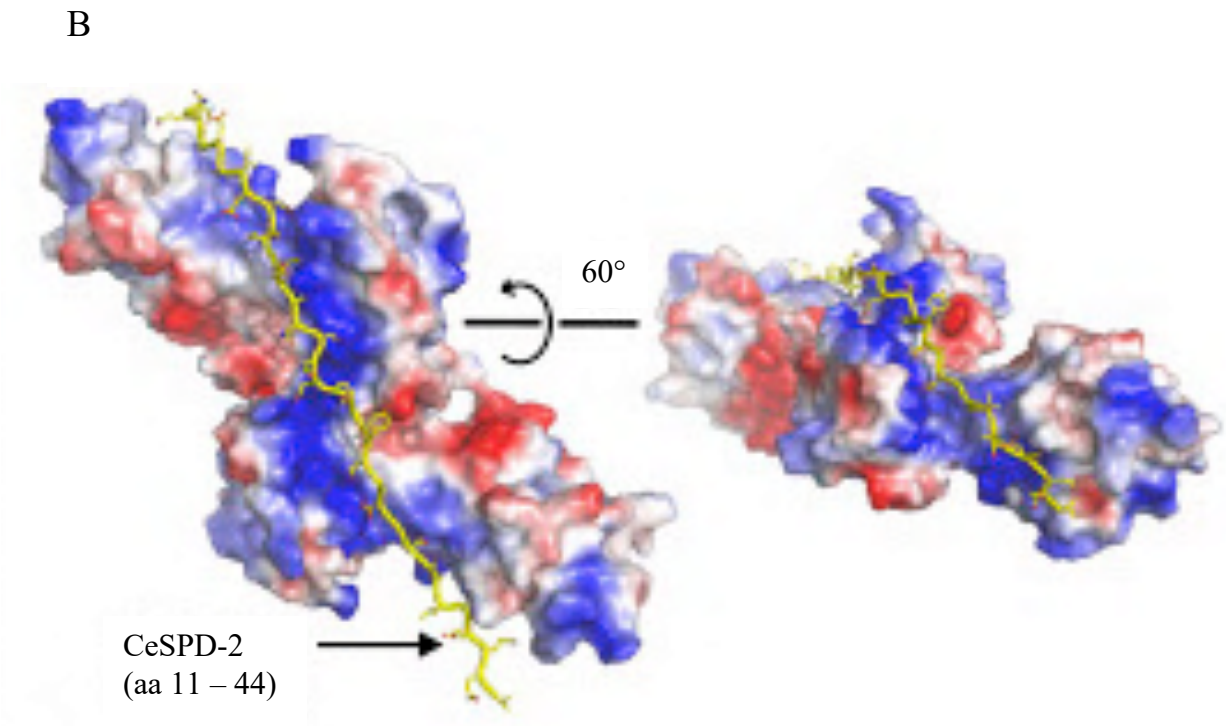

Figure 1.6| Beginning of centriole duplication (centriole assembly). A| The mother centriole (that is represented in brown) is bound to SPD-2 (that is represented in pink). SPD-2 has an acidic stretch that function as a recruitment tail for the dimeric CPB domain of Plk4. **B**| Docking analysis with the structures of ZYG-1 CPB dimer (that is represented with an electrostatic surface) and SPD-2 N-terminus (aa 11- 44). Image is adopted from Shimanovskaya et al, 2014.

Although SAS-4, found in worms, appears distantly related to the humans and flies counterparts, CPAP and SAS-4 [77-79], these proteins share most of their structural arrangements. Specifically, they contain a disordered N-terminus, a coiled-coil domain, as well as a TCP domain at the C-terminus. In addition to controlling the centriole size, SAS-4 is also involved in PCM accumulation [77,80-87].

Collectively, these intricate mechanisms explain how mother centrioles form daughter centrioles (centriole assembly). However, daughter centrioles are required to form new sets of centrioles for the next round of cell division or different physiological processes, and therefore needs to become replication competent (daughter-mother conversion). In vertebrates and worms, centriole assembly and daughter-mother conversion are two different processes [88]. In C. elegans, the ability to convert daughter centrioles into new mother centrioles (or daughter replication competency) is dictated by SAS-7, a protein with the ability of recruiting SPD-2 [89] (Figure 1.8). The coiled-coil SAS-7 lacks homology to proteins outside nematodes.

Nonetheless, CEP152 in humans and Asl in *Drosophila* have a similar localization pattern [62,90] and play a crucial role in daughter-mother conversion in their respective organism.

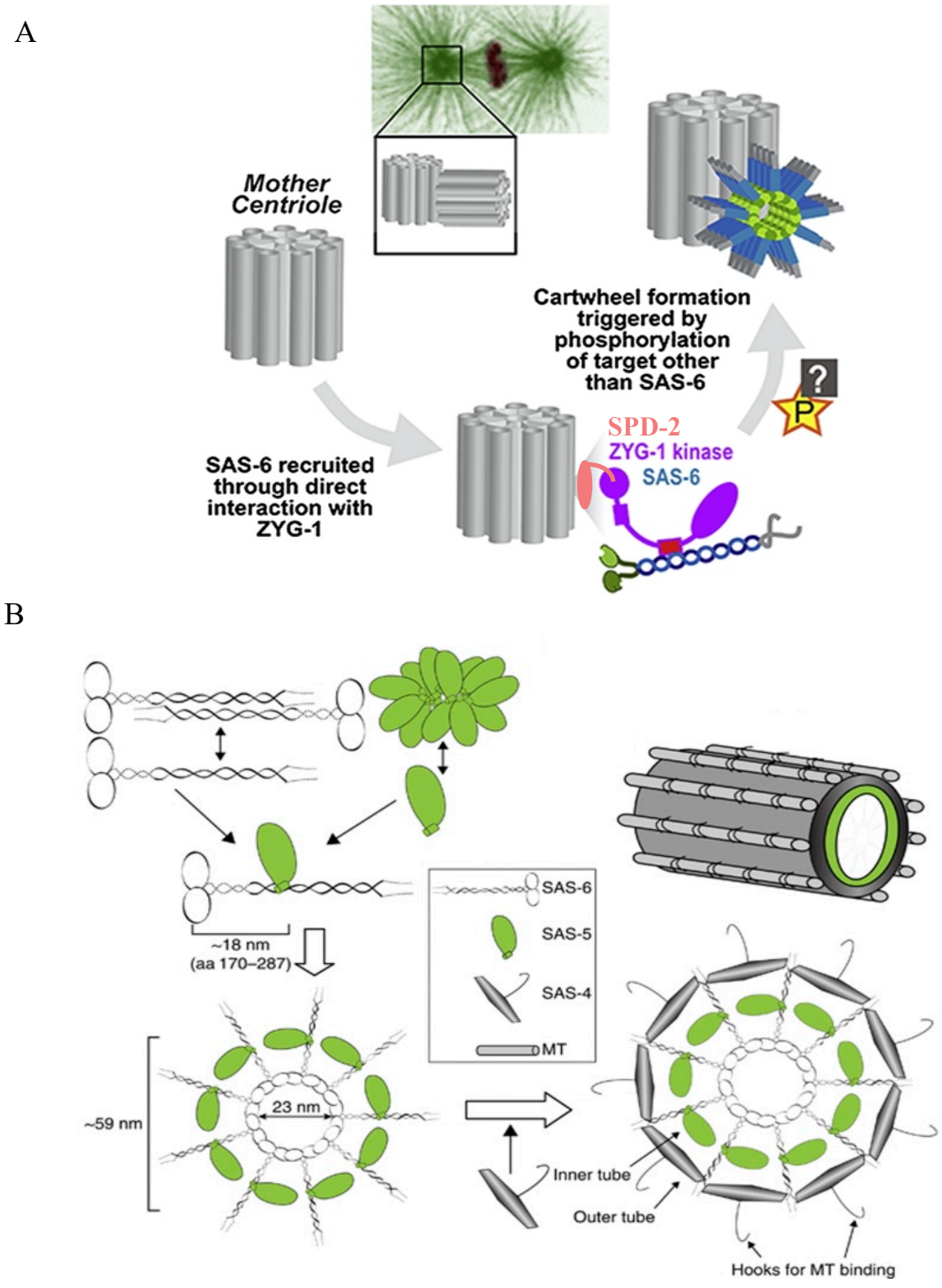

Figure 1.7| Cartwheel formation during centriole duplication (centriole assembly) *in C. elegans*. A| Schematic model of cartwheel formation where ZYG-1 (represented in violet), bound at the mother centriole

(represented as 9-fold symmetric array of MTs in grey) to SPD-2 (in pink), recruits SAS-6 coiled-coils (that is represented in blue). Image is adopted from Lettman et al, 2013. **B|** Schematic molecular mechanism of cartwheel comprising the proteins SAS-5, SAS-6, and SAS-4. Image is adopted from Qiao et al, 2012.

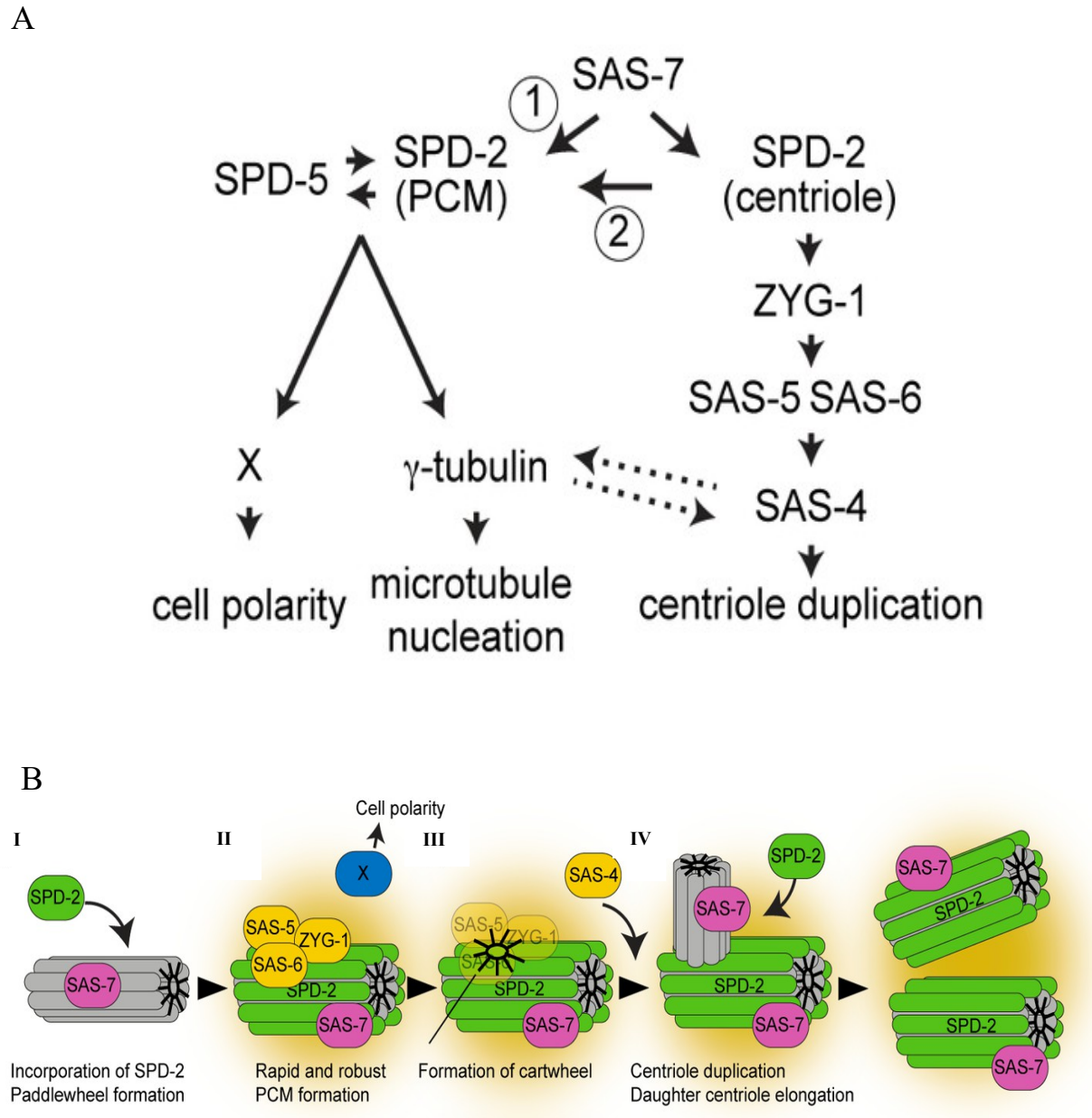

Figure 1.8| Centriole assembly, daughter-mother conversion and PCM in *C. elegans*. A| Scheme of the processes of centriole assembly, daughter-mother conversion, and PCM formation. In this model, SAS-7 recruitment of SPD-2 is shown to be regulating centriole duplication, daughter-mother conversion, as well as PCM formation. SAS-7 might signal for PCM assembly directly or indirectly (arrow 1 and 2, respectively) via SPD-2. The PCM formation also requires proteins such as SPD-5, γ-tubulin, and polarity factors (represented with the letter X). Some PCM component(s) may regulate SAS-4's recruitment (dotted arrows) during centriole duplication or assembly. In addition to SAS-7, the centriole assembly process requires proteins such as ZYG-1, SAS-5, SAS-6, and SAS-4. **B|** (I) Centriole assembly is initiated when SAS-7 recruits SPD-2 at the mother centriole. (II) SPD-2 further recruits ZYG-1 that allow the incorporation of SAS-5 and SAS-6. The complex comprised of SAS-5 and SAS-6 forms the central tube. (III) The complex comprised of SAS-5 and SAS-6 promotes the recruitment of SAS-4, that form the outer tube. (IV) Singlet MTs symmetric array is formed. Image is adopted from Sugioka K. et al, 2017.

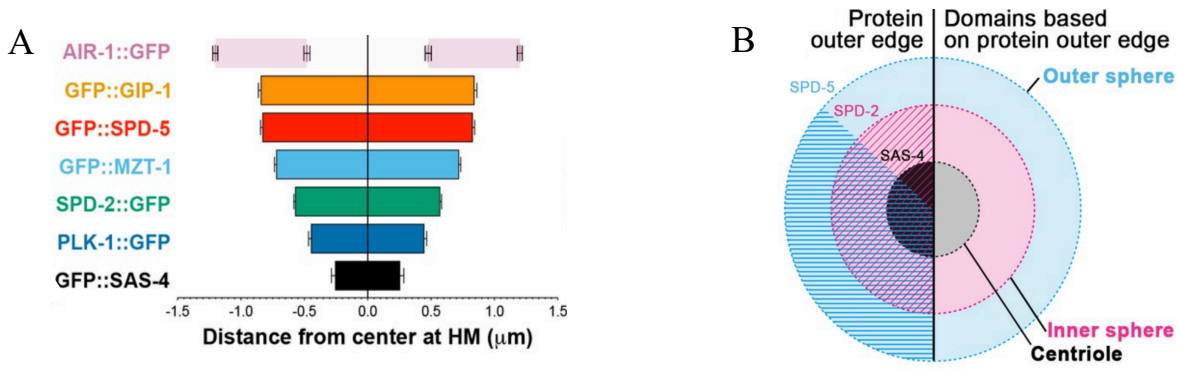

Figure 1.9| Organization of the PCM in *C. elegans*. A, B| Scheme of the organization and distance of centriolar and PCM proteins in *C. elegans*. Image is adopted from Magescas, J. et al 2019.

During centriole assembly, SAS-7, SPD-2, and SAS-4 contribute to PCM formation and/or accumulation. In particular, the PCM is built with layers containing hundreds of proteins that are dynamically organized throughout the cell cycle [43,46]. In *C. elegans*, the composition of these layers is simpler than the one found in humans or flies [43,46]. Previous studies showed that the outer edge localization of some proteins allows the characterization of the PCM into two layers, respectively called the inner and outer sphere (Figure 1.9) [46]. The inner sphere delimited by SPD-2 and can contain proteins such as PLK-1, TAC-1, ZYG-9, γ-TURC, TPXL-1, and AIR-1 [46]. In contrary, the outer sphere is delimited by SPD-5 and it contains proteins such as GIP-1, ZYG-9, MZT-1, TAC-1, AIR-1, and TPXL-1[46]. In addition to some of the centriole assembly proteins, the assembly and disassembly of the PCM is also tightly regulated by kinases and phosphatase activities [46]. Although few of these proteins contain homologues through evolutionary distant organisms, such as humans and flies, the complexity of the PCM and its organization include additional factors that varies depending on cell cycle and cell type.

2.2.2 Cilia, flagella, and basal bodies

Cilia and flagella are evolutionarily conserved structures characterized by a complex arrangement of MTs and MTBPs that are anchored to platforms known as basal bodies [20,48,91,92]. These structures play essential roles in motility as well as cellular signaling across a variety of organisms and/or species [91]. Despite the conservation across evolution, numerous studies have described diversity in architecture, functionality and biogenesis [48,91,92]. For example, motile cilia are usually formed through a structure known as the axoneme, where MTs could arrange into the "9 + 2" architecture (9 outer doublets and a central pair) and hosts a diverse set of regulatory proteins, including motors (Figure 1.10). In contrary, the majority

basal bodies are formed of a symmetric 9-fold array of triplets MTs as well as regulatory MTBPs.

2.3 Additional MTOCs and/or microtubule-based structures

2.3.1 Mitotic spindle

The mitotic spindle is a self-assembling and highly regulated structure that forms in the cytoplasm from the prophase of the mitotic cycle [93]. Crucial for the segregation of chromosomes, it contains dynamic MTs and a variety of regulatory proteins such as MTBPs and MAPs. In animal cells with centrosomes, a fully formed spindle occurs at metaphase and it is characterized by three classes of MTs (aster, kinetochore, and overlapping microtubules) that coordinate and provide a mechanical influence over the segregation process (Fig. 1.10). In other cell types lacking centrosomes, the mitotic spindle can assemble from alternative nucleation pathways, including chromatin-mediated nucleation and augmin-mediated MT generation [93-95].

2.3.2 Midbody

The midbody is a complex structure that appears at cytokinesis, the final stages of mitosis, that facilitates the physical separation of the two daughter cells (abscission) through the formation of the cleavage furrow [96]. It is located at the so called “intracellular bridge” and consists of bundled MTs and MTBPs, including MAPs. During this process, the spindle MTs are compacted and supplemented with regulatory proteins that ultimately allow the abscission [96]. Emerging research also identified that the midbody might influence cell polarity and fate decisions through its involvement in the Wnt (Wingless and Int-1) and Notch signaling pathways [20,96] (Figure 1.10).

2.4 Sjögren’s syndrome nuclear autoantigen 1 (SSNA1)

SSNA1, also named as NA14 or DIP13, is a MTBP previously characterized as MT remodeling factor [97]. Like many MTBPs, it is predicted to arrange as coiled-coil protein. SSNA-1 has been first described as an autoantigen found in the serum of a Sjögren’s Syndrome’ patient [98,99]. Since this finding, SSNA-1 is used as a major target for autoantibodies in primary Sjögren’s Syndrome (PSS) [99]. The PSS is an autoimmune rheumatic disease where exocrine

glands are infiltrated by lymphocytes, ultimately causing altered lacrimal and salivary secretions [100].

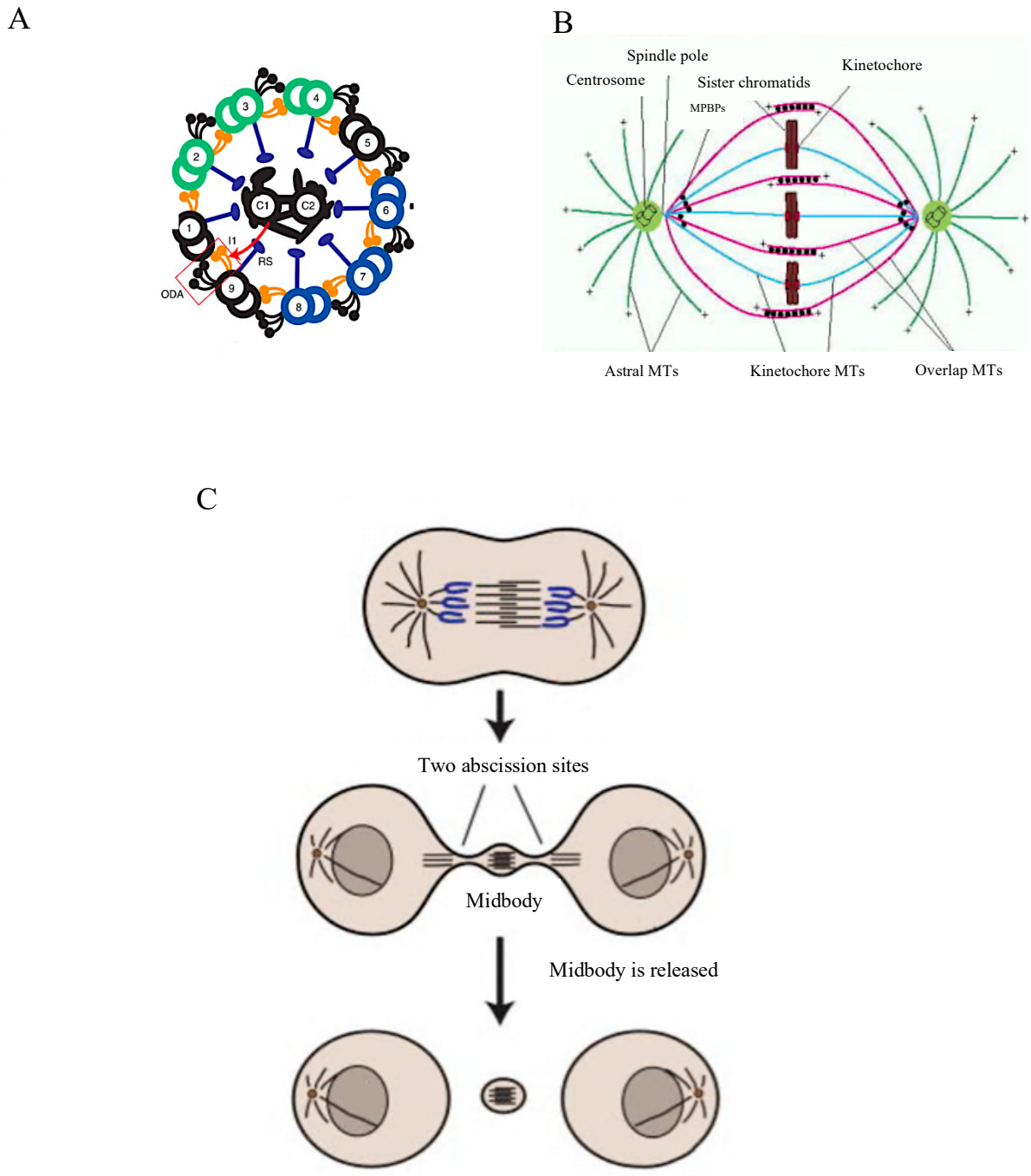

Figure 1.10| Cilia, mitotic spindle and midbody. **A**| Orthogonal view of the axoneme with the characteristic "9 + 2" architecture of MTs. While the outer doublet MTs are represented as C1-C9, the central pair of MTs is represented as C1 and C2. The regulatory proteins, such as the outer dynein arms and radial spokes, are represented as ODA and RS. Image is adopted from Viswanadha, R., et al, 2017. **B**| Schematic representation of the three classes of MTs of the mitotic spindle formed during metaphase of an animal cells. Image is adopted from Alberts, B., Johnson, A., Lewis, J., et al, 2002. **C**| Schematic representation of the midbody allowing physical separation of the two daughter cells (abscission) through cleavages of bundled MTs. Image is adopted from Dionne, L. K., et al, 2015.

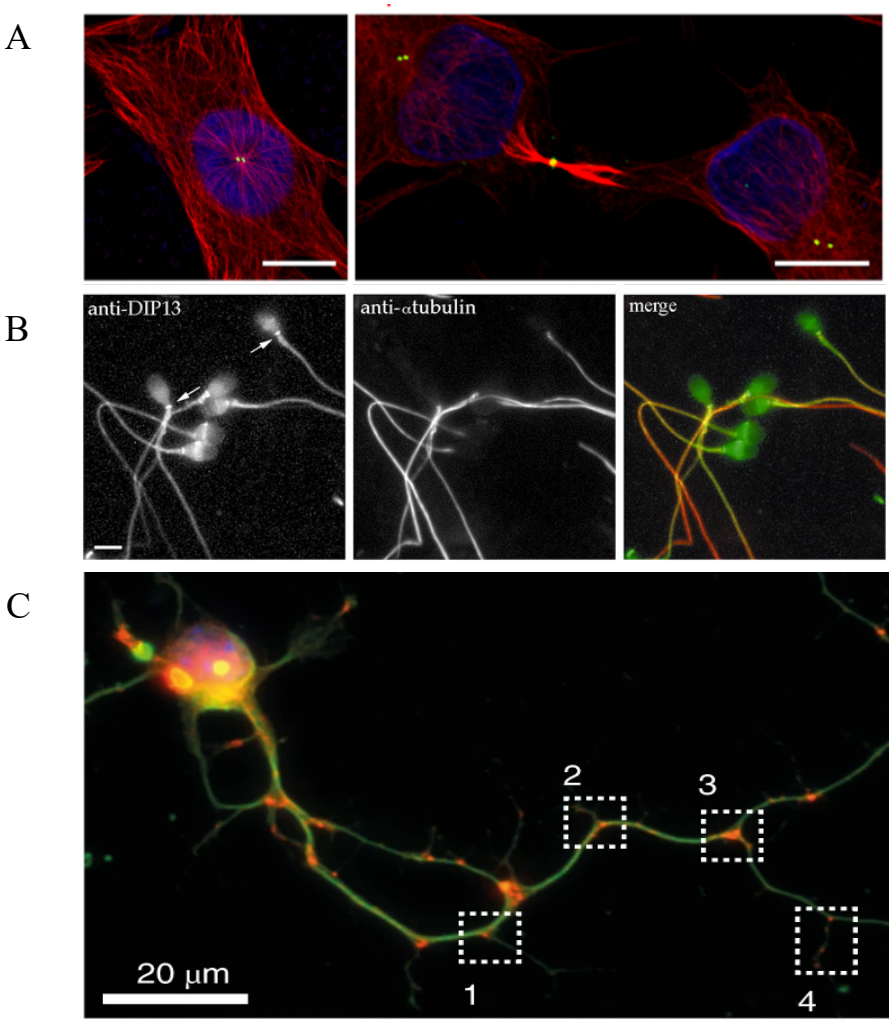

Figure 1.11| SSNA1 localization. **A**| Images of endogenous SSNA1/NA14 (in green) at the centrosome during interphase (left image) and at the midbody during late cytokinesis (right image) in HeLa cell lines. Tubulin is also represented (in red). The yellow color represents the co-localization of SSNA1/NA14 and tubulin (merge). The scale bar is 10 µm. Image is adopted from Goyal et al., 2014. **B**| DIP13/NA14 localizes to flagella in human spermatozoa. SSNA1 is represented in green and tubulin in red (immunostaining). The scale bar is 10 µm. Image is adopted from Pfannenschmid et al., 2003. **C**| SSNA1 is represent in red and tubulin in green. The immunostaining image contains neurons overexpressing SSNA1. The boxes 1-4 show SSNA-1 localization at axon branching points. The scale bar is 20 µm. Image is adopted from Basnet et al., 2018.

Homologues of SSNA1 are found in many eukaryotes such as fish, insects, protozoan parasites and green algae [101]. Interestingly, this ~14 kDa protein localizes in MTOCs, including centrosomes, basal bodies of cilia and flagella, the midbody of dividing cells, as well as axon branching points [97,98,101-105] (Figure 1.11).

When the expression of SSNA1 was reduced in green algae, through RNAi, multinucleate and multiflagellate cells were observed [102], showing defects in cell division. Similar to *C.*

reinhardtii, the reduction of SSNA1 expression in mammalian cells resulted in multinucleated cells, as well as the reduction in percentage of mitotic cells [105], showing again defects in cell division. While it was observed that SSNA1 could interact with the MT severing protein spastin, explaining its involvement during cytokinesis, no particular investigations explained SSNA1 role at the centrosome, perhaps key to understand better the cell division defects previously reported.

Furthermore, it's been showed that SSNA1 overexpression in fibroblast altered MT networks [97]. In neurons, SSNA-1 was instead characterized as promoter of axon development as well as axon branching [97,105].

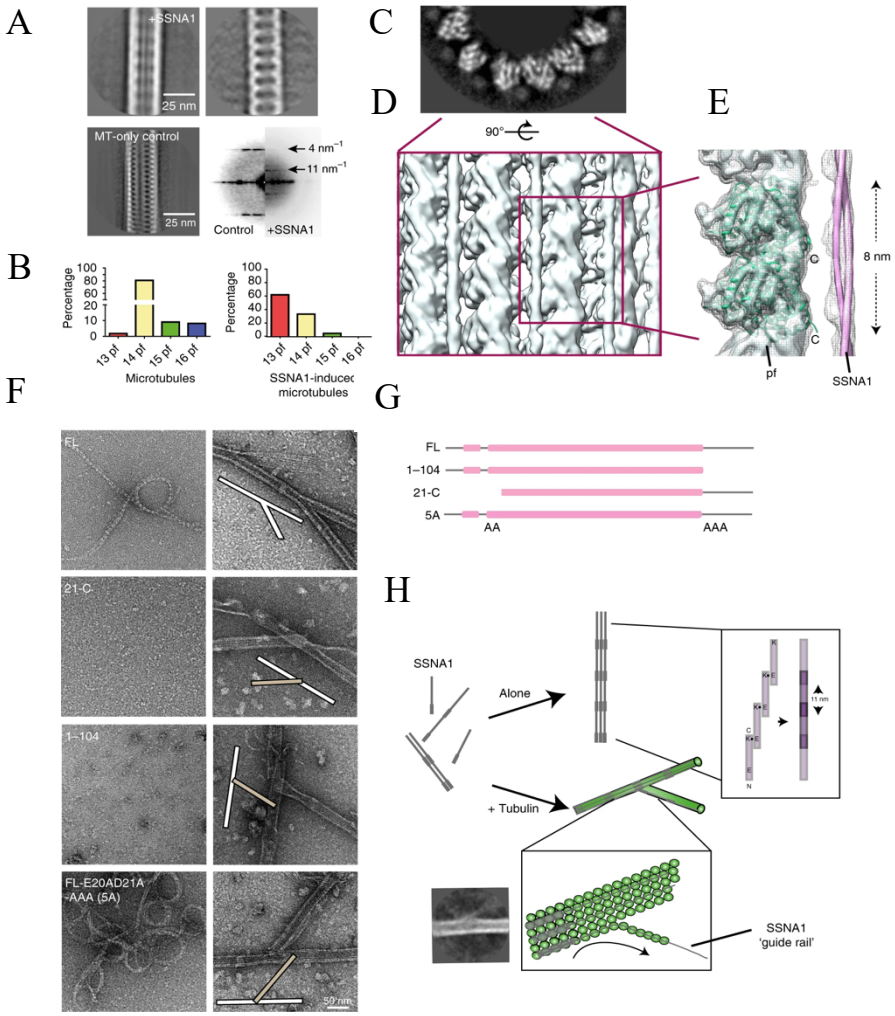

Figure 1.12| Characterization of SSNA1 (DIP13) and SSNA1 bound to MTs. **A**| Top left: 2D class average of MTs decorated with SSNA1. Top right: SSNA-1 decoration emphasized by computationally subtracting microtubule densities. Bottom left: 2D class average of MTs in absence of decoration. Bottom right: the power spectrum of MTs decorated with SSNA-1 class averages, showing 4 nm periodicity of tubulin and 11 nm periodicity of SSNA1. **B**| Protofilament (pf) number distribution of MT reconstituted in the absence (left) and in the presence (right) of SSNA1. **C**| Greyscale slice from the density map of the plus-end view of the SSNA1–microtubule 3D

reconstruction. **D|** Cryo-EM map of microtubule decorated with SSNA1. **E|** Tubulin atomic model (PDB ID: 3jal) fitted to the cryo-EM map (in green). The coiled-coil fibril of SSNA1 is represented with a tube (in purple). **F|** Negative staining of different SSNA1 constructs (left images) and their effect on microtubules (right images). **G|** A schematic model of the SSNA1 constructs used in F. **H|** A schematic model of the observed molecular behaviors. Image is adopted from Basnet et al, 2018.

Taking these observations altogether, it is clear that SSNA1 is involved in regulating the MTs dynamics. For example, *in vitro* studies described in detail the *C. reinhardtii* homologues of SSNA1, called DIP13, as a factor for MT nucleation and remodeling activity (Figure 1.12). Specifically, DIP13 mixed with unpolymerized tubulin formed tubulin clusters where MTs radiated out, resembling astral MTs. During this process, DIP13 could also remodel MTs into branched structures (Figure 1.12) [97]. The branching activity of DIP13 was showed to be relying on its self-assemble. Such self-assembly ability, observed as filaments of 11 nm periodicity, occurred through a head-to-tail mechanism with key interactions occurring between the negatively charged residues at N-terminus (E20 and D21) and positively charged residues (K105-107) at the C-terminus (Figure 1.12) [97]. A 6.1 Å cryo-EM structure of MT decorated with DIP13 has also revealed that DIP13 filaments can be found between protofilaments of MTs, near tubulin's C-terminus which contain the E-hooks (Figure 1.12) [97]. The periodical organization of tubulin in MTs allows the E-hooks to make a negative electrostatic cloud [106], which could recruit SSNA1 fibrils through the shielding of the electrostatic C-terminal tail. According to this hypothesis, it's been proposed that SSNA-1 could act as "guide rail" guiding the protofilaments of MTs (Figure 1.12) [97].

These experiments, collectively, show that SSNA1 is an important MTBP which can modulate microtubule dynamics and remodel MTs architecture. A recent article also found that SSNA1 could act as MT's stabilizer and sensor of damage *in vitro* [107].

2.5 Transmission electron microscopy in structural biology

TEM (transmission electron microscopy) is a method using an electron beam which is focused to a thin sample specimen, typically about 100 nm in thickness, to form an image known as electron micrograph. The initial endeavors to analyze the size and the shape of biologicals by TEM started from the 1940s [108]. Over the years, the field has grown with a multitude of applications and continuous technological advancements for the exploration of biomolecules [109].

2.5.1 Negative staining EM, and cryo-EM for single particle analysis

Combined with X-ray crystallography and nuclear magnetic resonance (NMR), electron microscopy (EM) can be considered another powerful technique to characterize the 3D structure of biological molecules. When biological molecules are observed through EM, the contrast generated in the micrographs is usually low [110, 111]. To overcome this issue, scientists embed biological molecules in a dried amorphous heavy metal solution, including molybdenum, uranium or tungsten solutions. In this manner, the electrons passing through the sample create a differential electron scattering. Such differential electron scattering, given by the mass/thickness disparity of the biological sample and the heavy metal solution, would generate high-contrast images. This approach is known as negative staining and is commonly used as screening methodology. The reason negative staining is a used as screening methodology is due to sample preparation issues. Biological specimens could indeed collapse when embedded with dehydrating solutions. Moreover, the grain size of the heavy metal limit the resolution to about 20 Å [100,111].

From the 1980s, the EM field started to overcome some of issues issue related to the sample preparation process. Such collaborative effort led to the development of methods involving the vitrification of biological samples within their natural environment. In this innovative approach, the specimens undergo plunge-freezing into liquid ethane or propane [112]. When vitrified samples are observed through EM, techniques known as cryo-EM, the images would still have low contrast due to the similar scattering of the specimens and their surroundings. To solve this issue, the 2D projections of the molecules represented in the electron micrographs can be computationally averaged to enhance the contrast or signal-to-noise ratio. In this process, it's paramount that images contain enough views, or different orientation, of the particle of interest, so different averaged 2D projections can be used to reconstruct a detailed 3D map. Few notable efforts that allowed the development of software to statistically process such images are the principal component analysis, hierarchical clustering, K-Means Clustering and Maximum Likelihood Method, as well as IHRSR algorithm [113,114]. Although such computations can be also used for negative staining images, cryo-EM, among other advantages, offers less stringent limitation in terms of resolution achievable as it's not depended on the grain size of the heavy metals. In addition, it's worth considering another key issue of biological EM which is the dose limitations. Such issue manifests when high-energy electrons pass through the specimen during a specific timeframe. Depending on the quantity of electrons

(electron dose) and/or the time of exposure used during imaging, specimens undergo electron damage caused by electrons breaking covalent bonds over time. This phenomenon could compromise the quality of the images acquired. However, the radiation damage could be ultimately contained by setting the right dose, including the time of exposure, on the microscope as well as using specific algorithms during data processing that allow to discard heavily exposed images.

Although the first strategies to process EM data were designed from the 1960s [115], continuous improvements have made this technique more efficient and powerful. Notable advancements have been made in TEM technology, electron detectors, image processing algorithms, including AI/ML-based tools, and computational power. Altogether, those advancements have allowed the so called resolution revolution in biological EM and consolidated this technique in the structural biology field [116].

A typical workflow in cryo-EM for single particle analysis is comprised of many processes (Figure 1.13). Once the specimen is vitrified onto an EM grid and a data collection through TEM has been acquired, the following steps are generally required. First, the movies, that are formed by a specific number of frames where each frame has a different dose exposure, undergo motion correction and dose weighting. While motion correction solves the motion of the particles, due to electron-molecules interaction throughout the time of exposure as well as mechanical vibrations, the dose weighting discard the frames with the most radiation damage. Afterwards, the corrected movies are used to calculate the contrast transfer function (CTF) and are sorted depending on the overall quality of the dataset. The CTF varies depending on the nature of the dataset, including a specific defocus range. Once the best micrographs are selected, jobs such as particle picking, particle extraction and 2D classification are used to calculate the 2D averaged projections. Finally, the particles selected from the best 2D classes can be used to solve the 3D heterogeneity, a job generally known as 3D classification, and refine the final map, through 3D refinement [117]. Most of these operations are performed in multiple rounds and iteratively.

To date, the number of cryo-EM structures entries is dramatically increasing. As of 01/03/2024, the cumulative entries at the Electron Microscopy Data Bank (www.ebi.ac.uk/embd) were 32033. While most structures have been solved at a resolution range of 3 - 4 Å, there are occasions where cryo-EM structures reached the range of 1 - 3 Å. Recently, a 1.15 Å-resolution apoferritin structure has been solved, setting a world record to date in term of resolution

achieved with proteins through cryo-EM [118]. Such achievements bring into consideration the exciting opportunity to use cryo-EM for structure-based drug design.

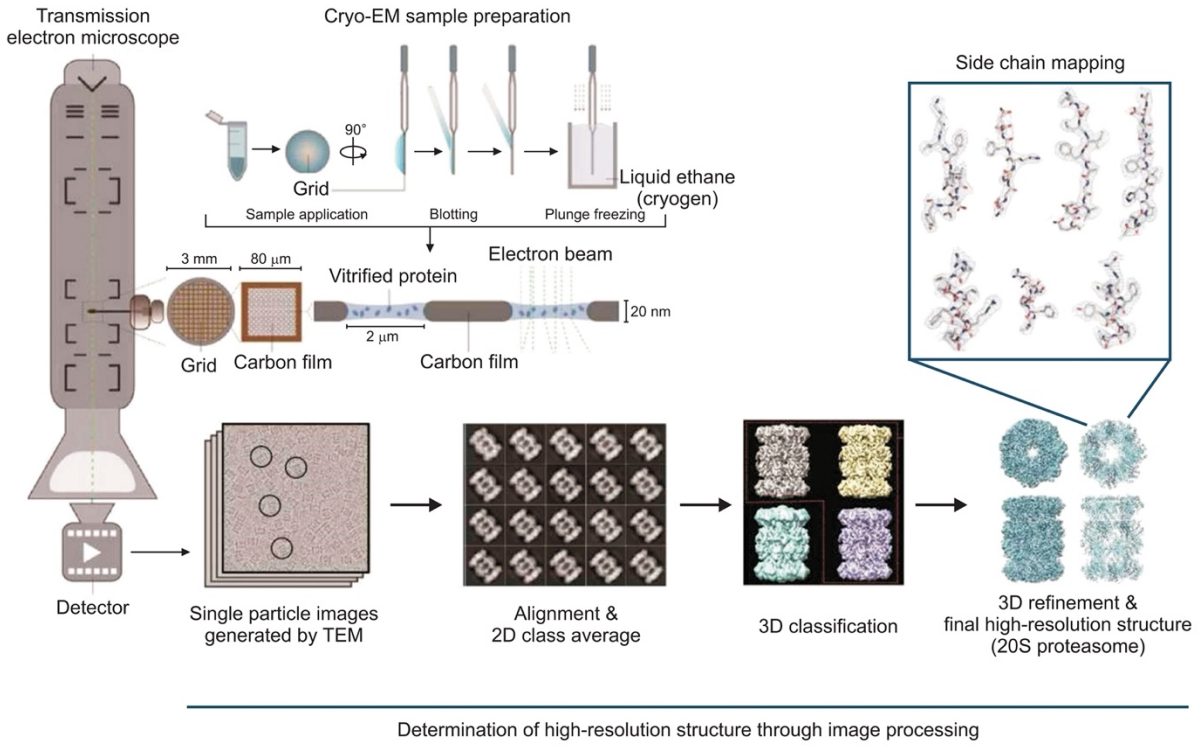

Figure 1.13| Single particle cryo-EM generic workflow. A biological specimen is applied to an EM grid and vitrified. After TEM data collection of the vitrified grid, the electron micrographs should contain 2D projections of the particles with different orientations. The 2D projections of the particles of interest are successively aligned for 2D class averaging. Finally, the best 2D classes are selected to reconstruct the 3D cryo-EM map through rounds of 3D classification and 3D refinement. Image is adopted from Chun and Kim, 2018.

3 Aim of the thesis

SSNA1 is a microtubule binding protein (MTBP) that has been characterized as microtubule remodeling factor. Some studies localize SSNA1 in microtubule organizing centers (MTOCs) such as centrosomes, basal bodies, flagella, midbody of dividing cells and neuronal axons. Despite its implication in multiple microtubule-based processes, the precise molecular mechanism underlying SSNA1's polymer formation and its regulation of centrosomes remains unclear.

The objective of my PhD thesis is to elucidate the molecular mechanism through which the previously unidentified *C. elegans* homologue of SSNA1, referred as SSNA-1, operates at the protein level and it is involved at the major MTOC, the centrosome. To achieve this aim, we performed biochemical and biophysical investigations, that were complemented, in collaboration with Dr. Jason Pfister and Dr. Kevin O'Connell at the Laboratory of Biochemistry & Genetics (NIH-NIDDK), to genetic analysis in *C. elegans*.

The *in vitro* characterization involved the expression and purification of recombinant proteins (full-length, truncations and point mutations), that were assessed through electron microscopy, light scattering and sedimentation approaches. These techniques have allowed us to successfully characterize SSNA-1's protein structure, its oligomerization mechanism, microtubule binding, microtubule branching activity, as well as SSNA-1 binding to the centriolar Polo-like kinase 4 of *C. elegans* ZYG-1.

Alternatively, the genetic analysis has been conducted using the model organism *C. elegans*. In worms, SSNA-1 was assessed for the loss of function and its mutagenesis. The wild-type and genetically engineered strains were observed through live imaging, immunofluorescence assays, and ultimately analyzed for their embryonic viability. Those experiments have provided insights into the SSNA-1 role in regulating centriole formation, ensuring proper spindle formation and progress of cell cycle. In addition, we found that SSNA-1 can form novel satellite-like structure surrounding the PCM.

4 Materials and methods

4.1 Laboratory equipment

Table 1.1| Sorted list of main laboratory equipment used.

Description	Product	Company
Centrifuge	Avanti J-26 XPI	Beckman Coulter
Centrifuge	Avanti JXN-26	Beckman Coulter
Centrifuge	5417R	Eppendorf
Centrifuge	5424R	Eppendorf
Chromatography system	AKTA pure	GE Healthcare
Chromatography system	AKTA purifier	GE Healthcare
Chromatographic column	Superdex 75 Increase	GE Healthcare
Chromatographic column	Superdex 200 Increase	GE Healthcare
Chromatographic column	Superose 6	GE Healthcare
Chromatography resin	COmplete His-tag Purification Resin	Roche
Chromatography resin	Q Sepharose Fast Flow	GE Healthcare
Chromatography resin	SP Sepharose Fast Flow	GE Healthcare
Concentrator	Amicon Ultra Centrifugal Filter Units	Merk
Dialysis units	Slide-A-Lyzer MINI dialysis units 7K MWCO	Thermo Fisher Scientific
Dynamic light scattering	Wyatt DynaPro NanoStar DLS	Wyatt
Electrophoresis cell	Mini-PROTEAN-Tetra Cell	Bio-Rad
Electrophoresis gels	Mini-PROTEAN TGX Precast gels	Bio-rad
Electrophoresis imaging system	GelDoc Go Gel Imaging System	Bio-rad
Electron microscope	FEI Tecnai T12	Thermo Fisher Scientific
Electron microscope	Glacios	Thermo Fisher Scientific
Electron microscope	Krios G4	Thermo Fisher Scientific
Electron microscopy grid	CF200-CU	Electron Microscopy Sciences
Electron microscopy grid	Quantifoil R2/1	Quantifoil Micro Tools GmbH
Glow discharger	PELCO easyGlow Glow Discharge Cleaning System	Ted Pella, Inc.
Homogenizers	Sonoplus HD 3200	Bandelin
Incubator	New Brunswick Innova 42	Eppendorf
Incubator	Multitron Standard	INFORS AG
Photometer	BioPhotometer plus	Eppendorf
Photometer	NanoPhotometer NP80	IMPLEN
Plunge Freezer	EM GP2	Leica
Rotor	TLA-100.3	Beckman Coulter

Rotor	TLA-120.2	Beckman Coulter
Rotor	JLA-81000	Beckman Coulter
Sonicator probe	MS72	Bandelin
Spectropolarimeter	J-715	Jasco
Spectropolarimeter cuvette	High Precision Cell Quartz Suprasil	Hellma Analytics
Thermocycler	peqSTAR 2X Gradient	VWR
Thermostat	PFD-350S	Jasco
Ultracentrifuge	Optima MAX-XP	Beckman Coulter
Ultracentrifuge	Optima TL-100	Beckman Coulter

4.2 Genes preparation

The SSNA-1 gene (*C. elegans* homolog of SSNA1) was identified through UNIPROT (www.uniprot.org). The DNA sequences corresponding to the full-length protein of SSNA-1 and related mutations (either truncations or point mutations) were either synthesized (Twist Bioscience) or created by mutagenesis PCR of the synthesized genes. Every construct had 6x-His-tag and TEV-protease (3c) recognition sequence (MGKHHHHHHGSLEVLFQGP) at the N-terminus (Table 1.2).

Table 1.2| List of SSNA-1's genes created and their nomenclature.

Name	**Construct**
SSNA-1 (WT or FL)	6x::His-tag::3c::SSNA-1(1-105)
SSNA-1 (11-105)	6x::His-tag::3c::SSNA-1(11-105)
SSNA-1 (16-105)	6x::His-tag::3c::SSNA-1(16-105)
SSNA-1 (18-105)	6x::His-tag::3c::SSNA-1(18-105)
SSNA-1 (19-105)	6x::His-tag::3c::SSNA-1(19-105)
SSNA-1 (20-105)	6x::His-tag::3c::SSNA-1(20-105)
SSNA-1 (22-105)	6x::His-tag::3c::SSNA-1(22-105)
SSNA-1 (1-71)	6x::His-tag::3c::SSNA-1(1-71)
SSNA-1 (1-79)	6x::His-tag::3c::SSNA-1(1-79)
SSNA-1 (1-91)	6x::His-tag::3c::SSNA-1(1-91)
SSNA-1 (1-95)	6x::His-tag::3c::SSNA-1(1-95)
SSNA-1 (1-96)	6x::His-tag::3c::SSNA-1(1-96)
SSNA-1 (1-97)	6x::His-tag::3c::SSNA-1(1-97)
SSNA-1 (1-99)	6x::His-tag::3c::SSNA-1(1-99)
SSNA-1 (1-100)	6x::His-tag::3c::SSNA-1(1-100)

SSNA-1 (R18A/R20A/E21A/E22A or 4A)	6x::His-tag::3c::SSNA-1(R18A/R20A/E21A/E22A)
SSNA-1 (R18E/R20E/Q98E or 3E)	6x::His-tag::3c::SSNA-1(R18E/R20E/Q98E)
SSNA-1 (Y15E/Y97E)	6x::His-tag::3c::SSNA-1(Y15E/Y97E)
SSNA-1 (R18E/Y97E)	6x::His-tag::3c::SSNA-1(R18E/Y97E)
SSNA-1 (Y97E)	6x::His-tag::3c::SSNA-1(Y97E)
SSNA-1 (R18E)	6x::His-tag::3c::SSNA-1(R18E)
SSNA-1 (Y15E)	6x::His-tag::3c::SSNA-1(Y15E)

The synthesized nucleic acids were cloned into self-generated LIC (ligation-independent cloning) vectors, containing resistance for ampicillin, by Gibson assembly [119]. The standard reaction is given in Table 1.3. Additional details of chemicals and reagents used are provided in Table 1.4.

Table 1.3| Gibson assembly reaction.

Chemicals/Reagents	**Volume/quantity**
Total amount of insert	50 fmol
Total amount of vector	5 fmol
Gibson Assembly Master Mix (2X)	12 µL
ddH2O	As needed to reach total volume of 20 µL

The insert and vector were mixed in 10:1 ratio and incubated for 1 hour at 50 °C with the Gibson Assembly Master Mix. After incubation, the reaction mixture was transformed into chemically competent *E. coli* XL1 - Blue cells. For transformation, 10 µL of reaction mixture was incubated with cells for 10 minutes on ice. After 10 minutes, cells were heated at 42 °C for 45 seconds followed by incubation on ice for 10 minutes (heat-shock method). Afterwards the cells were recovered in 150 µL of SOC (Super Optimal broth with Catabolite repression) media for 30 minutes at 37 °C (while shaking) and plated on LB (Luria-Bertani) solid agar plate with ampicillin overnight at 37 °C. Single colonies were then inoculated in 5 mL of LB

media with ampicillin overnight at 37 °C. Finally, engineered vectors were purified using NucleoSpin Plasmid EasyPure kit following company's standard protocol. The sequences were confirmed by sequencing (Eurofins Genomics).

Table 1.4| Sorted list of reagents and equipment used in molecular biology.

Description	**Product**	**Company**
Bacterial media	SOC medium	Quality Biological Inc.
Bacterial media	LB (Gibco Bacto Tryptone, Yeast extract, NaCl, Agar, H2O)	Thermo Fisher Scientific (Gibco Bacto Tryptone), BD Bioscience (Yeast extract), NaCl (Merk), Agar (Merk)
E. coli	XL1 - Blue	Agilent Technologies Inc.
E. coli	BL21- Gold (D3E)	Agilent Technologies Inc.
Incubator	Thermomixer compact	Eppendorf
Molecular biology reagents	DpnI	New England Biolabs Inc.
Molecular biology reagents	Gibson Assembly Master Mix (2X)	New England Biolabs Inc.
Molecular biology reagents	NucleoSpin Plasmid EasyPure	MACHEREY-NAGEL
Molecular biology reagents	Primers	Twist Bioscience
Molecular biology reagents	Phusion High-Fidelity PCR Master Mix with HF Buffer (2X)	New England Biolabs Inc.
Molecular biology	T4 DNA ligase	Takara Bio USA Inc.
Molecular biology	T4 DNA ligase Buffer (10X)	Takara Bio USA Inc.
Molecular biology	T4 Polynucleotide kinase	New England Biolabs Inc.
Petri dishes	100 mm x 15 mm Petri Dish Stackable	CELLTREAT

Out of all the constructs in Table 1.2, the N-terminus truncations SSNA-1 (16-105) and SSNA-1 (18-105) were obtained with PCR-based mutagenesis. The general reaction mixture for such PCRs and related amplification processes are given in Table 1.5 and Table 1.6.

Table 1.5| Mutagenesis PCR reaction scheme.

Chemicals/Reagents	Volume/quantity
DNA	1 ng
Phusion High-Fidelity PCR Master Mix with HF Buffer (2X)	12.5 µL
Forward Primer	12.5 pmol
Reverse Primer	12.5 pmol
DMSO	0.42 mM

Table 1.6| PCR amplification scheme.

Step	Temperature and time
Initial denaturation	98 °C
25 cycles	98 °C for 10 minutes 65 °C for 30 minutes 72 °C for 30 seconds every kb of DNA
Final extension	72 °C for 10 minutes
Hold	8 °C

The primers for construct mutagenesis were designed such that they annealed just outside the region that needed to be deleted and would amplify the desired product (Figure 2.1). PCR products were then digested with Dpn1 (*Diplococcus pneumoniae* restriction enzyme I) for 1 hour at 37 °C, according to manufacturer's instructions, in order to cleave methylated backbone of the original template. The resulting amplified linear sequences were blunt-end ligated using T4 DNA ligase following the standard protocol from the company. The general reaction for ligation is given in Table 1.7.

Finally, the ligated products were transformed into *E. coli* XL1 – Blue competent cells by heat-shock method. After transformation, single colonies amplification and DNA purification was performed as for the plasmids generated from synthesized genes. The constructs were confirmed by sequencing (Eurofins Genomics).

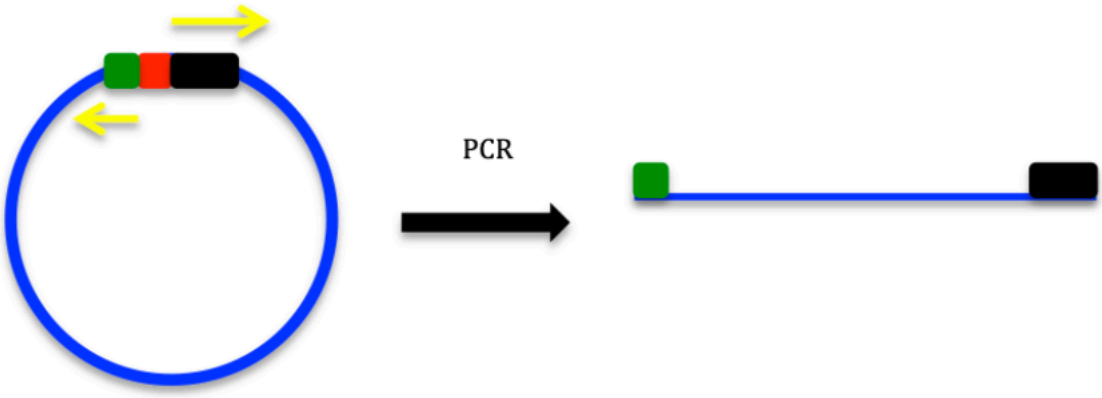

Figure 2.1| Primer design and mutagenesis PCR strategy. The blue circle shows the plasmid, the red item shows the region of the gene to be deleted, the black and the green rectangles items show the sequences to be amplified, and the yellow arrows represent the primers.

Table 1.7| Ligation reaction scheme.

Chemicals/Reagents	**Volume/quantity**
PCR product	10 µL
T4 DNA Ligase	140 U
T4 Polynucleotide kinase	20 U
T4 DNA ligase Buffer (10X)	2 µL
ddH2O	As needed to reach 20 µL

4.3 Protein preparation and purification

Protein expression and purification were performed as previously described [97]. Shortly, *E. coli* BL21(DE3) cells (Table 4.4) were transformed with recombinant SSNA-1 vectors through heat-shock method. The resulting cells were grown until OD 600 nm was about 1.6 in a solution containing 90 % TB (Terrific Broth) (v/v), 10 % P (phosphate buffer) (v/v) and 0.1 % ampicillin (v/v) at 37 °C (Table 1.8). Protein expression was induced with 0.4 mM IPTG (Isopropyl β-D-1-thiogalactopyranoside) overnight at 18 °C. The cells were harvested by centrifugation at 2541 *xg* with the rotor JLA-81000 for 10 minutes at 10 °C and resuspended with cold resuspension buffer (Table 1.8).

The lysis was performed through sonication in lysis buffer (Table 4.8) supplemented with protease inhibitors (1mM pepstinA, 1mM PMSF and 1mM leupeptin and/or cOmplete EDTA-free Protease Inhibitor Cocktail), and 10 mM imidazole (when required), for 10 minutes at 4 °C. Cell lysates were clarified through centrifugation and the resulted soluble fractions incubated for 1 hour at 4 °C with cOmplete His-Tag Purification Resin (Ni-NTA affinity chromatography). After incubation, the beads were centrifuged at 366 *xg* using centrifuge 5417R for 3 minutes at 4 °C and the flow through samples were collected. This centrifugation step was iteratively repeated to wash the beads with wash buffer I and II (Table 4.8). Washed samples were collected as well. Finally, recombinant SSNA-1 protein constructs were eluted from the beads through incubation in elution buffer (Table 1.8) for 1 hour at 4 °C and separate from the beads through centrifugation. Every specimen collected throughout the purifications was analyzed through SDS-PAGE. Proteins that required additional purification steps underwent ion exchange or size exclusion chromatography, using either Q Sepharose Fast Flow, SP Sepharose Fast Flow, or Superdex 75 Increase columns (Table 1.1). Finally, imidazole was removed from the elution buffer through dialysis at 4 °C against resuspension buffer. After dialysis, the specimens were centrifuged at 16100 *xg* at 4°C for 10 minutes to remove large oligomers and aggregates. Protein concentrations were assessed by measuring absorption at 280 nm and using extinction coefficients. Liquid chromatography mass spectrometry (LC/MS) was performed (NHLBI – Biochemistry Facility) to confirm the mass of the constructs. When required, the purified proteins were concentrated using concentrator filters with 10 kDa MWCO till 4 - 5 mg/ml. The proteins were ultimately snap-frozen in liquid nitrogen and stored at - 80 °C.

Table 1.8| Sorted list of buffers, media and chemicals used.

Buffer, media and chemicals	**Composition**
BRB80 Buffer	80 mM PIPES/KOH pH 6.8, 1 mM $MgCl_2$, 1 mM EGTA
BRB10 Buffer	10 mM PIPES/KOH pH 6.8, 1 mM $MgCl_2$, 1 mM EGTA
Elution Buffer	50 mM phosphate buffer pH 7.5, 150 mM NaCl, 10 % glycerol (v/v), 1 mM DTT, 500 mM imidazole
Phosphate buffer	0.17 M KH_2PO_4, 0.72 M K_2HPO_4-3 H_2O

Protease inhibitors	1 mM pepstinA, 1 mM PMSF, 1 mM leupeptin and/or cOmplete EDTA-free protease inhibitor Cocktail (Millipore Sigma)
Resuspension/Lysis buffer	50 mM phosphate buffer/NaOH pH 7.5, 150 mM NaCl, 10 % glycerol (v/v), 1 mM DTT
TB	12 g bacto tryptone, 24 g yeast extract, 8 mL of glycerol 50 % (v/v), H_2O as needed to reach 0.9 L of total volume
Wash buffer I	50 mM phosphate buffer pH 7.5, 1 M NaCl, 10 % glycerol (v/v)
Wash buffer II	50 mM phosphate buffer pH 7.5, 150 mM NaCl, 10 % glycerol (v/v)

Insoluble SSNA-1 constructs were purified as previously described with a buffer supplementation of 8M urea. The proteins were refolded by dialysis against resuspension buffer. Refolding was confirmed using Circular Dichroism Spectropolarimeter.

Tubulin was provided by Naoko Mizuno's lab from NHLBI-NIH and purified from porcine brains (The Bayerische Landesanstalt fur Landwirtschaft) following a previously published protocol [120].

The protein ZYG-1 was kindly prepared by Kevin O'Connell lab from NIDDK-NIH. Shortly, *E. coli* codon optimized ZYG-1 was cloned into pET21b between NheI and HindIII and expressed as C-terminal 6x-His fusion recombinant protein. The construct was transformed into T7 Express lysY/Iq Competent *E. coli* (NEB). After 4 hours induction with 1 mM IPTG at 37 °C, the cells were harvested by centrifugation and stored at - 20 °C. The cells were successively thawed, resuspended in 50 mM Tris pH 8.0, 250 mM NaCl, 5 mM DTT and lysed by sonication. The lysate was centrifuged at 20000 *xg* at 4 °C for 15 minutes. The pellet was washed twice and resuspended in the buffer described above with the addition of 8 M urea. Finally, the soluble fraction was applied on to His Trap resin (Roche) pre-equilibrated with the buffer mentioned above containing 8 M urea. Following binding, the column was washed and the bound protein was eluted with 60 mM Imidazole. The eluate containing urea denatured ZYG-1 was refolded by dialysis against the above buffer without urea. Refolding was

confirmed using Circular Dichroism Spectropolarimeter (JASCO) and *in vitro* biochemical analysis.

4.4 Protein sequences alignment and structural prediction

The protein sequences of various homologous of SSNA1/NA14/DIP13 were obtained from UNIPROT (www.uniprot.org). The sequences were aligned through M-Coffee software [121]. In addition, the sequences were also aligned through UNIPROT and represented in similarity mode. SSNA-1 structural predictions were calculated on the NIH HPC Biowulf system (http://hpc.nih.gov) through AlphaFold 2.3.2 [122], using aminoacidic sequences written into FASTA files as input.

4.5 Protein characterization through negative staining, and cryo-electron microscopy

4.5.1 Negative staining electron microscopy

Homemade carbon-coated grids were prepared and glow discharged for 45 seconds at 15 mA as plasma current. SSNA-1 constructs were applied on grids (5 µL), washed with ddH_2O and stained with 1 % (w/v) uranyl acetate or formate. The dilutions were performed with resuspension or lysis assay buffer (Table 1.8).

SSNA-1 constructs were also co-polymerized with purified brain tubulin in 1:2 ratio in BRB80 buffer (Table 1.8) supplemented with 1 mM of guanosine-5'-[(α,β)-methyleno]triphosphate (GMPCPP) for 5 minutes at room temperature and prepared for negative staining EM as mentioned above. Specifically, the specimens were incubated on carbon-coated grids for 1 minute at room temperature, washed twice with BRB80 buffer and/or ddH_2O and stained with uranyl acetate or formate for 1 minute.

Finally, the negatively stained samples were observed using FEI Tecnai T12 at 120 kV using different magnifications.

4.5.2 Cryo-EM sample preparation, data collection, and image processing

Fibrils of SSNA-1 (3E) were grown through overnight dialysis against resuspension or lysis buffer at 4 °C and applied on glow discharged Quantifoil grids R2/1 (t = 45 seconds, I = 15 mA) as 5 µL droplet with a final concentration of 0.1 mg/mL. After 1 minute incubation at

room temperature, the grid was manually blotted on the side with filter paper (Whatman Cat No 1001 125) and 4 µL of a solution containing 50 mM Phosphate buffer/NaOH pH 7.5, 150 mM NaCl, 1 mM DTT, 0.1 % octyl beta-D-glucopyranoside (v/v) was applied. Afterwards, the grid was transferred into EM GP2 (Leica) plunge chamber operating at 15 °C and max humidity (100 %), incubated 1 minute and vitrified in liquid ethane (using 212, 3.8, and 5.5 mm as blot settings, grid blot and TF position respectively). The grid was successively loaded on Krios G4 (ThermoFisher Scientific), equipped with a Gatan BioContinuum energy filter (slit width 20 eV) and K3 Summit direct detector electron camera at an acceleration voltage of 300 kV. Movies were recorded by EPU in super-resolution mode resulting in a raw pixel size of 0.412 Å with defocus range varying from - 0.5 to - 2.3 µm (0.2 µm steps). In total, 10396 movies were acquired with each movie having 40 frames and a total dose of 40.84 e-/Å2. The image processing was performed in cryoSPARC (v. 3.3.1 and v. 4.1.1) [123]. Movies underwent patch motion correction with output Fourier cropping factor of ½ resulting in a pixel size of 0.82 Å. After dose weighting and motion correction, CTF measurements were performed via patch CTF and 8390 exposures were selected for further processing. An initial set of helical particles were auto picked with filament tracer, extracted with a box size of 512 pixels, F-cropped to 256 pixels, resulting in a pixel size of 1.648 Å, and classified through 2D classification. The best classes were selected and used as templates for multiple rounds of auto-picking until satisfying 2D classes. Ab-initio and helix refinements were performed using C1 as point group symmetry to obtain the initial map. Those particles underwent 3D classification and each of the resulted 3D classes (6 classes) was subsequentially used for another round of 3D classification. Out of 36 volumes, 6 of them were selected (including their corresponding particles) to further perform multiples rounds of 3D classification and hetero refinement. One class of particles (42005) was successively selected and used to create artificial 2D projections through create templates job in cryoSPARC. These 2D projections acted as templates to perform a new round of particles picking through filament tracer. The new stack of particles (1626072) underwent several rounds of 2D classification until 700986 particles were selected for final processing. After re-extraction of the selected particles, with a box size of 512 pixel and a pixel size of 0.82, we obtained the final map through helix reconstruction using C8 as point group symmetry. The map was analyzed for its flexibility through flexible refinement. The final set of particles were also re-extracted with a box size of 1024 pixel, F-cropped to 512 pixels (with a pixel size of 1.648 Å), and the resulted 2D classification results were used to calculate the averaged power spectrum through Fiji [124]. All 3D reconstructions were visualized in Chimera X [125].

4.5.3 Model building

SSNA-1 structures were predicted on the NIH HPC Biowulf system through AlphaFold 2.3.2 [122]. For our model building strategy, we first fit the most accurate SSNA-1 (3E) AlphaFold prediction into the cryo-EM map in Chimera X [125] and perform rigid body fit in Coot [126]. The resulted structural model had the residues M1-S8, that were predicted to be part of the coiled-coil by AlphaFold, involved in steric clashes. However, we observed from our cryo-EM map an extra density from the residue F9, protruding inward the filament and that would connect to the inner lumen disordered region. This observation, along with our CD data, suggested an unstructured N-terminus. Additionally, the AlphaFold prediction of the fragment SSNA-1 (1-18) would resemble the disordered structure observed in the inner lumen, confirming our previous observations. Taking these findings into considerations, we calculated a new AlphaFold prediction using the sequence SSNA-1 (3E_7-105) and further used it to create a model in which the structured helices at the N-terminus of SSNA-1 (3E) would start from S8-F9. The final model was created by using such AlphaFold prediction, that underwent fitting through Chimera X, rigid body fit though Coot, real space refinement as well as validation through Phenix [127]. Figures of the structural model were created with Chimera X. The neighboring residues and the likely interactions of the structural model were analyzed through LIGPLOT [128].

4.6 Sedimentation assay

SSNA-1 was assessed for microtubule binding through sedimentation of purified proteins (*in vitro* reconstitution). Tubulin was pre-polymerized for half an hour at 37 °C in BRB80 buffer supplemented with 1 mM GMPCPP. SSNA-1 constructs were pre-sedimented twice at 16100 *xg* using the rotor TLA-120.2 for 10 and 5 minutes, respectively, at 25 °C to remove large oligomers and aggregates. Soluble SSNA-1 was successively dialyzed against BRB10 buffer (Table 1.8) for 5 minutes, and incubated for 4 minutes at room temperature with pre-polymerized MTs. The final reactions had a total volume of 30 µL with a concentration of each protein of 20 µM and were sedimented at 9776.5 *xg* using the rotor TLA-120.2 for 10 minutes at 25 °C. The supernatants and pellets were then recovered and analyzed via SDS-PAGE. Bands intensity and data analysis were performed using Fiji [124]. Data was plotted with Prism (www.graphpad.com).

SSNA-1 was also assessed for ZYG-1 binding as follow. SSNA-1 was dialyzed against resuspension buffer, overnight at 4 °C, to grow fibrils and successively incubated at room temperature for 10 minutes with ZYG-1. The final reactions had a total volume of 30 µL and concentrations of ZYG-1 and SSNA-1 of 1.25 µM and 10 µM, respectively. The sedimentation steps were performed at 278088 *xg* with the rotor TLA-120.2 for 10 minutes at 25 °C. Similarly, we tested the binding of ZYG-1 and pre-polymerized MTs as well as SSNA-1 and BSA. While the final concentrations of ZYG-1 and SSNA-1 were kept the same as the previous experiments, MTs and BSA were 10 µM and 1.25 µM, respectively. The analysis was carried out through SDS-PAGE (through coomassie or oriole staining) and/or western blot using mouse monoclonal anti-FLAG M2 F1804 (Sigma-Aldrich), mouse monoclonal anti-alpha-tubulin DM1A (Sigma-Aldrich) and rabbit polyclonal anti-recombinant-SSNA-1 (Yenzym Antibodies), for ZYG-1, alpha-tubulin, and SSNA-1 detection, respectively. The antibodies were used at a dilution of 1:1000. Bands intensity and data analysis were performed using Fiji. Data was plotted with Prism.

4.7 Circular dichroism (CD) spectroscopy

The CD spectra were recorded on a Jasco J-715 spectropolarimeter equipped with Peltier thermostat (Max Planck Institute of Biochemistry, Munich, Germany). The system was connected to the Spectra Manager software J700 for signal averaging and processing. The calibration of the instrument was carried out using d-10-camphorsulfonic acid as a standard substance over the range 350 - 180 nm. Measurements were obtained in cuvettes (High Precision Cell Quartz Suprasil, Table 1) of 0.1 cm optical path-length over the range 195 - 250 nm at 4 °C with 100 mdeg of sensitivity, continuous scanning mode, 100 nm/min scanning speed, and 4 accumulation spectra. The average of 4 scans is expressed as ellipticity per mole of peptide residues [θ_R].

As described above, the imidazole in the SSNA-1 protein solution was previously removed by dialysis against resuspension buffer. After buffer exchange, the specimens were centrifuged to remove any aggregates at 16100 *xg* for 10 minutes at 4 °C. The proteins were then diluted in resuspension buffer (Table 1.8) to 0.1 mg/mL (final concentration) and used for the measurement. Data was plotted with Prism.

The unfolding curves were also obtained by following the change in intensity of the CD signal at 222 nm as a function of temperature over the range of 4 - 90 °C. For thermal denaturation,

the protein samples were prepared as mentioned above and the samples were heated by a Peltier thermostat at a heating rate of 60 °C/hour. Data was plotted with Prism.

4.8 Dynamic light scattering (DLS)

DLS analyses was performed to detect oligomerization states of SSNA-1 and which regions of the protein were involved in its self-assembly. Measurements were acquired using Wyatt DynaPro NanoStar DLS (Table 1.1). The instrument was calibrated with a laser wavelength of 658 nm and scattering angle of 90 °.

The proteins underwent triplicated measurements, where every measurement consisted of 10 acquisitions for 1 minute (acquisition time 5 seconds and read interval 1 second) at 20 °C. Finally, the data were processed with Dynamics v7.4.0 software (Wyatt) and both cumulant and regularization analysis were presented with Prism.

4.9 *C. elegans* strain preparation, and maintenance

C. elegans strains were prepared and examined by Dr. Jason Pfister from Dr. Kevin O'Connell lab (NIDDK-NIH). The strains used in this study are described in Table 1.9.

4.9.1 CRISPR-Cas9 genome editing

CRISPR-Cas9 genome editing was performed as previously described by Dr. Jason Pfister at NIH-NIDDK [129,130]. Primers and oligonucleotide repair templates were purchased from Integrated DNA technologies (Table 1.10). CRISPR RNAs (CrRNAs) were purchased from Dharmacon, Inc. Cas9 protein was purified as previously described [130].

4.10 Embryonic viability assay

For quantification of embryonic viability, L4 larvae were individually picked to a 35 mm MYOB agar plate at the indicated temperature and allowed to become gravid for 1 day. Worms were then singled to new 35 mm plates and allowed to lay eggs after which the adult worms were removed, and the eggs were allowed to hatch. Total progeny, unhatched eggs and hatched worms, were then manually counted. The analysis was presented with Prism.

4.11 Fixed and live imaging

Immunofluorescence microscopy was performed as previously described [131], using the following antibodies. Mouse monoclonal anti-alpha-tubulin DM1A (Sigma-Aldrich) and rabbit polyclonal anti-SAS-4 were used at a dilution of 1:1000. Alexa Fluor 488 anti-rabbit and Alexa Fluor 568 anti-mouse (ThermoFisher Scientific) secondary antibodies were used at a 1:1000 dilution. The SPOT tag was detected using the SPOT-Label Alexa Fluor 568 (ChromoTek) at a dilution of 1:1000.

Specimens were fixed in methanol at room temperature, as previously descibed [131], and imaged by spinning disk confocal microscopy using a Nikon Eclipse Ti microscope equipped with a Plan Apo VC 60x 1.4 N.A. oil immersion lens, a CSU-X confocal scanning unit (Yokogawa Electric Corporation), and an Orca-FusionBT C15440 digital camera (Hamamatsu Photonics). Excitation light was generated using 405 nm, 488 nm, and 561 nm controlled via a Nikon LunF-XL solid state laser source (Nikon Instruments, Inc). Images were acquired using NIS-elements software (Nikon Instruments, Inc).

Time-lapse imaging was performed by spinning disk confocal microscopy using a Nikon TE2000U inverted microscope equipped with a Plan Apo 60x 1.4 N.A. oil immersion lens, a Thermo Plate heating/cooling stage (Tokai Hit) and a C9100-13 EM-CCD camera (Hamamatsu Photonics). Excitation light was generated using 405 nm, 491 nm, and 561 nm solid state lasers controlled by a LMM5 laser launch and fed through a Borealis beam conditioning unit (Spectral Applied Research). MetaMorph software was used to acquire images (Molecular Devices).

Image processing was performed using either Fiji or NIS-elements software (Nikon Instruments, Inc). Data were plotted with Prism.

Table 1.9| *C. elegans* strain genotypes.

N2	**Wild type**
OC1002	*zyg-1 (bs197[zyg-1::spot]) II*
OC1013	*bsSi30[pCW9: unc-119(+) pcdk-11.2::sfgfp::his-58::cdk-11.2 3′ utr] II; bsIs20[pNP99: unc-119(+) tbb-1p::mCherry::tbb-2::tbb-2 3′-utr]; bsIs2 [pCK5.5: Ppie-1::gfp::spd-2]; ssna-1 (bs182) / dpy-9 (tm9713) kvs-5 (tmIs1245)] IV*
OC1014	*ssna-1(bs182) / dpy9 (tm9713) kvs5 (tmIs1245) IV*
OC1018	*ssna-1 (bs206 [ssna-1::spot]) IV*
OC1021	*zyg-1 (bs197 [zyg-1::spot] II; ssna-1 (bs182) IV*

OC1040	*sas-4(bs195 [sas-4::GFP]) III; ssna-1 (bs206 [ssna-1::spot]) IV*
OC1041	*pie-1::GFP::spd-5; ssna-1 (bs206 [ssna-1::spot]) IV*
OC1043	*ssna-1 (bs215[R18A]) IV*
OC908	*bsSi30[pCW9: unc-119(+) pcdk-11.2::sfgfp::his-58::cdk-11.2 3′ utr] II; bsIs20[pNP99: unc-119(+) tbb-1p::mCherry::tbb-2::tbb-2 3′-utr]; bsIs2 [pCK5.5: Ppie-1::gfp::spd-2]*
OC1045	*ssna-1 (bs217[R1820A, E21/22A]) IV*
OC1052	*ssna-1 (bs220 [1-99])/dpy9 (tm9713) kvs5 (tmIs1245) IV*
OC1068	*ssna-1 (bs222 [G7X])/dpy9 (tm9713) kvs5 (tmIs1245) IV*
OC1070	*ssna-1 (bs224 [Δ2-22])/dpy9 (tm9713) kvs5 (tmIs1245) IV*
OC1072	*ssna-1 (bs231 [Δ2-17])/dpy9 (tm9713) kvs5 (tmIs1245) IV*
OC1073	*ssna-1 (bs232 [Δ2-17])/dpy9 (tm9713) kvs5 (tmIs1245) IV*
OC1076	*ssna-1 (bs235 [Δ2-18])/dpy9 (tm9713) kvs5 (tmIs1245) IV*
OC1134	*sas-6 (bs190 [sas-6::spot]) IV*
OC1135	*ssna-1(bs182), sas-6 (bs190 [sas-6::spot]) IV*
OC1138	*ssna-1(bs182)/ears-2(ve631[LoxP + myo-2p::GFP::unc-54 3′ UTR + rps-27p::neoR::unc-54 3′ UTR + LoxP]) IV*
OC1185	*ssna-1(bs249 [ssna-1(4A)::spot]) IV*

Table 1.10| CrRNAs and repair templates used in this study.

Allele	Background	crRNA (5’ -> 3’)	Repair template (5’ -> 3’)
bs206	N2	CTTTGTGCGCAAAGTATC	GCAAAAGACGTTGGTGGACTTTGTGCGCAAAGAGTATCAAGATACGAAACATCAGAAATATCCAGACCGTGTCCGTGCCGTCTCCCACTGGTCCTCCTGAACTCTGAACAACTGTCTCCCAAAAATGCCTGTAAATATATCAATTATCGACATAACTTC
bs249	bs217	GATATATTTACAGGCATTTT	
bs182	N2	TAGAATCATGCATTTGCATT CTTTGTGCGCAAAGAGTATC	TTCGTATTTGAACAATTACTGACTAATTTCCTCCGAATGCAAATGCATGATTCTAGAACAAAAAAAACATCAGAAATATTGAACTCTGAACAACTGTCTC
bs215	N2	CTGTGAGACGGCGTTCCTCT	GAAGATAAACATTTATAGTAATATTTCAGACATCCAAGCGCTCAGAGAGGAACGCCGTCTCACAGAATCGTCGATTCGAAAAATG
bs217	bs215	AGACATCCAAGCGCTCGCGG	GTAAGAGCAAATTGAAGATAAACATTTATAGTAATATTTCAGACATCCAAGCGCTCGCGGCAGCACGCCGTCTCACAGAATCGTCGATTCGAAAAATGGAAA

bs220	N2	CTTTGTGCGCAAAGAGTATC	GCAAAAGACGTTGGTGGACTTTGTGCGCAAAGAGTATCAAGATTGAACTCTGAACAACTGTCTCCCAAAAATGCCTGT
bs222	N2	AAAATGTCTTCTCGATCTAC	TGCATGATTCTAGAACAAAAAATGTCTTCTCGATCTACATGAAGCTTTGATGAAATATCACAGTGTAAGAGCAAATT
bs224	bs215	AAATGTCTTCTCGATCTAC AGACATCCAACGTCTCCGAG	CCGAATGCAAATGCATGATTCTAGAACAAAAAATGCGCCGTCTCACAGAATCGTCGATTCGAAAAATGGA
bs231	N2	AAAATGTCTTCTCGATCTAC CTGTGAGACGGCGTTCCTCT	CCGAATGCAAATGCATGATTCTAGAACAAAAAATGCGTCTCAGAGAGGAACGCCGTCTCACAGAATCGTCGATTCGAAAAA
bs235	N2		CCGAATGCAAATGCATGATTCTAGAACAAAAAATGCTCAGAGAGGAACGCCGTCTCACAGAATCGTCGATTCGAAAAA

5 Results

5.1 SSNA-1 (*C. elegans*) shares high similarity with other homologues

The SSNA1 protein family has been identified in many eukaryotes such as mammals, trematode, protozoan and fish genomes, indicating an ancestral function [101]. Interestingly, all these species have centrioles, cilia and/or flagella, with SSNA-1 localizing at such microtubule organizing centers [97,98,101-105]. In *C. elegans*, however, a model organism that has been extensively used for centriole characterization [59], there has been no evidence that reported the presence of such protein. Here, we validated the sequence of the *C. elegans* SSNA1, called SSNA-1, and its homology through the alignment of its amino acid sequence with others (Figure 3.1). The multiple sequence analysis of those homologues showed high alignment accuracy with an overall consistency value of 92, indicating that the aligned sequences were matched correctly and consistently across the dataset (Figure 3.1).

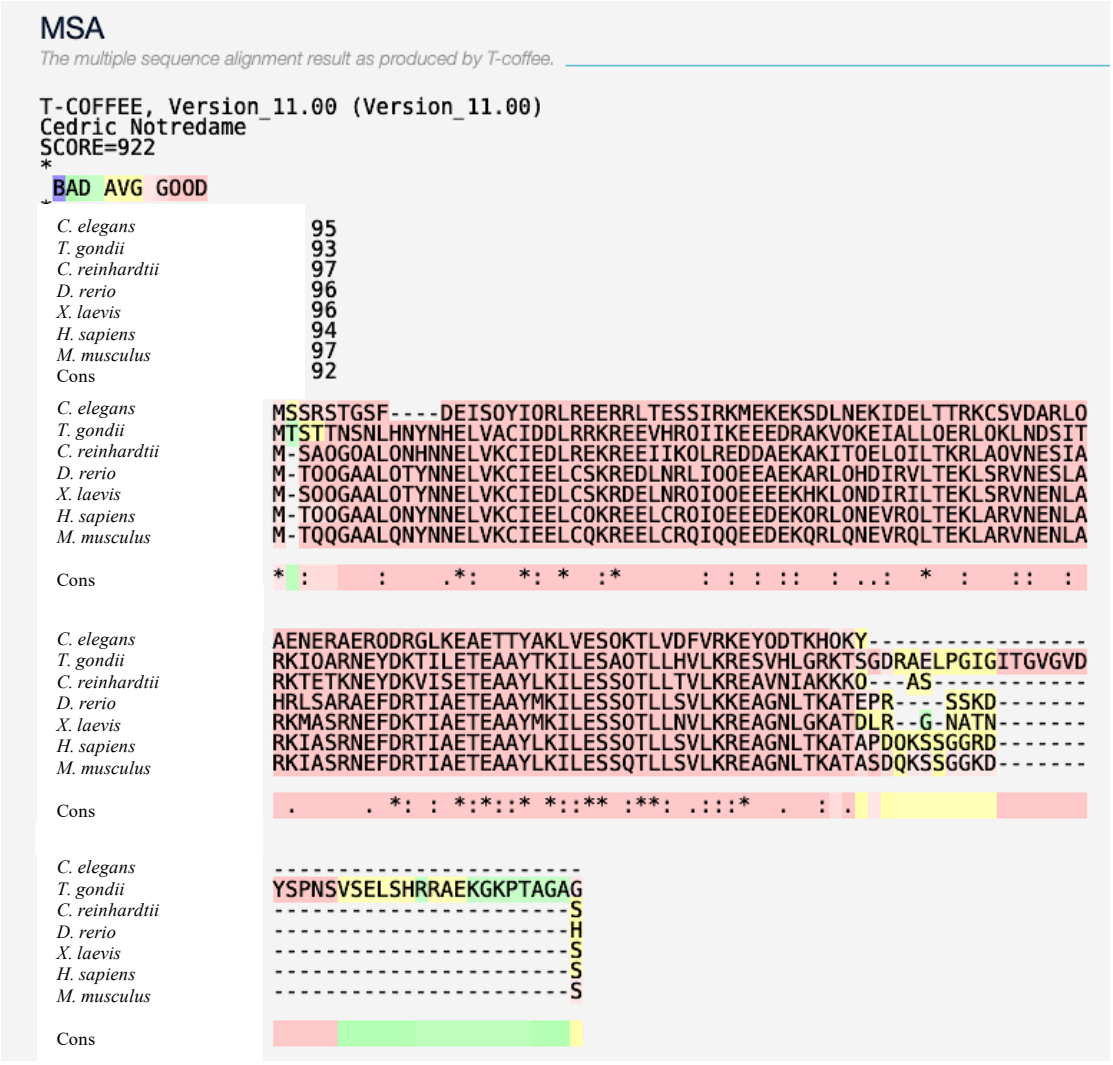

Figure 3.1| SSNA1/DIP13/NA14 protein sequence alignment (using T-coffee).

Accordingly, the chemical-physical properties of these homologs appeared to be redundant with most of the amino acids conserved and/or with similar functions (Figure 3.1 and 3.2). Although the whole sequence is reasonably conserved, C-terminal tails show different coverage likely indicating species-specialized domains.

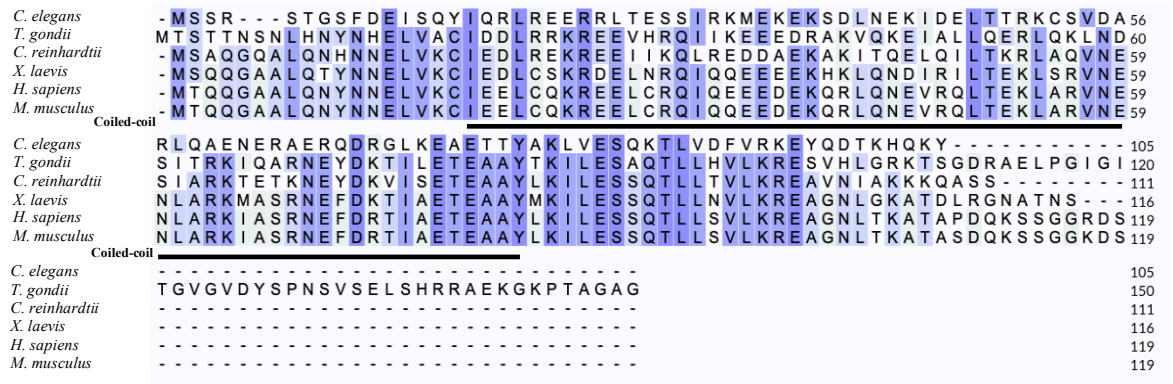

Figure 3.2| SSNA1/DIP13/NA14 protein sequence alignment highlighting residue similarity. The blue highlight is based on the chemical-physical similarity of amino acids, such as charged, polar, and hydrophobic functions. Different shades of blue indicate varying degrees of similarity: darker blue represents a higher similarity, while lighter blue indicates a lower degree of similarity. Image is created from UNIPROT. The coiled-coiled region is a predicted coiled-coil region conserved across species.

5.2 Cryo-EM analysis of SSNA-1 reveals dimeric coiled-coils connecting through triple-stranded helical junctions

SSNA1 forms a filamentous polymer, but the mechanism of assembly and its functional significance are unclear [97,98,101-104]. To gain insights into the mechanism, we purified the *C. elegans* SSNA-1 and characterized its biochemical and biophysical properties (Figure 3.3). Consistent with our previous findings [97], we observed bundled filaments formed by SSNA-1, which were not suitable for structural analysis. To obtain a structurally amenable form of SSNA-1, we introduced a series of point mutants at both N- and C- terminus, and identified a mutant variant, SSNA-1 (3E), with the mutations R18E/R20E/Q98E, showing filaments with no bundles which were suitable for further structure determination (Figure 3.3).

Cryo-EM analysis of SSNA-1 (3E) revealed the presence of eight parallel fibrils assembled into filaments with C8 symmetry (Figure 3.4 and 3.5). The outer and inner diameters of the filaments were 90 Å and 55 Å, respectively (Figure 3.4). The 8 fibrils were bundled together and had a density within the inner lumen of the filament, exhibiting a periodicity of 112 Å, which was validated by the averaged power spectrum of the aligned filaments (Figure 3.4 and 3.5). Within each fibril, individual protomers were arranged as dimeric coiled-coils,

longitudinally connected to the next dimeric coiled-coil units with the same periodicity (112 Å) as the inner lumen density (Figure 3.4 and 3.5). The connection between adjacent coiled-coil dimers was mediated by an unusual triple-stranded helical junction (Figure 3.4 and 3.5). Although the resolution of our 3D reconstruction was moderate (6.8 Å - 0.143 criterion) (Table 2.2), due to the inherent flexibility of SSNA-1 (Figure 3.5), we complemented our analysis with AlphaFold structural prediction to create a hybrid structural model (Figure 3.6) (Table 2.1, 2.2, and 2.3), which validated the presence of the triple-stranded helix junction.

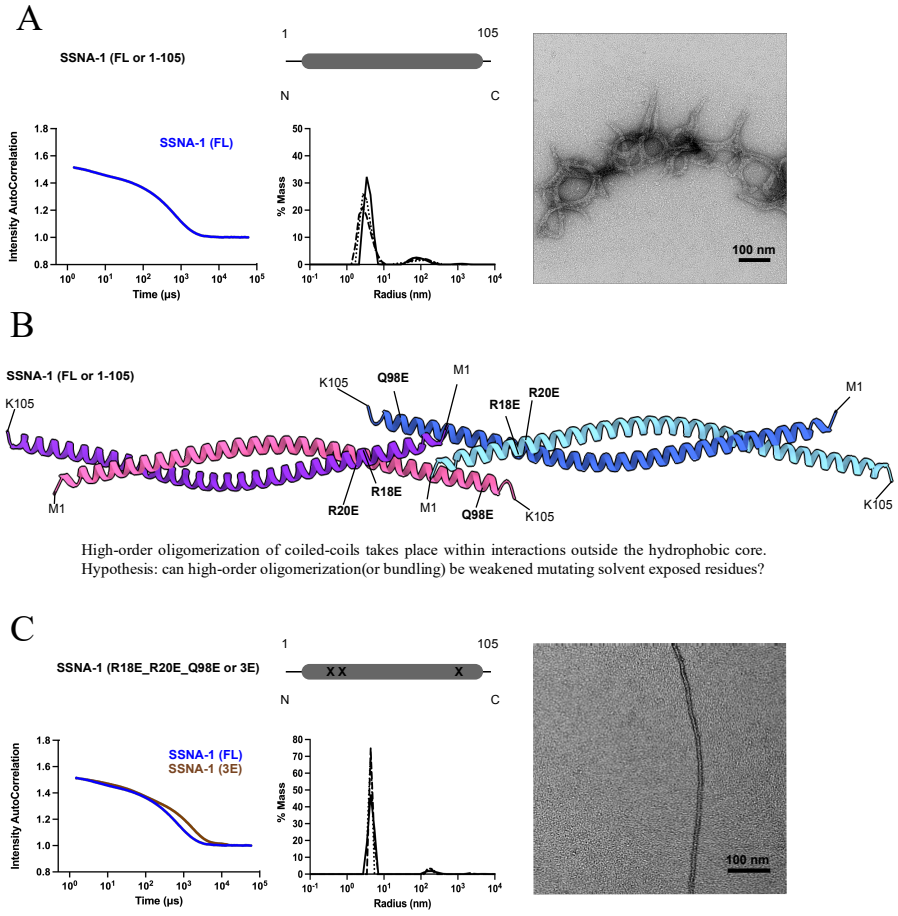

Figure 3.3| Mutagenesis strategy to obtain structurally amenable form of SSNA-1. A| Top left: schematic view of SSNA-1 (FL) protein construct. Bottom left: Autocorrelation curve of SSNA-1 (FL) measured through DLS and related hydrodynamic radii distribution of SSNA-1 (FL) particles. SSNA-1 (FL) had a decay of the autocorrelation function at 5324.8 µs. The hydrodynamic radii distribution (measured from the Autocorrelation curves) of SSNA-1 (FL) revealed a heterogeneous distribution of particles with two peaks, one between 10^0 and 10^1 nm (representing small oligomers) and another at about 10^2 nm (indicating big oligomers). Right: Negative staining EM of SSNA-1 (FL) showed filamentous bundles, which is a result in line with the peak observed for bigger oligomers. Small oligomers were observed with difficulty due to resolution limitation of negative staining EM. Scale bars refer to 100 nm. **B|** AlphaFold prediction of tetrameric SSNA-1 (FL) shows two antiparallel coiled-coils polymerized via a three-stranded helical junction. The residues highlighted in bold (R18/R20/Q98) were chosen as point mutation sites to create a less bundled version of SSNA-1. The statement regarding the high-order oligomerization of coiled-coils is extracted from Ciani B. et al, 2010, Charest G. et al, 2006, and Lupas A. et al,

2006. **C**| Top left: schematic view of SSNA-1 construct (3E). Bottom left: Autocorrelation curves of SSNA-1 (3E) and (FL) measured through DLS and related hydrodynamic radii distribution of particles. SSNA-1 (3E) had a decay of the autocorrelation function at 15564.8 µs. The hydrodynamic distribution of SSNA-1 (3E) also reveals a heterogeneous distribution of particles characterized by one peak between 10^0 and 10^1 nm (representing small oligomers) and another peak at about 10^2 nm (indicating big oligomers). Right: Negative staining EM of SSNA-1 (3E) showed filaments with no bundles, which is a result in line with the peak observed for bigger oligomers. Small oligomers were observed with difficulty due to resolution limitation of negative staining EM. Scale bars refer to 100 nm.

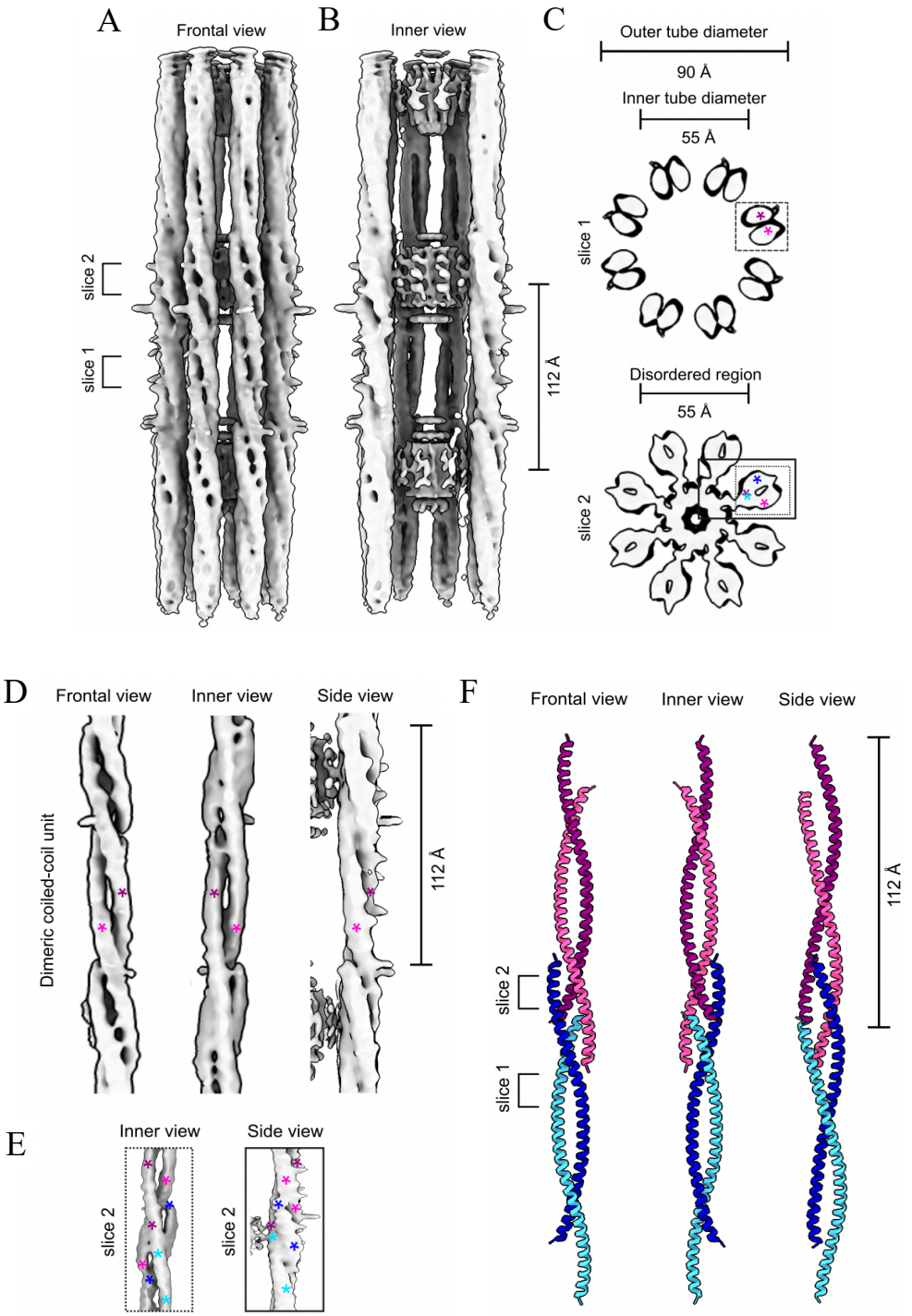

Figure 3.4| Cryo-EM analysis of SSNA-1 (3E). A, B| Frontal view (A) and inner view (B) of SSNA-1 (3E) filament obtained through helical reconstruction (grayscale 0.07). **C|** Top: orthogonal view of dimeric coiled-coils (protomers) arranged in the filament (slice 1). Bottom: orthogonal view of two different protomers (dimeric coiled-coil units) connecting through three-stranded helical junctions. Such density extends to a disordered region at the inner lumen (slice 2). **D|** Frontal, inner, and side views of a single fibril protomer (dimeric coiled-coil unit). **E|** Left: inner view of the density representing the connection of two different protomers within the same fibril (three-stranded junctions) (slice 2). Right: side view of a three-stranded junction where the density extends to the inner lumen to form a disordered structure (slice 2). The asterisks represent the EM density corresponding to the helices of the structural model. **F|** Frontal, inner, and side views of our SSNA-1 (3E_7-105) hybrid structural model. The coiled-coiled are connected to the next ones with the same periodicity (112 Å) as the inner lumen density.

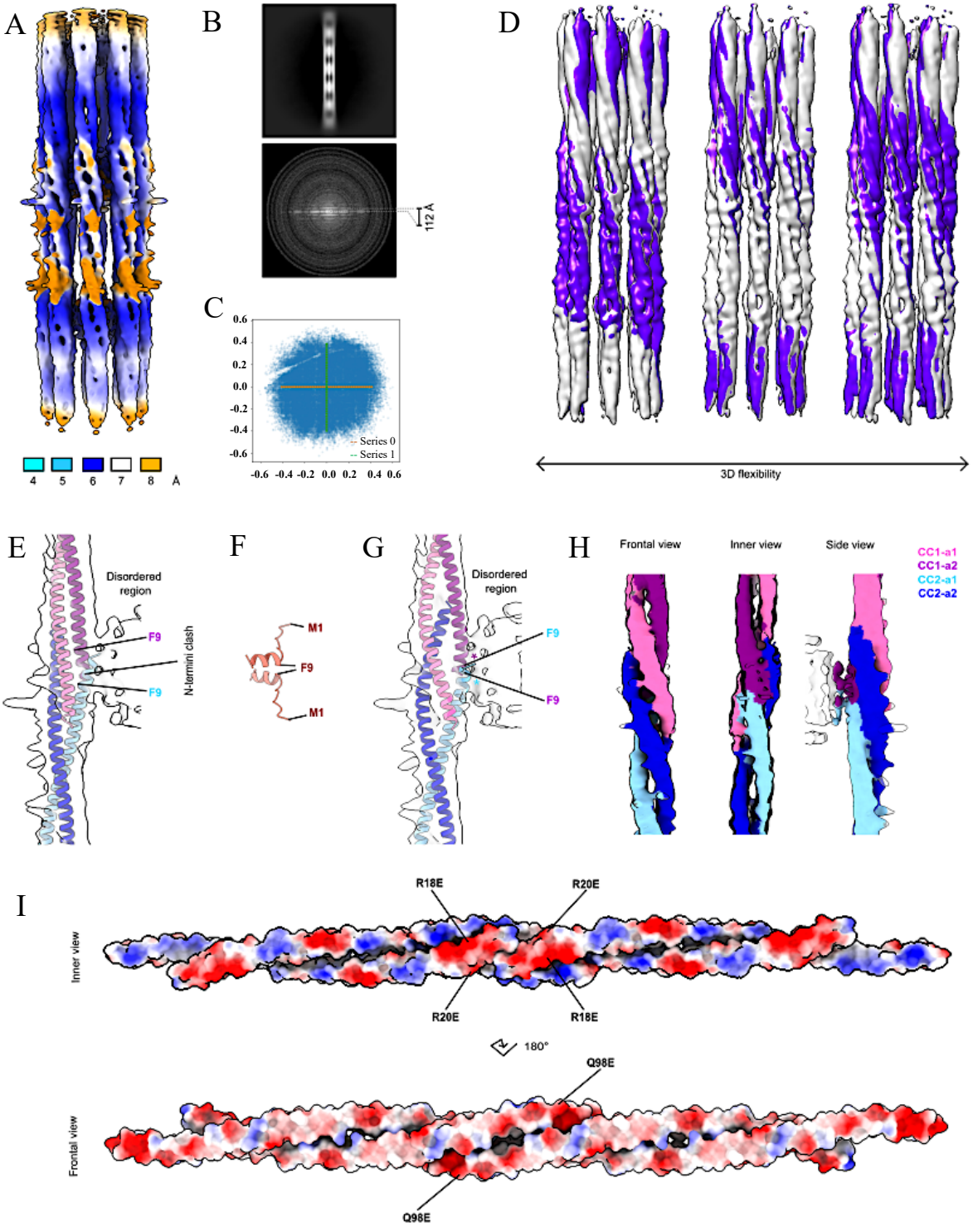

Figure 3.5| Additional data of the structural analysis and model building strategy. A| Local resolution estimation of SSNA-1 (3E) cryo-EM map. Bottom: different colored squares refer to different resolution expressed in Å. **B|** Top: 2D average of SSNA-1 (3E) with box size of 512 pixel and pixel size of 1.648 Å. Bottom: averaged power spectra of SSNA-1 (3E) with layer lines in grey showing helical periodicity. The helical repeat was calculated as 112 Å. **C|** Latent space distribution in two dimensions (dim 0 and dim 1) of the two series of volumes generated from the 3D Flexible model. **D|** Representation of three frames (out of 41) of the two volumes series obtained from 3D Flexible Refinement. Two maps (in violet and silver) were created to describe the non-linear non-rigid deformation and show the flexibility of the reconstructed map. **E|** Representation of SSNA-1 (3E_1-105) AlphaFold model modified through rigid body method in Coot fitting the cryo-EM density of a single fibril of SSNA-1 (3E). Such model illustrates that N-terminal residues of different protomers would clash from M1 to S8. **F|** The AlphaFold prediction of SSNA-1 (1-18) shows how the disordered N-termini of two different protomers could potentially fold and create the disordered region observed at the lumen of the filament. **G|** Representation of the SSNA-1 (3E_7-105) structural model fitting cryo-EM density of a single fibril of SSNA-1 (3E). According to our analysis, such EM map interpretation, CD analysis (Figure 5.8), and AlphaFold predictions (Figure 5.3), we created a structural model that would not have the N-termini clash previously observed, as M1 - S8 are likely disordered creating an unstructured N-terminus. **H|** Representation of SSNA-1 (3E_7-105) structural model (frontal, inner, and side views, respectively) where the cryo-EM density has been colored with the same color of the corresponded structural model chain fit into it. **I|** Columbic electrostatic potential (EPS) of SSNA-1 (3E_7-105) structural model (frontal and inner views) calculated in Chimera X (Amber 20). The residues highlighted in bold (R18/R20/Q98) were chosen as point mutation sites to create a structure amenable form of SSNA-1.

Our structural model revealed that the dimeric coiled-coil within each repeating unit or protomer (CC1-a1 and CC1-a2) is assembled in an antiparallel manner, spanning residues 9-105 (Figure 3.6) (Table 2.1, 2.2, 2.3). The density upstream of residue F9 extended and connected to the inner lumen density (Figure 3.4 and 3.5), suggesting that this disordered region corresponds to the assembly of the amino acids M1 - S8 from the two coiled-coil dimers of the eight fibrils in the filament, with the total density accounting for 128 amino acids (13 kDa). Accordingly, the CD spectra analysis indicated that this portion of SSNA-1 is likely disordered, with a higher disordered percentage observed in full-length SSNA-1 (1-105) (27.5 %), compared to a truncation construct SSNA-1 (12-105) (9.4 %) (Figure 3.8). Furthermore, these observations are in line with the AlphaFold prediction of the N-terminal amino acids M1 - R18, showing that amino acids 1 - 8 are disordered (Figure 3.5).

At the helical junction connecting neighboring coiled-coil fibril units, two tandem triple-stranded junctions (junction 1 and 2) were observed (Figure 3.6). The over-hanged C-terminus of the first coiled-coil (CC1-a1) formed a triple-stranded helix with the pair of the second coiled-coil (CC2). Similarly, the C-terminus of CC2-a2 interacted with the coiled-coils of CC1. The junction interfaces were stabilized through hydrophobic, charged, and polar residues, forming a classical coiled-coil structure. Those interfaces were formed through specific interactions between key amino acids, namely T26 (CC1-a2) - K104 (CC2-a2), E22 (CC1-a2) - K104 (CC2-a2) - T100 (CC2-a2), R18E (CC1-a2) - Y97 (CC2-a2), Y15 (CC1-a2) - V93 (CC2-a2), I12 (CC1-a2) - L89 (CC2-a2), R23 (CC1-a2) - Q68 (CC1-a1), L19 (CC1-a2) - Y79 (CC1-a1), P9 (CC1-a2) - P9 (CC2-a1), V93 (CC1-a1) - I12 (CC2-a1), R94 (CC1-a1) -Y97

(CC1-a1) - E11 (CC2-a1), E96 (CC1-a1) - Y15 (CC2-a1), T100 (CC1-a1) - Y15 (CC2-a1), K104 (CC1-a1) - E22 (CC2-a1), and Q103 (CC1-a1) - T26 (CC2-a1). The junction was further stabilized by interactions between CC1-a1 and CC2-a2, creating a third interface through hydrophobic, charged, and polar interactions. Similar to the junctions, the center of dimeric coiled-coils units is stabilized by a canonical hydrophobic core, charged, and polar residues.

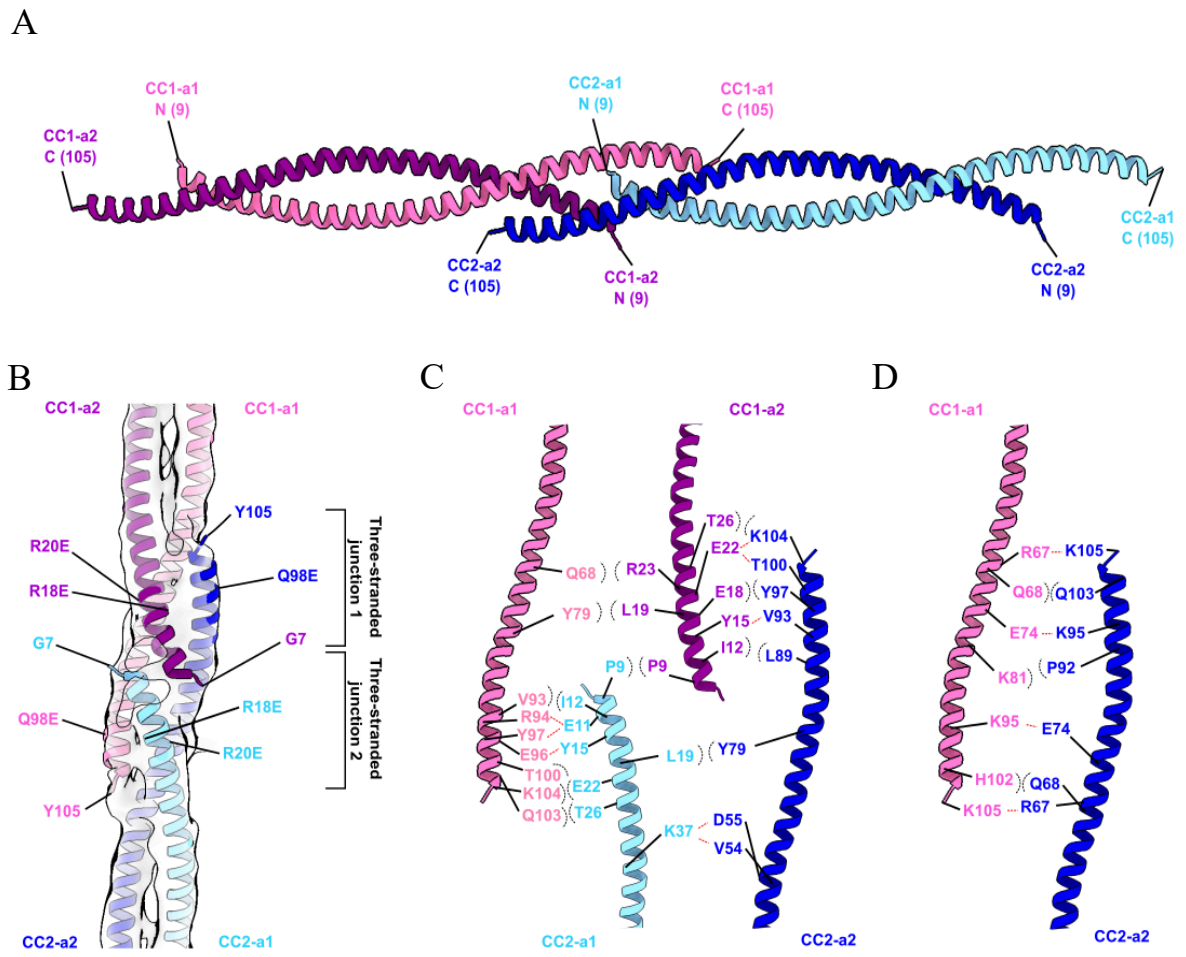

Figure 3.6| Structural model of SSNA-1 (3E_7-105). A| SSNA-1 (3E) fibrils are formed by antiparallel dimeric coiled-coils (CC1-a1, CC1-a2, CC2-a1, and CC2-a2) that interact through three-stranded helical junctions. CC1-a1 is colored in hot pink. CC1-a2 is represented in purple. CC2-a1 is highlighted in light blue. CC2-a2 is indicated in blue. The amino acids show the N- and C-termini of the helices. **B|** The image describes the three-stranded helical junctions arranged in tandem. The structural model is fit into the cryo-EM density. The point mutations R18E/R20E/Q98E shown were created to obtain the structurally amenable form of SSNA-1. **C-D|** The three-stranded helical junction is characterized by a hydrophobic core that gets stabilized and/or shielded from the solvent interface by neighboring hydrophilic and charged residues. While in C we show two interfaces of interaction (three-stranded helical junctions), in D we describe the third interface of interaction that is characterized by antiparallelly oriented C-termini of two different protomers (or coiled-coil units). The dotted parenthesis and red lines represent interactions between neighboring residues.

Table 2.1| Structural model summary. The analysis was performed using Phenix 0.9.

Composition (#)	
Chains	4
Atoms	3316 (Hydrogens: 0)
Residues	Protein: 396 Nucleotide: 0
Water	0
Ligands	0
Bonds (RMSD)	
Length (Å) (# > 4σ)	0.004 (0)
Angles (°) (# > 4σ)	0.955 (0)
MolProbity score	2.03
Clash score	33.95
Ramachandran plot (%)	
Outliers	0.00
Allowed	2.06
Favored	97.94
Rama-Z (Ramachandran plot Z-score, RMSD)	
whole (N = 388)	1.85 (0.40)
helix (N = 388)	1.29 (0.25)
sheet (N = 0)	--- (---)
loop (N = 0)	--- (---)
Rotamer outliers (%)	0.00
Cβ outliers (%)	0.00
Peptide plane (%)	
Cis proline/general	0.0/0.0
Twisted proline/general	0.0/0.0
CaBLAM outliers (%)	0.00
ADP (B-factors)	
so/Aniso (#)	3316/0
min/max/mean	
Protein	105.72/687.41/260.58
Nucleotide	---
Ligand	---
Water	---
Occupancy	
Mean	1
occ = 1 (%)	100.00
0 < occ < 1 (%)	0.00
Occ > 1 (%)	0.00

Table 2.2| Additional structural model data. The analysis was performed using Phenix 0.9.

Box		
Lengths (Å)	40.38, 38.73, 295.82	
Angles (°)	90.00, 90.00, 90.00	
Supplied Resolution (Å)	7.0	
Resolution Estimates (Å)	Masked	Unmasked
d FSC (half maps; 0.143)	---	---
d 99 (full/half1/half2)	5.1/---/---	5.0/---/---
d model	7.8	7.8
d FSC model (0/0.143/0.5)	6.0/6.8/4.2	6.0/6.8/3.1
Map min/max/mean	-0.14/0.25/0.02	

Table 2.3| Model vs data. The analysis was performed using Phenix 0.9.

CC (mask)	0.72
CC (box)	0.73
CC (peaks)	0.39
C (volume)	0.69
Mean CC for ligands	---

Our structural analysis of SSNA-1 self-assembly support the head-to-tail interaction model proposed for *C. reinhardtii* homologue of SSNA1 [97], where N- and C-termini interact to drive the formation of fibrillar oligomers. Specifically, we revealed a molecular characterization of the register of the coiled-coil and provided a molecular basis of why both N-terminal and C-terminal residues are dispensable for the coiled-coil formation.

Additionally, the electro-surface potential analysis of the 3E mutant fragments further revealed the presence of negatively charged patches, primarily attributed to the specific 3E mutations (R18E/R20E/Q98E) and the neighboring charged residues within the three-stranded junctions (Figure 3.5). While R18E and R20E mutations were oriented towards the inner lumen, Q98E was located at the interfibrillar interfaces. These negative charges likely acted as a repulsive factor to separate the bundles into the 8-stranded filaments, enabling our structural analysis.

5.3 SSNA-1 head-to-tail self-assembly requires both N- and C-termini

To elucidate the critical regions involved in the self-assembly process and validate our hybrid structural model, we characterized the full-length as well as various constructs of SSNA-1 to disrupt its fibril formation. The assembly of these variants were assessed using several

techniques including dynamic light scattering (DLS), negative staining EM, and CD (Figure 3.7, 3.8, and 3.9) (Table 2.4). In the case of full-length SSNA-1 (FL or 1-105), DLS analysis revealed a decay of the autocorrelation function at 5324 µs, indicating the presence of a mixed population of small oligomers and filaments with heterogeneous bundles (Figure 3.7) (Table 2.4).

Furthermore, we tested truncated protein variants to identify crucial residues involved in self-assembly. Our findings revealed that SSNA-1 (18-105) retained the ability to form filaments though they were not bundled and less prominent than the full-length (Figure 3.7). In opposite, SSNA-1 (19-105), lacking R18, no longer exhibited filament assembly, nor fibril assembly, as measured by DLS as well as negative-stain EM.

Similarly, we investigated the impact of C-terminal truncations on the self-assembly process. We created truncation fragments, namely SSNA-1 (1-96), SSNA-1 (1-97), and SSNA-1 (1-100). While SSNA-1 (1-100) and (1-97) demonstrated filament formation without bundles, no filaments nor fibrils were observed with SSNA-1 (1-96).

Finally, we created individual constructs with point mutations on residues that appeared to be located in the region key for self-assembly, namely SSNA-1 (R18E/Y97E), (Y15E/Y97E), (Y97E), (Y15E), and (R18E), and tested them to assess their influence on the oligomerization process. Interestingly, the mutations R18E/Y97E, Y15E/Y97E, and Y97E, weakened fibril formation such that observed for the full-length. In contrast, R18E and Y15E did not have the same effect, as they formed filamentous bundles (Figure 3.9).

These results validate our hybrid structural model and led us to conclude that Y97-based interactions are critical for fibril formation.

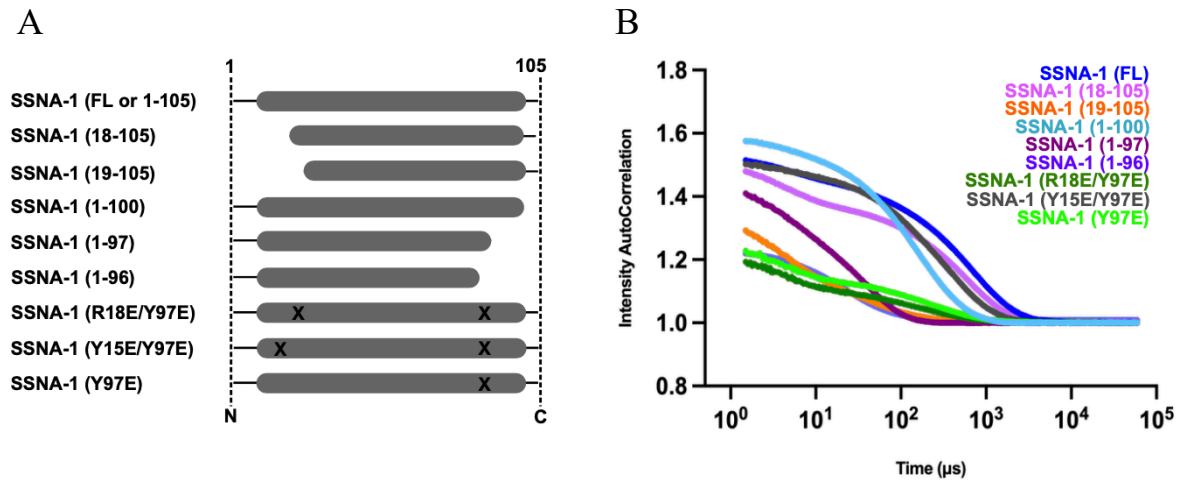

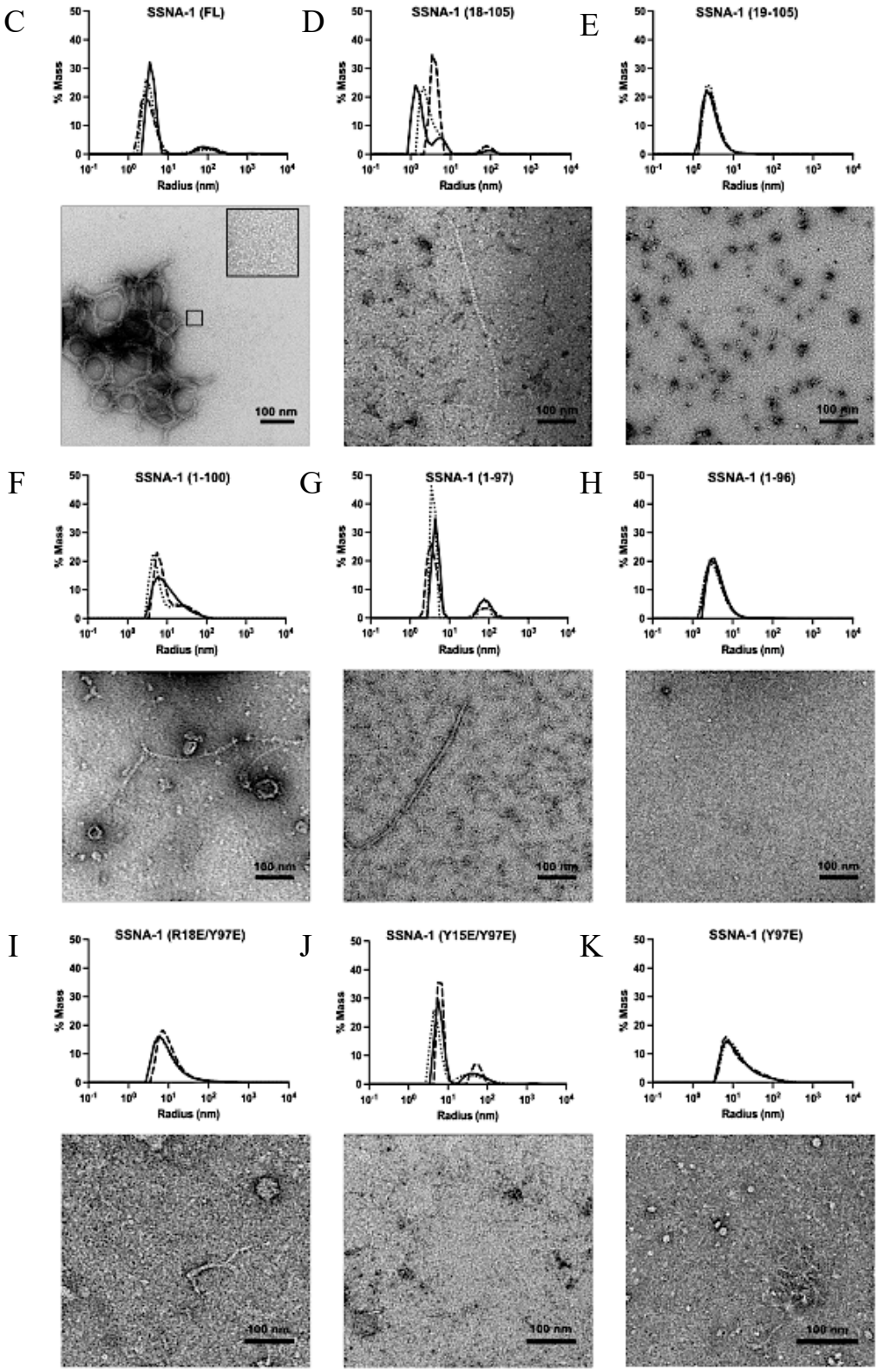

Figure 3.7| Biochemical characterization of SSNA-1. A| Schematic view of SSNA-1 constructs generated to understand functional regions involved in the self-assembly process. **B|** Autocorrelation curves (cumulative fits) of SSNA-1 constructs measured through DLS. **C-K|** Top: hydrodynamic radii distribution of SSNA-1 particles measured from the Autocorrelation curves. Bottom: negative staining EM of SSNA-1 constructs. Scale bars refer to 100 nm.

Table 2.4| Autocorrelation function decay measured by DLS for different protein construct of SSNA-1. The decay threshold is considered at Intensity AutoCorrelation = 1.

Protein construct	Autocorrelation function decay
SSNA-1 (FL)	5342.8 µs
SSNA-1 (18-105)	2969.6 µs
SSNA-1 (19-105)	332.8 µs
SSNA-1 (1-100)	1177.6 µs
SSNA-1 (1-97)	3481.6 µs
SSNA-1 (1-96)	665.6 µs
SSNA-1 (R18E/Y97E)	1228.8 µs
SSNA-1 (Y15E/Y97E)	2355.2 µs
SSNA-1 (Y97E)	1331.2 µs

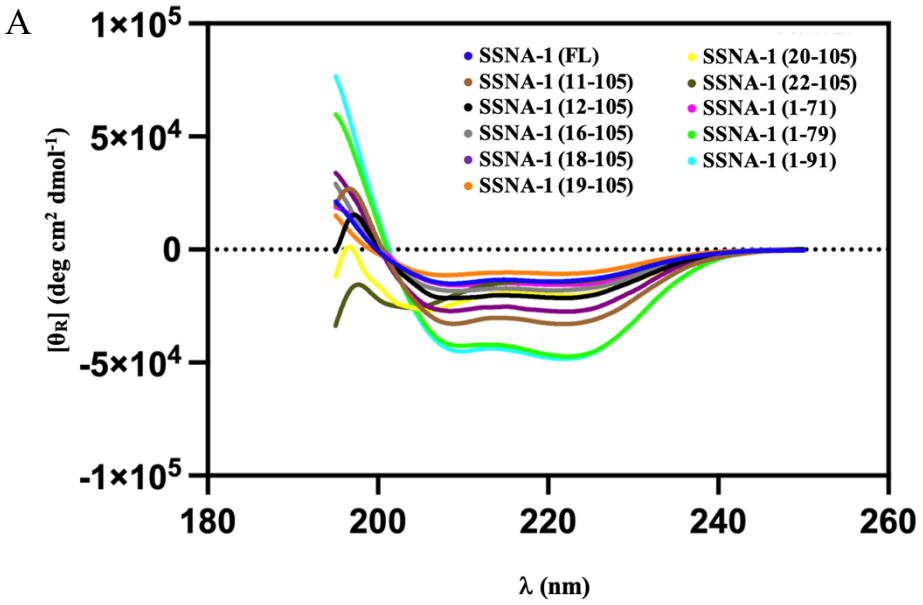

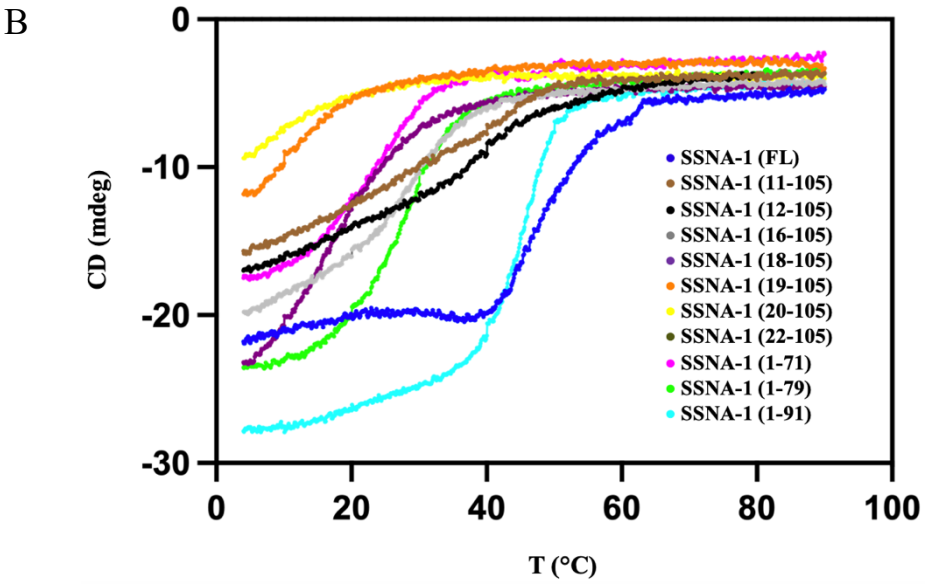

Figure 3.8| CD spectra of recombinantly purified SSNA-1 constructs. A| The graph shows the ellipticity per mole of peptide residues as a function of the wavelength. **B|** The graph represents the circular dichroisms as a function of the temperature.

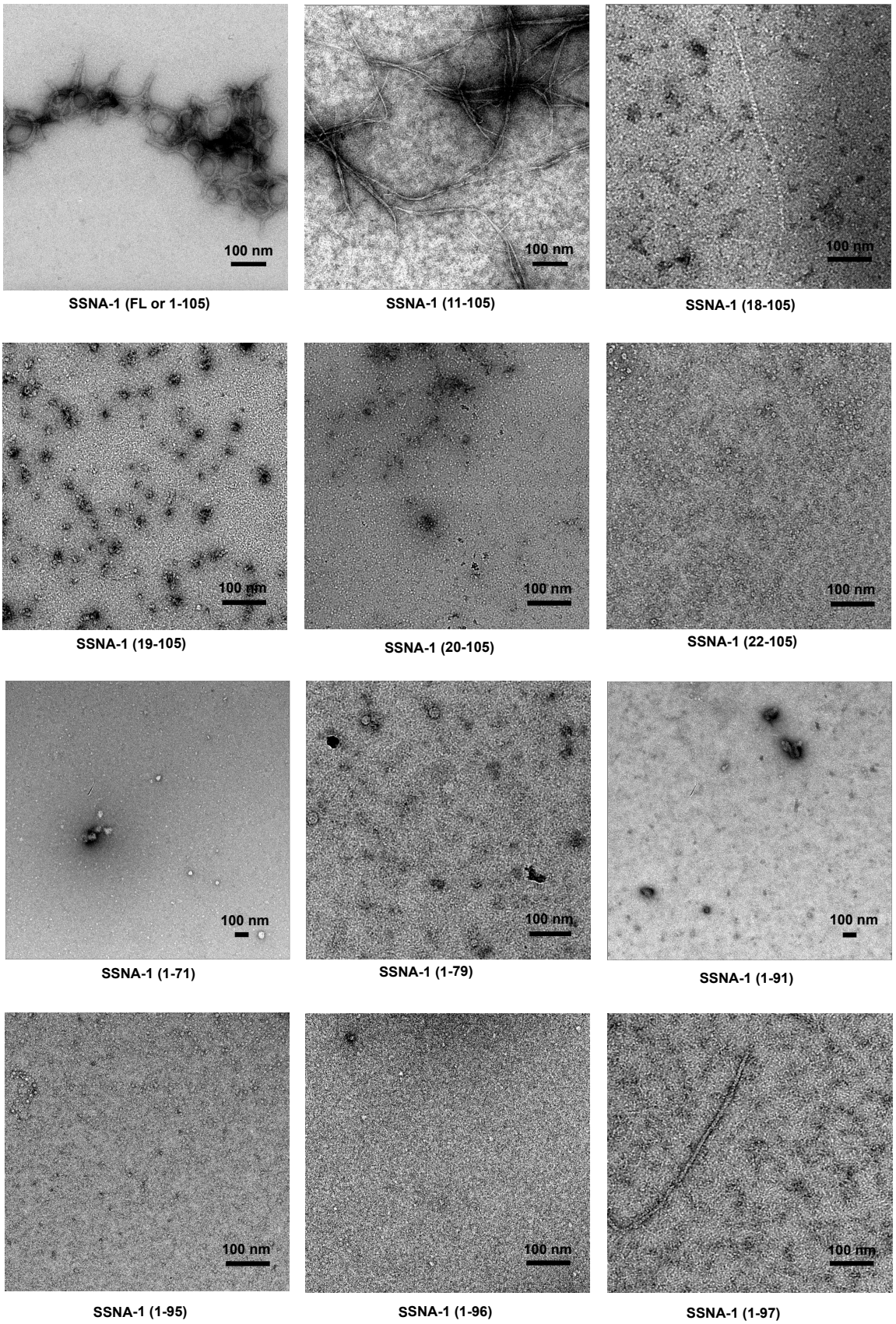

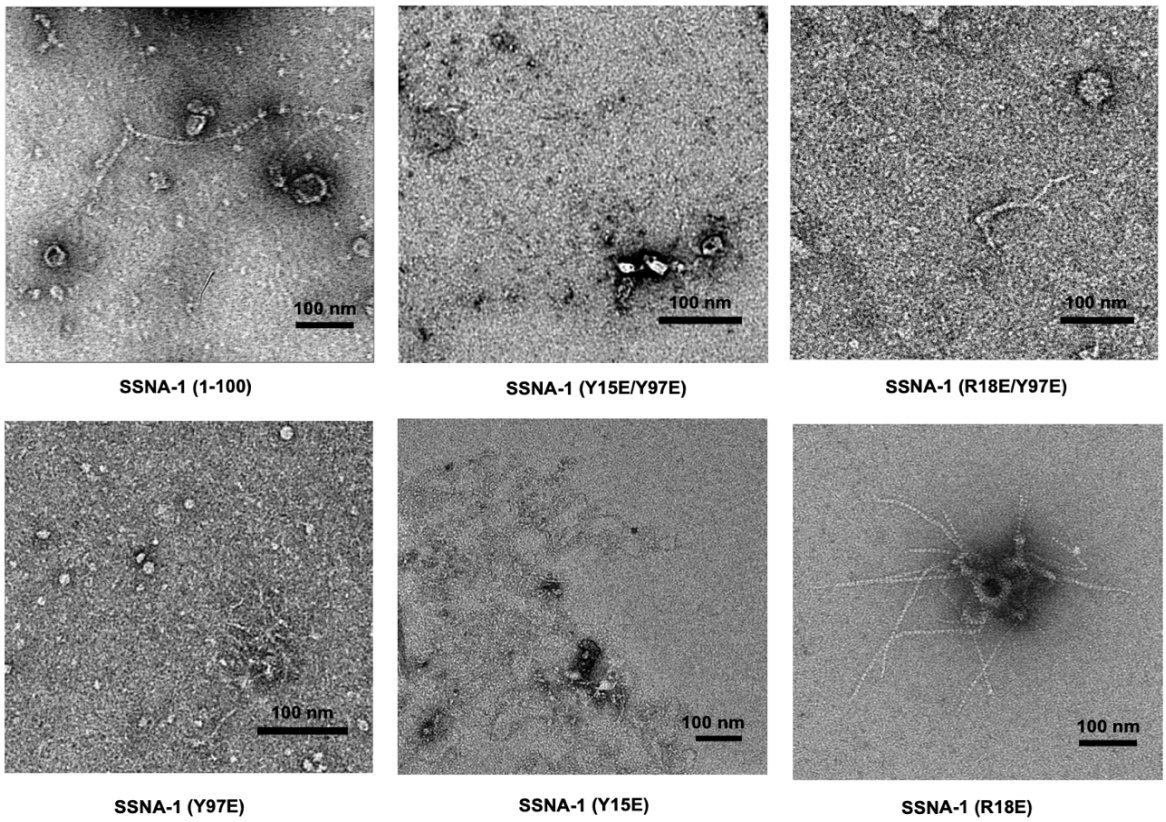

Figure 3.9| Negative staining of SSNA-1 protein constructs. Scale bars refer to 100 nm.

5.4 The localization of SSNA-1 is centriolar but it becomes dynamic after the second cell cycle in *C. elegans* embryos

Collectively, our *in vitro* analysis characterized SSNA-1 molecular mechanism of self-assembly, but its biological significance at the centrosome remains unclear. To test SSNA-1's role we fist evaluated its localization using *C. elegans*. We characterized SSNA-1 localization in *C. elegans* using transgenic worms expressing SSNA-1::spot and GFP fused to the centriolar component SAS-4 (or SAS-4::GFP) (Figure 3.10).

The co-localization of SSNA-1 with SAS-4::GFP, observed by fixed imaging via SPOT tag as well as SPOT 568 conjugated antibody, indicated that from fertilization through the end of the division of the zygote SSNA-1 shows a centriolar localization (Figure 3.10). Following the first division, SSNA-1 remained centriolar but additionally displays a dynamic localization that is initially dispersed throughout the cytoplasm but then congregates around the centriole as the cell progresses through mitosis (Figure 3.10). This localization pattern is reminiscent of centriolar satellites that are present in vertebrate cells but have thus far not been discovered

in *C. elegans*. At the end of mitosis when the PCM is being broken down, these SSNA-1 satellites disperse again and then recongregate around the centriole in the following mitosis.

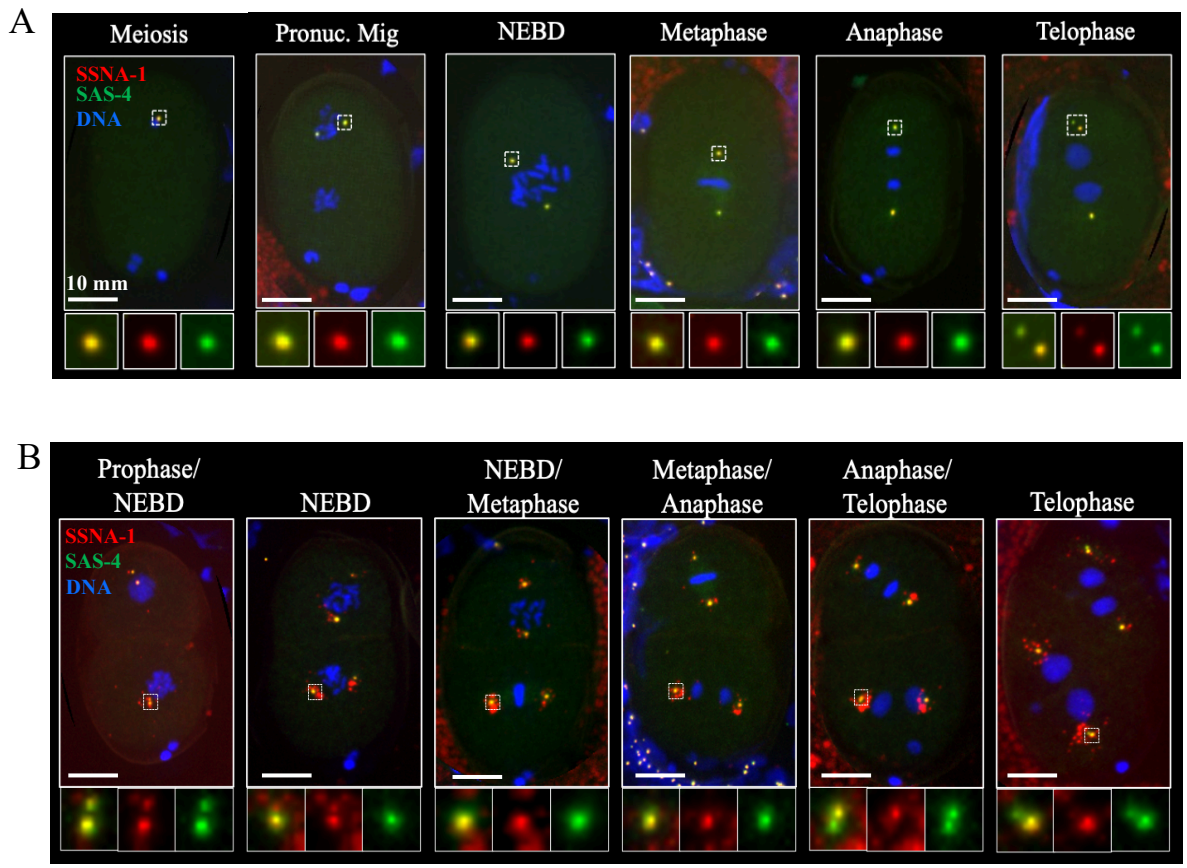

Figure 3.10| Localization of SSNA-1 in C. elegans embryos. A| SSNA-1 is restricted to the centriole from fertilization through the end of the first division. **B|** SSNA-1 localizes to centrioles and satellite-like structures following zygotic division. SSNA-1::spot and SAS-4::GFP were visualized by fixed imaging via C-terminal SPOT tag and a SPOT 568 conjugated nanobody. DNA is colored in blue. Scale bars are 10 mm.

These results agree with previous findings [98,101-104] and led us to conclude that SSNA-1 localization is centriolar, but it becomes dynamic during embryonic development of *C. elegans*, specifically after the second cell cycle.

5.5 SSNA-1 knock-out results in reduced viability and morphological defects in *C. elegans* embryos

To elucidate SSNA-1's role and its centriolar involvement during embryonic development of *C. elegans*, we created different strains of worms which had the knock-out of SSNA-1 as well as various protein mutation and performed viability assays (Fig. 3.11).

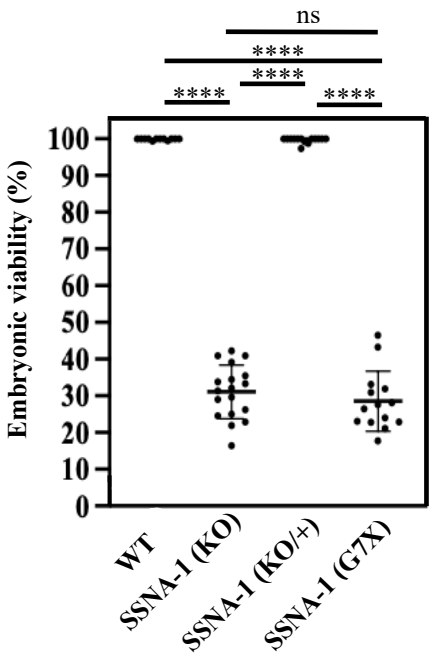

Figure 3.11| The knock-out effect of SSNA-1 *C. elegans* embryos. Viability assay of wild-type (WT), knock-out (KO), and heterozygote strains for SSNA-1 (KO/+), as well as G7X. One-way anova was used to determine significance. The 4 asterisks represent a p-value which is <0.0001.

The embryonic viability of *C. elegans* was significantly decreased when CRISPR-mediated deletion of SSNA-1 was performed, as 31 % of embryos were viable, compared to the viability observed for the wild-type with 99 % (Figure 3.11). This reduction in viability was not showed in heterozygotes SSNA-1 (KO/+) indicating that SSNA-1 is a recessive gene (Figure 3.11). In addition, the viability was measured in strains containing a premature stop codon, as shown with SSNA-1 (G7X). We introduced a stop codon in position G7 to ensure that the procedure of creating knock-out strains didn't compromise any of the other 2 genes present into the 3 genes operon in which SSNA-1 is hosted. Consistently, SSNA-1 (G7X) viability was comparable to the one observed for SSNA-1 (KO) (Figure 3.11).

The 31 % of embryos that were able to hatch from SSNA-1 (KO) strains showed four distinct morphological phenotypes (data not shown), such as wild-type, vulva defects (protruding vulva), egl (egg-laying defective) phenotype, and stunted development with tail abnormalities, that were all maternally rescued.

5.6 SSNA-1 knock-out reveals cell division defects in *C. elegans*, with multipolar spindle being the most prevalent

A closer look of SSNA-1 (KO) strains revealed that most embryos had defects in cell division (Figure 3.12). We observed multipolar spindles in 89 % of embryos as well as minor

phenotypes, such as detached centrosomes and cytokinesis failure, in 15 % and < 10 % of embryos, respectively (Figure 3.12). Following embryonic development until 8-cell stage, the most severe phenotypes were observed at the third division (4-cell stage) through dipolar spindles (70 %), tripoles (28 %), and tetrapoles (2 %). Multipolar formation appeared to occur in specific cell types without any preference (Figure 3.12).

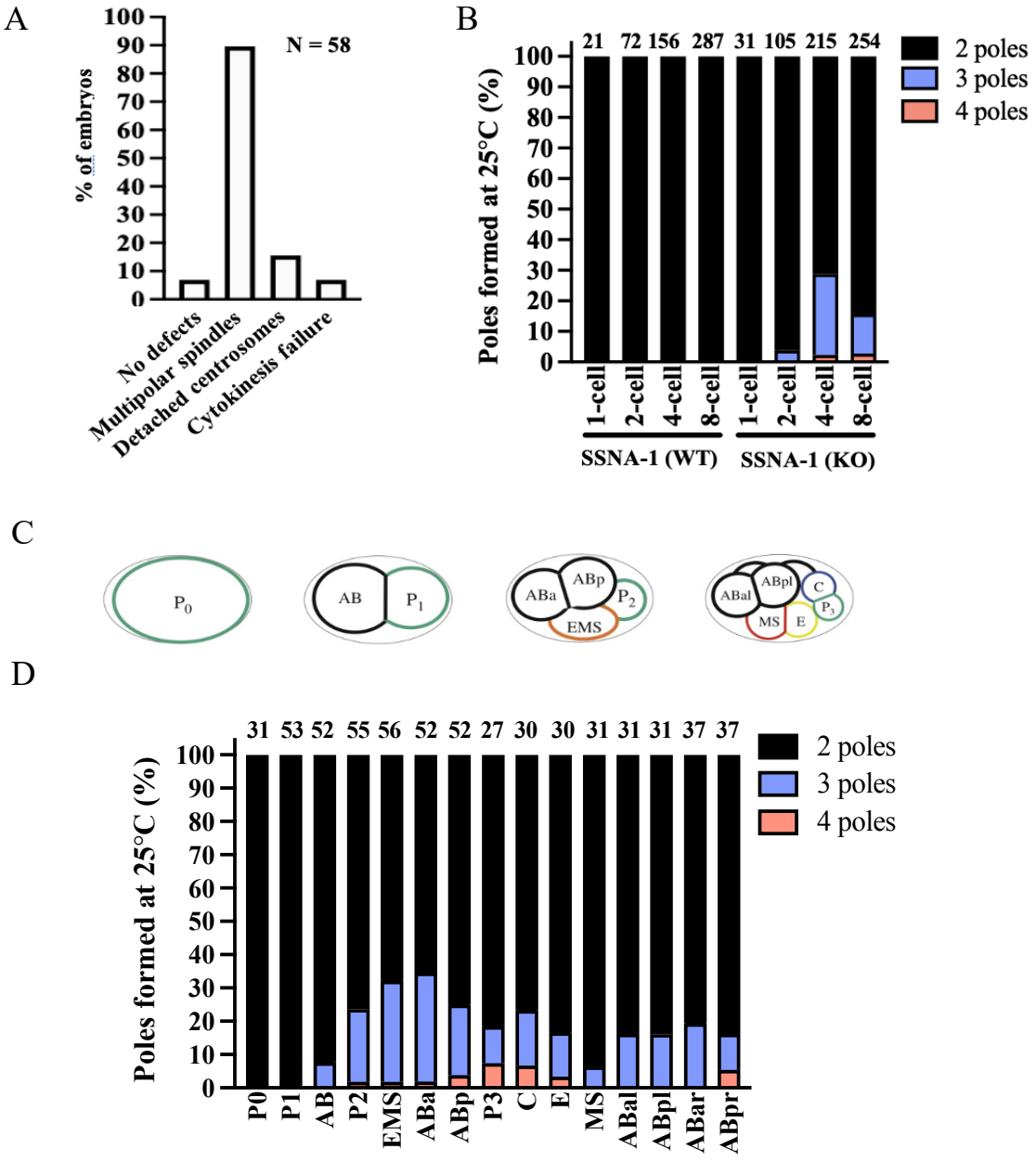

Figure 3.12| The knock-out effect of SSNA-1 in *C. elegans*. A| Live imaging of SSNA-1 (KO) reveals severe cell division defects such as multipolar spindle, detached centrosomes, and cytokinesis failure. 58 embryos were analyzed and the relative defects were quantified. **B|** Quantification of multipolar formation events throughout the first four cell divisions or until the 8-cell stage of embryonic development. Dipoles, tripoles, and tetrapoles were further distinguished. The numbers above each column describe the number of cells that were analyzed. **C|** Schematic view of the cell nomenclature until 8-cell stage of *C. elegans* embryonic development. Image is adopted

from Rose and Gonczy, 2014. **D|** Quantification of multipolar formation events in specific cell types until 8-cell stage during embryonic development. The numbers above each column describe the number of cells that were analyzed. The letters below each column represent the differentiated cell type that was analyzed during embryonic development in *C. elegans* (according to the scheme in C).

5.6.1 Extra poles contain SPD-2, ZYG-1, and SAS-4

In light of the findings described in the previous paragraphs, we found that SSNA-1 regulates the nematode viability most likely through the proper formation of the mitotic spindle. The mitotic spindle is a dynamic structure which is essential to physically segregate chromosomes and orient the plane of cleavage during cell division. Although these results could explain the low viability observed for SSNA-1 (KO) strains, the details remain still unclear. To assess how SSNA-1 would specifically regulate the proper spindle formation, we performed immunofluorescent assays labeling nematode centriolar proteins.

Our results show that tripolar spindles were positive for most of the core proteins of centriole replication [51-59], such as SPD-2, ZYG-1, and SAS-4 (Figure 3.13). Although the presence of SPD-2 and ZYG-1 may indicate that the extra poles are either fragmented or immature centrosomes, the presence of SAS-4, a protein recruited at final stages of centriole replication [77-86], indicates bona fide that such extra poles are centrosomes. In addition, our immunofluorescence analysis reveals that loss of SSNA-1 alters centriolar composition such that centrioles have less ZYG-1 and more SAS-6, the main central scaffold components. SPD-2 protein levels remain as wild-type strains (Figure 3.14).

These findings led us to conclude that SSNA-1 ensure the formation of the proper mitotic spindle through regulating centriole structural integrity and/or its molecular composition.

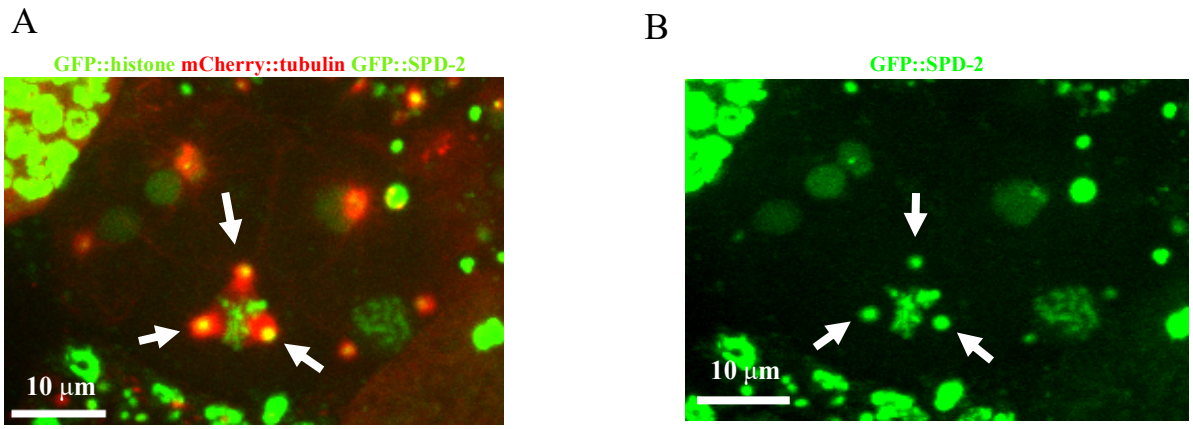

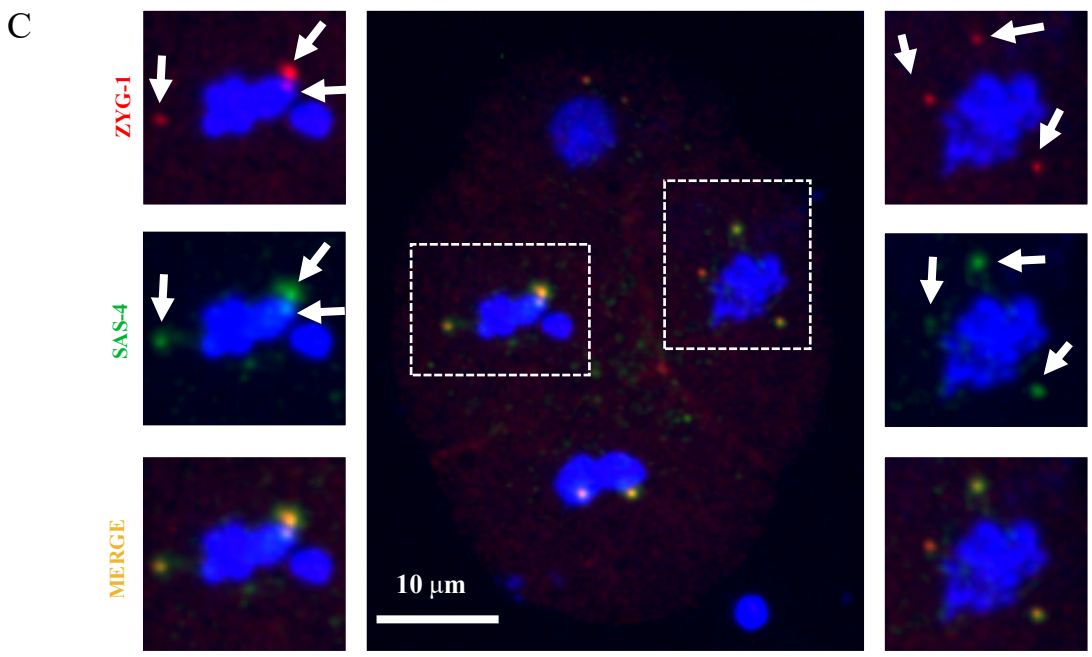

Figure 3.13| Extra poles (tripolar spindles) of SSNA-1 (KO) strains contain the proteins SPD-2, ZYG-1, and SAS-4. A| *C. elegans* embryos were fixed with methanol and imaged via mouse monoclonal anti-alpha-tubulin DM1A and Alexa Fluor anti-mouse as secondary antibodies. The image shows that tripolar spindles (arrows) in SSNA-1 (KO) strain are positive for tubulin. The green signals show the fluorescence of GFP::SPD-2 and GFP::histone indicating that tripolar spindles (arrows) are positive for the protein SPD-2. The tubulin signals co-localize with SPD-2 signals. **A|** The image shows the signal of GFP::SPD-2 only for the specimen observed in figure A. The arrows indicate the localization of SPD-2 at the tripolar spindles. **C|** *C. elegans* embryos were fixed with methanol and imaged for endogenous SAS-4, using rabbit polyclonal anti-SAS-4 and Alexa Fluor anti-rabbit as secondary antibodies. These results suggest that tripolar spindles (arrows) are positive for the protein SAS-4. The same specimen was also analyzed for ZYG-1::spot, which was visualized via SPOT-Label Alexa Fuor. The signal of ZYG-1::spot also appears at the tripolar spindles (arrows). DNA is represented in blues. Scale bars refer to 10 µm.

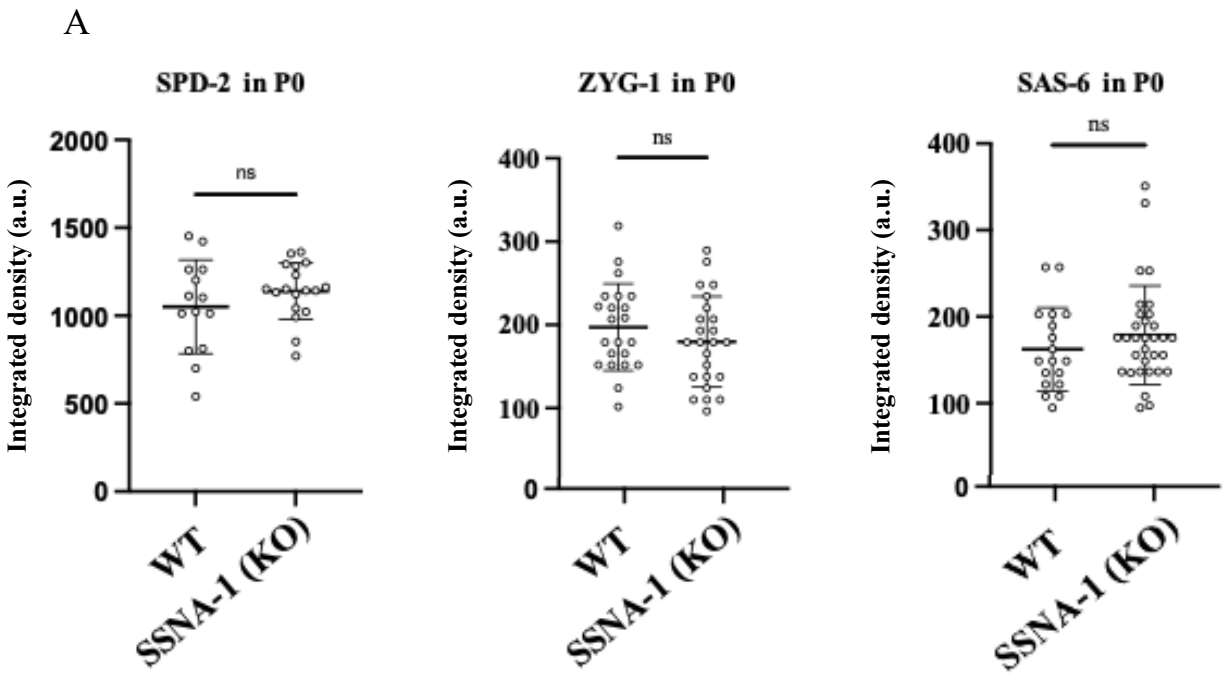

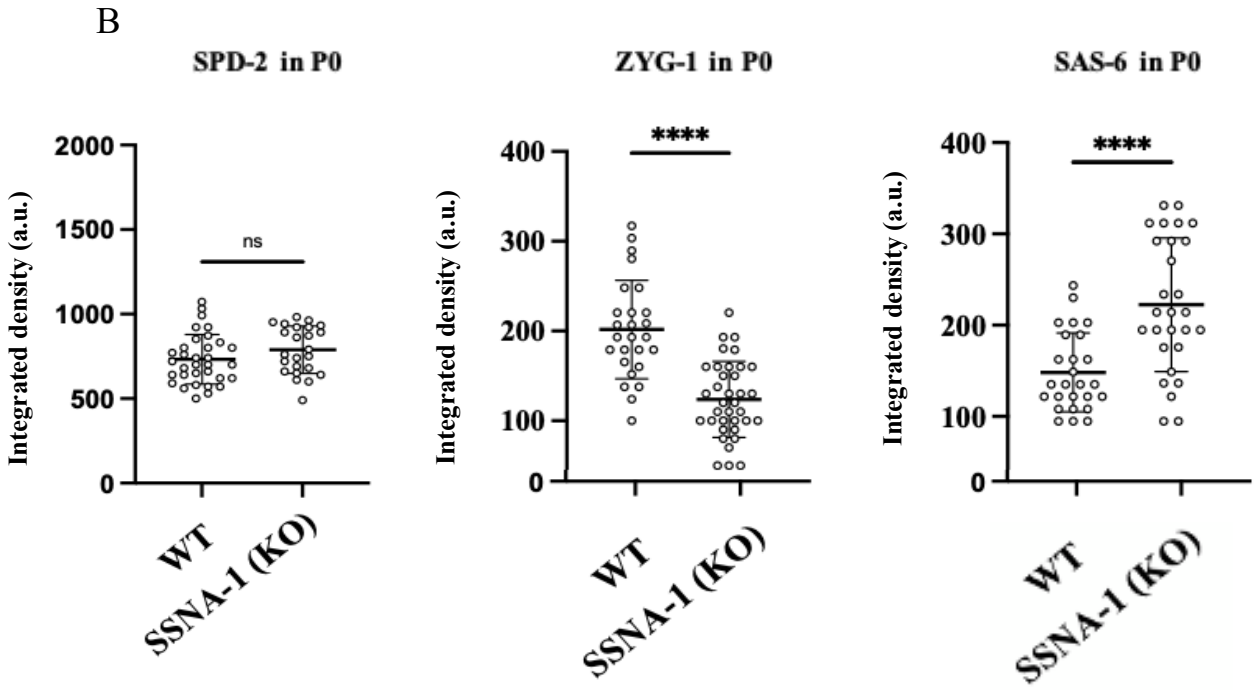

Figure 3.14| Centriolar levels of ZYG-1 and SAS-6 are altered in the SSNA-1 (KO) strain. A, B | Quantification of immunofluorescence signal of GFP::SPD-2, ZYG-1::spot, and SAS-6::spot at anaphase in either WT of SSNA-1 (KO) embryos during the second cell division. The arbitrary unit (a.u.) is calculated from the density of the fluorescent signal through ImageJ. One-way anova was used to determine significance. The 4 asterisks represent a p-value which is <0.0001.

5.7 Mutations interfering with SSNA-1 oligomerization affect *C. elegans* viability

Considering SSNA-1 involvement in centriole formation, we hypothesized that such biological mechanism could be orchestrated by its self-assemble ability. To test such idea, we created worm strains having different SSNA-1 endogenous constructs (Figure 3.15), that were previously characterized *in vitro* in regard of the filament formation (Figure 3.7, 3.8, and 3.9). When endogenous SSNA-1 was truncated for amino acids that impaired the filament bundle formation, the embryonic viability resulted in a significant decrease (Figure 3.15). In particular, strains with SSNA-1 (19-105), a construct that abolished completely the fibril formation *in vitro*, decreased the strain viability to 30 %. Similarly, worms with SSNA-1 (1-99), a truncation that retained fibril formation, and higher order oligomerization into filaments, but impaired the bundling activity of filaments *in vitro*, were as viable as 30 %. Both reductions in viability are comparable to the one observed for SSNA-1 (KO) strains. We also show that SSNA-1 (18-105) induced a stronger decrease in viability than SSNA-1 (KO) worms (~20 %), indicating a toxic effect for the embryos.

A

SSNA-1 fragment	Fibril formation
SSNA-1 (FL or 1-105)	++
SSNA-1 (18-105)	+
SSNA-1 (19-105)	-
SSNA-1 (1-100)	+
SSNA-1 (1-97)	+
SSNA-1 (1-96)	-
	++ Filament (bundles) + Filament (no bundles) - Short oligomers

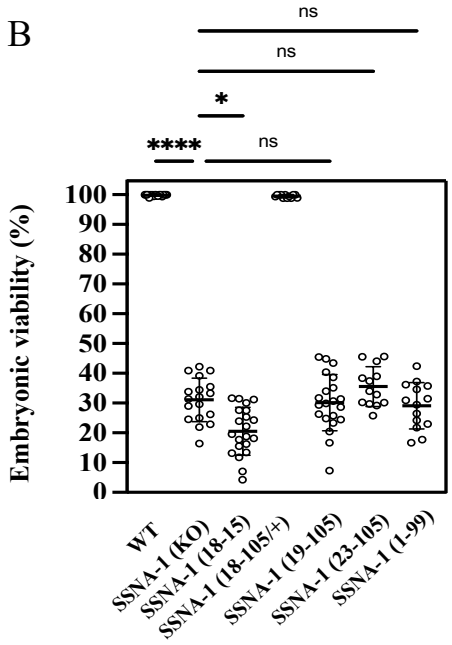

Figure 3.15| Mutations of SSNA-1 that interfere with its high-order oligomerization (fibril-like bundles) affect worms' viability. A| Schematic table of the oligomerization ability of SSNA-1 and relative truncations *in vitro*. Scheme is a summary of the results observed in Figure 3.7, 3.8, and 3.9. **B|** Viability assay for endogenous SSNA-1 and relative truncations in *C. elegans*. One-way anova was used to determine significance. The 4 asterisks represent a p-value which is <0.0001. One asterisk indicates p<0.05.

5.8 Microtubules and ZYG-1 bind SSNA-1 *in vitro*

Previous results revealed that SSNA-1 involvement in centriole formation rely on its self-assembly ability. However, the centriolar architecture comprise many proteins that form a highly regulated network in space and time, ensuring its biological functions throughout specific interactions [59]. To test whether SSNA-1 would have binding partners contributing to

the underlying biological mechanism of centriole regulation, we performed *in vitro* reconstitution experiments with two centriolar proteins, such as MTs and ZYG-1.

The SSNA1 family has been previously characterized as MTBP [97]. To test whether the *C. elegans* orthologue SSNA-1 would conserve such activity, we performed co-sedimentation assays between recombinant SSNA-1 and pre-polymerized MTs (Figure 3.16). When SSNA-1 (FL or 1-105) was reconstituted with MTs, it exhibited binding activity as 69% of SSNA-1 used for the assay co-sedimented with MTs (Figure 3.16 and 3.18). To further identify whether SSNA-1 self-assembly would be involved in MT binding and assess the region responsible for MT recognition, we performed binding assays with the previously characterized truncation versions of SSNA-1. Interestingly, when N-terminal truncation SSNA-1 (18-105) was tested, the binding of MTs was reduced, compared to the full-length SSNA-1, to 29% (Figure 3.16 and 3.18). Furthermore, MT binding was consistently decreases to 12% when an additional N-terminal residue was truncated, such as SSNA-1 (19-105) (Figure 3.16 and 3.18).

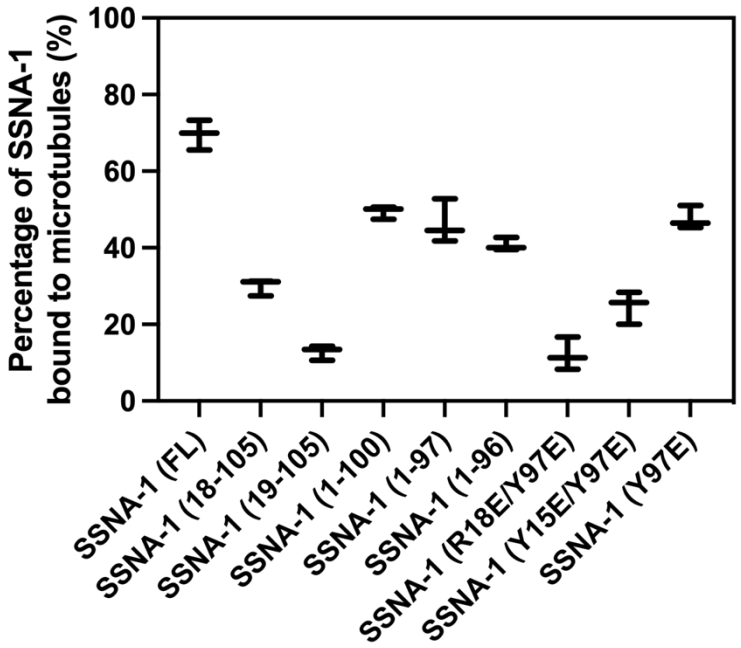

Figure 3.16| SSNA-1 interacts with microtubules (MTs) *in vitro*. Violin plot representing the quantification of the co-sedimentation assay of pre-polymerized MTs and different SSNA-1 protein constructs. The mean value corresponds to the horizontal line inside the violin. These results indicate that the formation of fibrils is not essential for the binding of SSNA-1 to microtubules. Additionally, the SSNA-1 N-terminus fragment until R18, independent of its role in fibril assembly, is a critical region for microtubule binding.

To investigate whether the ability of SSNA-1 to bind MTs is completely dependent on its fibrillar formation, we also tested the microtubule binding of C-terminal truncated SSNA-1

fragments. SSNA-1 (1-96), which do not form fibrils, still exhibited binding to MTs (Figure 3.16 and 3.18). The percentage of SSNA-1 (1-96) that co-sedimented with MTs was 40 %, which is comparable to the percentages observed for the self-assembly competent constructs, such as SSNA-1 (1-97), which showed 46 %, SSNA-1 (1-100), with 49 %, and the full-length, with 69% (Figure 3.16 and 3.18).

Furthermore, as MT binding did not rely on SSNA-1 self-assembly, to assess whether MT binding ability would exclusively depend on SSNA-1 N-terminus, we used constructs that weakened fibril formation (using the mutation Y97E) with additional point mutations at the N-terminus, such SSNA-1 (R18E/Y97E), (Y15E/Y97E), and (Y97E). Interestingly, we observed that SSNA-1 (Y15E/Y97E) and (R18E/Y97E) reduced its co-sedimentation with MTs to 24 and 12 %, respectively, compared to the construct SSNA-1 (Y97E), which showed 47 % of co-sedimentation, a similar result previously observed for the full-length (Figure 3.16 and 3.18).
These results indicate that the formation of fibrils is not essential for the binding of SSNA-1 to microtubules. We showed that N-terminus fragment until R18, independent of its role in fibril assembly, is a critical region for MT binding, with the upstream N-terminus residues likely playing regulatory roles in the MT recognition. The N-terminus fragment until R18 of SSNA-1 is also crucial for structural stability (Figure 3.8).
These findings also reveal the possibility that, in *C. elegans*, SSNA-1 could bind MT during its involvement in regulating proper centriole formation.

Taking into consideration our previous results, where the knock-out of SSNA-1 decreased ZYG-1 recruitment at centrioles in *C. elegans* embryos (Figure 3.17 and 3.19), we also tested whether SSNA-1 could bind the Polo-like kinase ZYG-1. Our results show that SSNA-1 could co-sediment with recombinant ZYG-1 *in vitro*. We found that 84.6 % of ZYG-1 co-sedimented with SSNA-1 filaments, compared to the control percentage of 3.9 % (in absence of SSNA-1). The interaction of SSNA-1 and ZYG-1 was previously undocumented (to the best of our knowledge) and further provide evidence that SSNA-1 might be directly involved in ensuring the proper centriolar architecture through ZYG-1 binding and/or recruitment. In contrast, the control experiment shows that ZYG-1 could not co-sediment with pre-polymerized MTs. Finally, to further validate the specific binding between ZYG-1 and SSNA-1 filaments, we show that BSA could not co-sediment with SSNA-1 filaments.

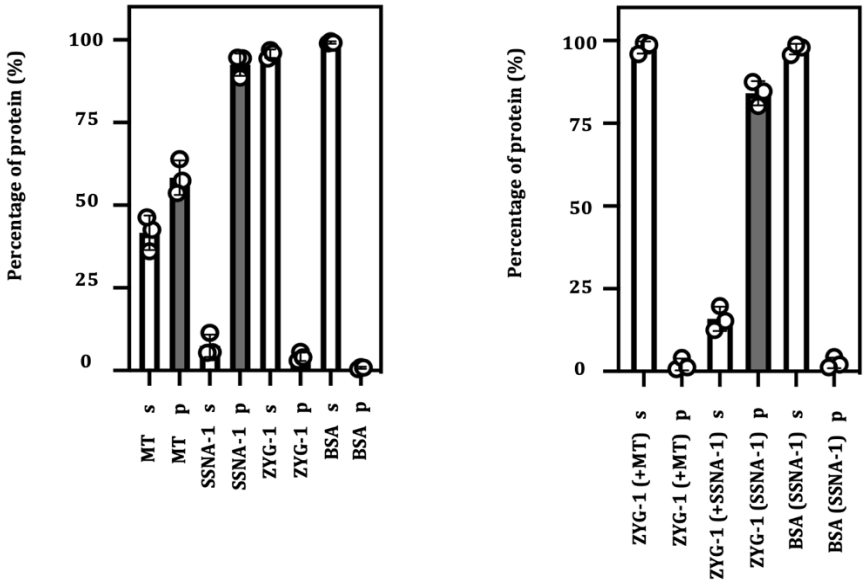

Figure 3.17| SSNA-1 interacts with ZYG-1 *in vitro*. A | Left graph: sedimentation assay of pre-polymerized MTs, pre-polymerized SSNA-1 filaments, soluble ZYG-1, and BSA. Right graph: sedimentation assay of ZYG-1 in presence of MTs, ZYG-1 in presence of SSNA-1 filaments, and BSA in presence of SSNA-1 filaments. The letter "s" represents supernatant and the letter "p" represents pellet. This sedimentation assay shows that ZYG-1 could co-sediment with SSNA-1 filaments, compared to the control where ZYG-1 could not co-sediment with pre-polymerized MTs. To further validate the specific binding between ZYG-1 and SSNA-1 filaments, we show that BSA could not co-sediment with SSNA-1 filaments.

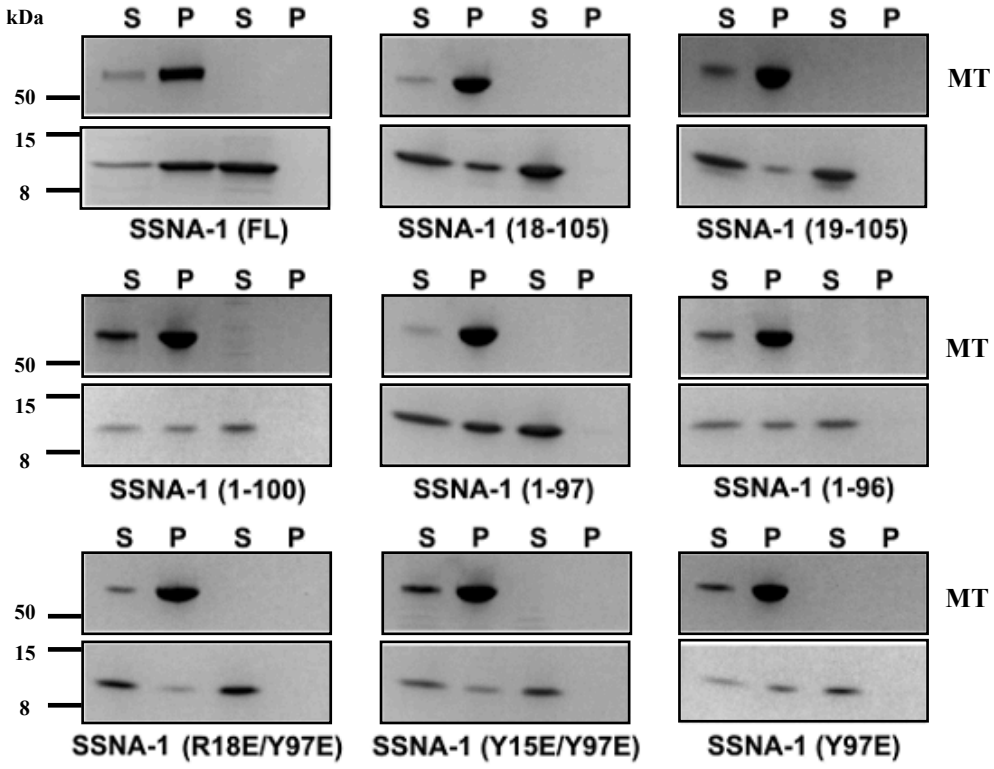

Figure 3.18| Sedimentation assay of several protein constructs of soluble SSNA-1 and pre-polymerized MTs. The letter "s" represents supernatant and the letter "p" represents pellet. Each experiment was performed three times.

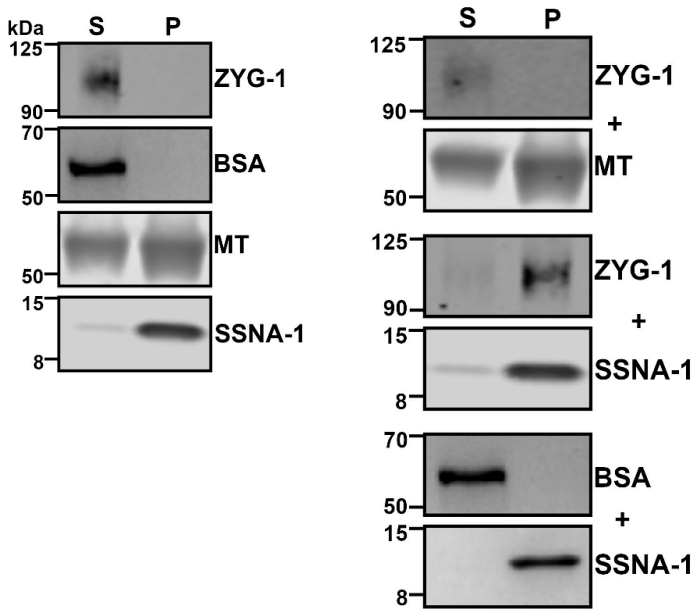

Figure 3.19| Sedimentation assay of SSNA-1 (FL) filaments and ZYG-1, ZYG-1 and pre-polymerized MTs, as well as SSNA-1 and BSA. The letter "s" represents supernatant and the letter "p" represents pellet. Each experiment was performed three times.

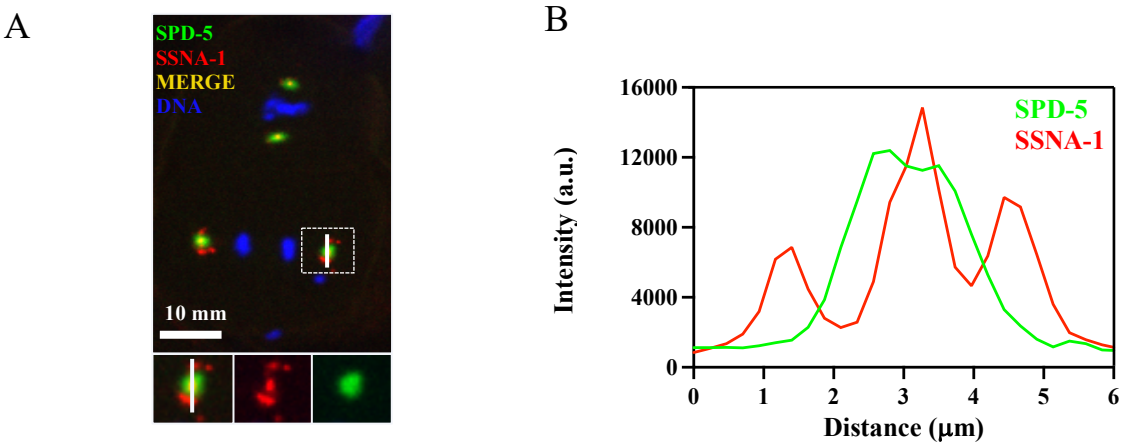

Figure 3.20| SSNA-1 satellite-like structures. A| Localization of SSNA-1::spot (through SPOT 568) in relation of GFP::SPD-5 signal in *C. elegans* embryo. The box represents a centrosomal area delimited by the PCM protein SPD-5. The SPD-5 signal further extends outside the centriolar localization of SSNA-1. The line across the box is an arbitrary plane chosen for the analysis performed in B. Scale bar refers to 10 mm. The DNA signal is represented in blue. **B|** Line plot profile of across the centrosome, indicating that satellite-like structures reside outside SPD-5. The arbitrary unit (a.u.) is calculated from the density of the fluorescent signal through ImageJ.

5.9 SSNA-1 novel satellite-like structures reside at about 750 nm from the center of centrioles

We have shown that SSNA-1 localizes to centriole and contribute for its formation. However,

following the zygotic division, SSNA-1 also shows additional satellite-like structures in embryos that have progressed to the second cell cycle (Figure 3.20). The localization pattern is reminiscent of centriolar satellites, but these structures have not been reported in *C. elegans* so far. Specifically, at the end of mitosis, when the PCM is dynamically rearranged, we found that SSNA-1 spreads out of centriole and quickly recongregate around the centriole in satellite-like structure as the following mitosis occur.

To characterize such satellite-like structures we performed immunofluorescence analysis (Figure 3.20). Our results revealed that SSNA-1 satellite-like structures localized nearby SPD-5 signal at about 750 nm from the center of centrioles (Figure 3.20 and 1.9). In this location, towards the outer PCM, there are proteins such as GIP-1 and AIR-1. Interestingly, AIR-1 is a PCM protein that along with γ-TURC is required to build MTs at the centrosome. The protein AIR-1 is activated by the TPXL-1/TPX2 complex which is a MT stabilizing and nucleation promoting factor [132,133].

Table 2.5| SSNA-1 directed activity of MTs branching *in vitro*. Table representing the quantification of the MT branching assay (co-polymerization between tubulin and different SSNA-1 constructs) and its correlation with SSNA-1 fibril formation activity observed previously *in vitro*. The "++" of "Fibril formation" section refers to SSNA-1 filament formation with bundles. The "+" of "Fibril formation" section indicates to SSNA-1 filament formation with no bundles. The "+/-" of "Fibril formation" section highlight SSNA-1 fibril formation without high-order oligomerization into filaments. The "-" of "Fibril formation" section refers to SSNA-1 fibril formation not observed. The "+" of "Microtubule branching" section indicates to the observation of such activity. The "-" of "Microtubule branching" section highlight activity not observed.

	Fibril formation	**Microtubule branching**
SSNA-1 (FL or 1-105)	++	+
SSNA-1 (18-105)	+	+
SSNA-1 (19-105)	-	-
SSNA-1 (1-100)	+	+
SSNA-1 (1-97)	+	+
SSNA-1 (1-96)	-	-
SSNA-1 (Y15E/Y97E)	+/-	+
SSNA-1 (R18E/Y97E)	+/-	-
SSNA-1 (Y97E)	+/-	+

5.10 SSNA-1 is a microtubule remodeling factor *in vitro*

The SSNA-1 satellite-like structures location is rich in proteins that promote MT nucleation and/or stabilization. As SSNA1 has been previously characterized as MT nucleator and

remodeling factor [97], we hypothesize that also the *C. elegans* homolog would retain such activity, and explain a potential implication of those SSNA-1 satellites-like structures.

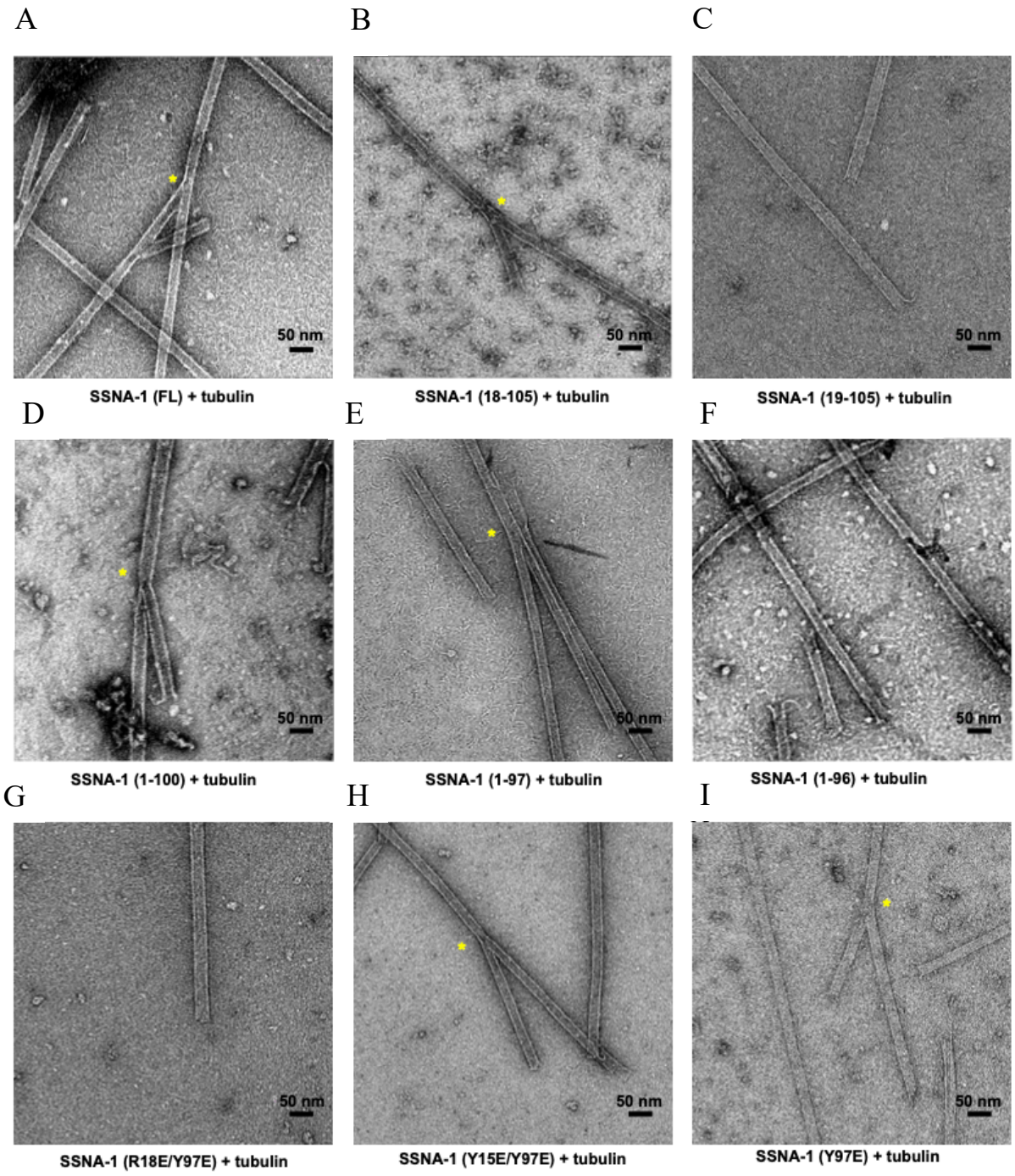

Figure 3.21| Microtubule formation and branching activity mediated by SSNA-1. A-I| Negative staining of different constructs of SSNA-1 co-polymerized with tubulin at room temperature. The yellow asterisk shows branching activity. Scale bars refer to 50 nm.

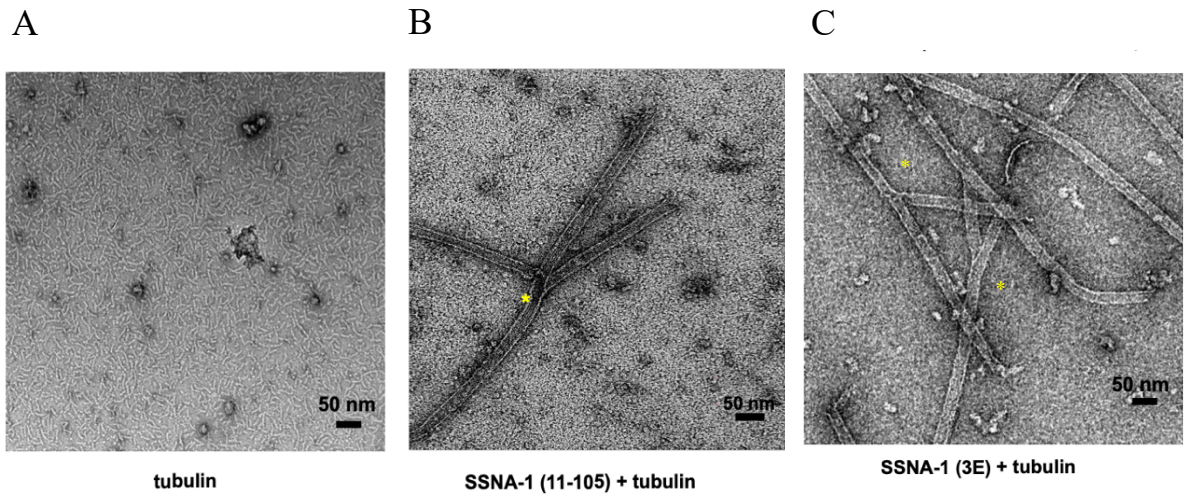

Figure 3.22| Additional data of MT formation and branching activity mediated by SSNA-1. A| Negative staining of tubulin at room temperature (control). **B|** Negative staining of SSNA-1 (11-105) co-polymerized with tubulin at room temperature. **C|** Negative staining of SSNA-1 (3E) co-polymerized with tubulin at room temperature. The yellow asterisk shows branching activity. Scale bars refer to 50 nm.

To test this idea, we observed the co-polymerization of SSNA-1 and tubulin through negative staining EM. We found that SSNA-1 (FL) led to MT formation and branching (Table 2.5) (Fig. 3.21), compared to the control where tubulin without SSNA-1 (FL) could not form MTs (Fig. 3.22), validating the conserved ability of the *C. elegans* homolog to branch MTs. When N-terminal truncations SSNA-1 (11-C) and SSNA-1 (18-C) were tested, which are constructs that could form fibrils (Table 2.5) (Figure 3.7, 3.8 and 3.9), MT branching was still observed (Table 2.5) (Figure 3.21 and 3.22), indicating that these truncations retained the ability to induce MT formation and branching.

Similarly, C-terminal truncations, such SSNA-1 (1-100) and (1-97), which retained the ability to form fibrils, also showed MT formation and branching. However, the truncations that abolished fibril formation, such as SSNA-1 (19-105) and (1-96), no longer exhibited MT branching. To test whether MT branching would rely completely on its self-assembly, constructs that significantly weakened fibril formation, such SSNA-1 (R18E/Y97E), (Y15/Y97), and (Y97) were tested. Interestingly, while the point mutation R18E/Y97E abolished MT branching, the constructs SSNA-1 (Y15E/Y97) and (Y97E) had residual activity. These results are consistent with our co-sedimentation assay, as the construct SSNA-1 (R18E/Y97E) was significantly impaired in binding MTs. Accordingly with our previous

observations [97], we found that SSNA-1 forms MTs and the branching activity don't rely exclusively on SSNA-1 self-assembly, but it is significantly influenced by its N-terminus.

Although we are not aware of any MT branching activity occurring at the centrosome in *C. elegans*, our findings reveal that SSNA-1 satellite-like structures may be promoting MT nucleation and/or potential regulatory activity.

5.11 SSNA-1 satellite-like phenotype appears to be microtubule dependent

To understand whether SSNA-1 satellite-like structures would be involved and/or regulated by MTs, we created nematode strains with an endogenous construct of SSNA-1 containing the point mutation R18A/R20A/E21A/22A, also called 4A (Figure 3.23).

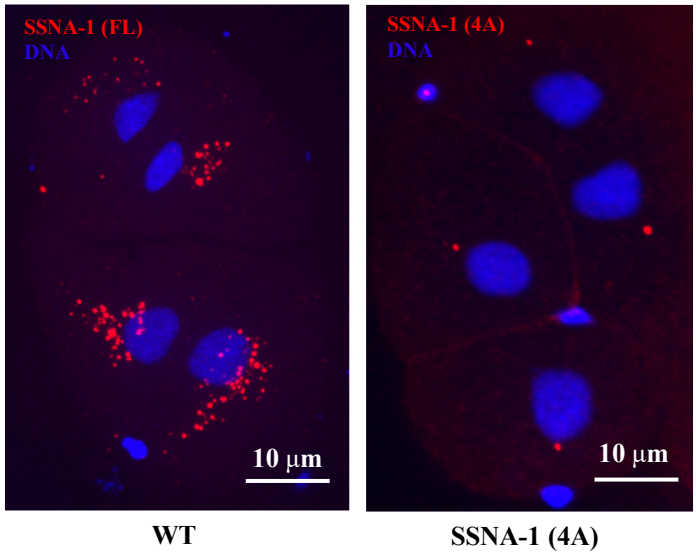

Figure 3.23| The microtubule binding activity of SSNA-1 is required to form SSNA-1 satellite-like structures. | Left panel: localization of SSNA-1::spot in *C. elegans* embryo. Right panel: localization of SSNA-1(4A)::spot in *C. elegans* embryo. The DNA signal is represented in blue. Scale bars refer to 10 µm.

These point mutations were at the N-terminus of SSNA-1, a region that we previously showed to be critical for MT recognition *in vitro*. In addition to R18, a key residue for MT binding, we mutated R20, E21, and E22, as previous findings revealed that the *C. reinhardtii* ortholog of SSNA-1 would bind MT through electrostatic interactions [97]. Interestingly, our imaging revealed that such point mutations successfully abolished the formation of SSNA-1 satellite-

like structures (Figure 3.23), compared to the wild-type. The strains SSNA-1 (4A), however, didn't show decrease in viability, compared to the wild type (data not shown).

These results lead us to conclude that SSNA-1's N-terminus would regulate the formation of SSNA-1 satellites-like structures and that this localization is MT dependent.

6 Discussion

The centrosome is the major MTOC of animal cells and thus has key roles in regulating cell shape, polarity, and motility, as well as spindle formation, chromosome segregation, and cytokinesis. At the core of the centrosome there is an orthogonally oriented pair of microtubule-based, barrel-shaped structures, known as centrioles, which are surrounded by layers of proteins known as the pericentriolar material (PCM). Both centriole and PCM contain proteins important for microtubule nucleation, regulation of the cell cycle and its checkpoints. Following entry into S-phase, centrioles duplicate exactly once per cell cycle to form two centrosomes, which functions in the formation of the mitotic spindle. Following exit from mitosis, cells can re-enter the cell cycle leading to another round of centriole duplication, or the mother centriole can transform into a basal body and template the formation of cilia. Alterations in centriole biogenesis and/or the number of daughter centrioles produced are contributing factors in cancer, neurodevelopmental disorders, and ciliopathies. Previous research has provided an increased understanding of the molecular mechanisms that control such processes. However, we lack comprehensive insights of how these pathways are specifically regulated and how they function in various organisms [47].

During my PhD research, I investigated the molecular and, through a collaboration effort, the genetic analysis of the *C. elegans* protein SSNA-1, whose orthologs have been characterized as microtubule remodeling factors and shown to localize to centrosomes and basal bodies. In this study, SSNA-1's structure is solved in unprecedented detail and the molecular characterization of its behavior, functional domains, as well as interacting partners *in vitro,* has led the discovery of SSNA-1's direct involvement in regulating centriole formation in *C. elegans*.

Our *in vitro* analysis of SSNA-1 revealed a filamentous architecture in which every fibril is composed of antiparallel coiled-coils. The connection between individual coiled-coil dimer units is made with an unusual triple-stranded coiled-coil that acted as a polymerizing junction point. The centrosome is rich in coiled-coil proteins and one of most conversed function is their ability to oligomerize and form the underlying scaffold onto which all other centrosomal proteins are loaded. The formation of these scaffolds during mitotic entry requires proteins such as SPD-2/Cep192, polo-like kinases Plk4/ZYG-1, SPD-5 and Aurora kinase A [132-134]. Interestingly, the observations of SSNA-1 high-order oligomers *in vitro* resembled the process

of scaffold formation. Although such filaments were visualized at non-physiological conditions, the self-assembly ability has led to the interesting hypothesis that SSNA-1, like other centrosomal proteins, could build a scaffold-like structure within the centrosome thereby regulating the recruitment of downstream factors to drive centriole biogenesis.

In *C. elegans*, our results show that from fertilization through the end of the first cell cycle, SSNA-1 localization is restricted to centrioles. However, during subsequent divisions while it remains centriolar, SSNA-1 also localizes to novel satellite-like structures that surround the PCM. These satellites are reminiscent of centriolar satellites that are found in vertebrate cells, but they, as well as their hallmark scaffolding protein, PCM1, have thus far not been discovered in *C. elegans* [135-137]. The deletion of the SSNA-1 coding sequence led to a significant reduction in embryonic viability with the observation of cell division defects, including multipolar spindles, detached centrosomes, and cytokinesis failure. As expected, introducing N- or C-terminal truncations, that were shown to interfere with SSNA-1 self-assembly via coiled-coil interactions *in vitro*, showed an embryonic viability which were comparable to SSNA-1 (KO) strains, indicating a necessity for SSNA-1 oligomerization for its function in *C. elegans*.

Previous studies have characterized other SSNA-1 orthologs as microtubule binding proteins. Accordingly, our results demonstrate that the N-terminus of *C. elegans* SSNA-1 is required for both microtubule binding and remodeling *in vitro*. Microtubule binding was retained independently of the self-assembly ability of SSNA-1. Furthermore, our mutation analysis revealed four key residues within SSNA-1's N-terminus that would regulate the formation of SSNA-1's satellites-like structures, indicating, similar to centriolar satellites, that this localization is likely microtubule dependent. As such strain was fully viable, the low viability observed for SSNA-1 (KO) is relegated to SSNA-1 centriolar localization and indicates that these satellites might be involved in other roles.

Live imaging analysis of SSNA-1 (KO) embryos through the first four rounds of division (until 8-cell stage) revealed cell division defects, with multipolar spindle formation being the most prevalent phenotype observed. The multipolar spindles, which predominately occurred as tripoles, became evident at the beginning of the third round of mitotic division (4-cell stage), indicative of a maternal effect. Such extra poles contained proteins that are among the core components of centriole assembly, including ZYG-1 (the *C. elegans* ortholog of the mammalian Plk4 that acts as the master regulatory kinase controlling centriole assembly), SPD-

2 (the centriolar receptor for ZYG-1), SAS-5 and SAS-6 (the main cartwheel proteins), as well as SAS-4 (that mediates formation of the microtubules-containing centriolar outer wall). Given that SAS-4 is stably incorporated into centrioles in the final stage of centriole assembly, this result indicates that the extra poles observed are bona fide centrosomes that are potentially arising from an overduplication defect or fragmentation. It has been shown that increasing the expression of core centriolar proteins can induce additional daughter centriole formation [138-143]. Under this consideration, we find that SAS-6 centriolar levels, but not total protein, are significantly elevated during centriole duplication initiation at the end of the second mitotic division at the 2-cell stage. As multipolar spindles observed at the 4-cell stage indicates that centriole overduplication would occur at the end of zygote's first mitotic division, and SAS-6 proteins levels were not elevated at this timepoint, SAS-6 is unlikely to be the driver of such potential overduplication. We think that SAS-6 protein levels increase is reflective of additional daughter centrioles that are already present at end of the second mitotic division rather than the cause of their formation. Surprisingly, we also find that ZYG-1 levels are decreased at the 2-cell stage.

ZYG-1 acts upstream of SAS-6 and a physical interaction between the two, but not ZYG-1 kinase activity, is required for SAS-6 recruitment. Given SSNA-1's genetic interaction with ZYG-1, as ZYG-1 protein levels decreased when SSNA-1 was deleted, along with the likely overduplication defect, we think that SSNA-1 is playing both positive and negative roles in centriole assembly, such that it positively regulates ZYG-1 levels and negatively regulates additional daughter centriole formation. In line with this idea, we find that SSNA-1 and ZYG-1 biochemically interact *in vitro*. Downstream, ZYG-1 and SPD-2 can interact, through a conserved mechanism across species, and progress centriole biogenesis. The human ortholog of SPD-2, Cep192, and its cooperation with Cep152 is required for the recruitment of Plk4. However, in *Drosophila* Plk4 is targeted to the centrosome by Asterless/Cep152. Considering these mechanisms, *C. elegans* lack a Cep152/Asterless ortholog [59-62] and it is possible that SSNA-1 may play a role analogous to Cep152 cooperating with SPD-2 in ZYG-1 recruitment to or retention at the centriole.

In various eukaryotic organisms, the centriole pair is held together by a proteinaceous linker that is cleaved near the onset of mitosis, thereby allowing the centrosomes to migrate away from one another and set up the mitotic spindle. This linker, however, has not been shown at the centrosome in *C. elegans*. Centrioles undergo two rounds of duplication in the zygote, with

the first occurring during meiotic exit following fertilization and then the second being at the end of the first mitosis. The first centriole duplication event is controlled by separase and cohesin [137]. However, those two proteins do not play a significant role in centriole separation beyond meiosis and the next duplications occurring during mitotic divisions are instead mediated by microtubule pulling forces. These forces will act on a disassembling PCM, that in turn leads to mother and daughter centrioles moving away from one another and initiation of a new round of duplication. We find that multipolar spindles become apparent during the third mitotic division at the 4-cell stage, indicating that a potential overduplication event likely occurred during this second round of centriole duplication at the end of the first mitotic division. Given that SSNA-1 oligomerization is required for its function in the embryo, and taking all the *in vivo* data into account, it is intriguing to speculate that SSNA-1 self-assembles at the site of daughter assembly following the second duplication initiation, creates a scaffold-like structure, and acts as a linker of sorts between mother and daughter centrioles. Without SSNA-1 in the cell, the newly forming daughter is at risk of premature separation thereby leading to an additional round of centriole duplication.

7 Outlook

In this study, SSNA-1 has been characterized as a centriolar component in *C. elegans*, which is directly involved in regulating the proper centriole formation. Enhanced understanding of the molecular processes governing the number, structure, and function of centrioles can be significant for comprehending diseases connected to centrosome dysfunctions and designing potential therapeutic solutions.

In order to shed light on those mechanisms, further investigations will be required to identify how SSNA-1 is spatially and temporally regulated into the cellular context, as well as its precise involvement into the dynamic process of centriole assembly. Given the technical difficulties of employing SSNA-1 for live imaging, which concern the potential disruption of its molecular activity using engineering constructs, *in vitro* reconstitution and structural biology might provide useful insights. Deciphering SSNA-1 binding partners and precise mode of interaction will give new information into centriole formation, its relative molecular architecture, and additional clues about the highly regulated process of spindle formation. Other approaches, such as proteomic analysis, expansion microscopy, and cryo-ET might give us complementary considerations helping us clarifying SSNA-1 post-translational modifications, unknown binding partners and the exact molecular machineries involved in the cellular context. Previous studies have reported how centrosomal proteins can be conserved, absent, or divergent in different species. Taking these findings into consideration, it will be essential to address whether SSNA-1 would conserve its molecular and biological functions that we found in *C. elegans* throughout different organisms, including humans. For instance, the employment of genetic engineering approaches to create knock-out cell lines and/or cell lines with diverse SSNA-1 constructs, combined to *in vitro* reconstitution investigations, might give us a better understanding of such convergence/divergence of centrosomal proteins.

Although few articles have observed SSNA-1 at centrosomes, the SSNA-1 protein family was also reported to localize at cilia, flagella, and midbodies, in dividing cells, as well as axon branching points, in neurons. These studies underscore a versatile and complex regulation of SSNA-1. Hence, it will also be interesting to understand how SSNA-1 is regulated in different cellular processes, considering both centrosomal and non-centrosomal microtubule organizing centers.

8 References

1. Desai, A. & Mitchison, T. J. Microtubule polymerization dynamics. Annu. Rev. Cell Dev. Biol. 13, 83–117 (1997).

2. Hall, A. The cytoskeleton and cancer. Cancer Metastasis Rev 28, 5–14 (2009).

3. Sharp, D. J. & Ross, J. L. Microtubule-severing enzymes at the cutting edge. J. Cell Sci. 125, 2561–2569 (2012).

4. Petry, S., Groen, A. C., Ishihara, K., Mitchison, T. J. & Vale, R. D. Branching microtubule nucleation in Xenopus egg extracts mediated by augmin and TPX2. Cell 152, 768–777 (2013).

5. Maiato, H., Rieder, C. L. & Khodjakov, A. Kinetochore-driven formation of kinetochore fibers contributes to spindle assembly during animal mitosis. J. Cell Biol. 167, 831–840 (2004).

6. Heald, R. et al. Self-organization of microtubules into bipolar spindles around artificial chromosomes in Xenopus egg extracts. Nature 382, 420–425 (1996).

7. Petry S, Vale RD. Microtubule nucleation at the centrosome and beyond. Nat Cell Biol. 17(9):1089-93 (2015).

8. Tassin, A. M., Maro, B. & Bornens, M. Fate of microtubule-organizing centers during myogenesis in vitro. J. Cell Biol. 100, 35–46 (1985)

9. Chabin-Brion, K. et al. The Golgi complex is a microtubule-organizing organelle. Mol. Biol. Cell 12, 2047–2060 (2001).

10. Efimov, A. et al. Asymmetric CLASP-dependent nucleation of noncentrosomal microtubules at the trans-Golgi network. Dev. Cell 12, 917–930 (2007).

11. Murata, T. et al. Microtubule-dependent microtubule nucleation based on recruitment of gamma-tubulin in higher plants. Nat. Cell Biol. 7, 961–968 (2005).

12. Janson, M. E., Setty, T. G., Paoletti, A. & Tran, P. T. Efficient formation of bipolar microtubule bundles requires microtubule-bound γ-tubulin complexes. J. Cell Biol. 169, 297–308 (2005).

13. Mogensen, M. M. & Tucker, J. B. Evidence for microtubule nucleation at plasma membrane-associated sites in Drosophila. J. Cell Sci. 88, 95–107 (1987).

14. Anna Akhmanova & Michel O. Steinmetz. Control of microtubule organization and dynamics: two ends in the limelight. Nature Reviews Molecular Cell Biology volume 16, pages 711–726 (2015).

15. Florian S., Mitchison T.J. Anti-Microtubule Drugs. The Mitotic Spindle. Methods in Molecular Biology, vol 1413. (2016).

16. Brouhard, G.J., Rice, L.M. Microtubule dynamics: an interplay of biochemistry and mechanics. Nat Rev Mol Cell Biol 19, 451–463 (2018).

17. Wade et al., new data on the microtubule surface lattice. Elsevier (1991).

18. Haixin Sui, Kenneth H. Downing, Structural Basis of Interprotofilament Interaction and Lateral Deformation of Microtubules. Structure, Volume 18, Issue 8, (2010).

19. Alexander D. Cook, Szymon W. Manka, Su Wang, Carolyn A. Moores, Joseph Atherton, A microtubule RELION-based pipeline for cryo-EM image processing. Journal of Structural Biology, Volume 209, Issue 1 (2020).

20. Goodson HV, Jonasson EM. Microtubules and Microtubule-Associated Proteins. Cold Spring Harb Perspect Biol 10(6):a022608 (2018).

21. Dehmelt, L., & Halpain, S. (2005). The MAP2/Tau family of microtubule-associated proteins. Genome biology, 6(1), 204.

22. Roll-Mecak, A., and McNally, F.J. (2010). Microtubule-severing enzymes. Current Opinion in Cell Biology 22, 96–103

23. Maurer, S.P., Fourniol, F.J., Bohner, G., Moores, C.A., and Surrey, T. (2012). EBs Recognize a Nucleotide- Dependent Structural Cap at Growing Microtubule Ends. Cell 149, 371–382.

24. Zanic, M., Stear, J.H., Hyman, A.A., and Howard, J. (2009). EB1 Recognizes the Nucleotide State of Tubulin in the Microtubule Lattice. PLoS ONE 4, e7585.

25. Hayashi I, Ikura M. Crystal structure of the amino-terminal microtubule-binding domain of end-binding protein 1 (EB1). J Biol Chem. 2003 Sep 19;278(38):36430-4. doi: 10.1074/jbc.M305773200. Epub 2003 Jul 11. PMID: 12857735.,

26. De Groot, C.O., Jelesarov, I., Damberger, F.F., Bjelić, S., Schärer, M.A., Bhavesh, N.S., Grigoriev, I., Buey, R.M., Wüthrich, K., Capitani, G., et al. (2010). Molecular insights into mammalian end-binding protein heterodimerization. J. Biol. Chem. 285, 5802–5814.

27. Akhmanova, A., and Steinmetz, M.O. (2008). Tracking the ends: a dynamic protein network controls the fate of microtubule tips. Nature Publishing Group 9, 309–322.

28. Weisbrich, A., Honnappa, S., Jaussi, R., Okhrimenko, O., Frey, D., Jelesarov, I., Akhmanova, A., and Steinmetz, M.O. (2007). Structure-function relationship of CAP-Gly domains. Nat Struct Mol Biol 14, 959–967.

29. Kumar, P., and Wittmann, T. (2012). +TIPs: SxIPping along microtubule ends. Trends in Cell Biology 22, 418–428.

30. Al-Bassam, J., Larsen, N.A., Hyman, A.A., and Harrison, S.C. (2007). Crystal Structure of a TOG Domain: Conserved Features of XMAP215/Dis1-Family TOG Domains and Implications for Tubulin Binding. Structure 15, 355–362.

31. Slep, K.C. (2009). The role of TOG domains in microtubule plus end dynamics.

32. Geyer, E.A., Burns, A., Lalonde, B.A., Ye, X., Elife, F.P., 2015 (2015). A mutation uncouples the tubulin conformational and GTPase cycles, revealing allosteric control of microtubule dynamics.

33. Kollman, J. M., Merdes, A., Mourey, L. & Agard, D. A.Microtubule nucleation by γ-tubulin complexes. Nat. Rev. Mol. Cell Biol. 12, 709–721 (2011).

34. Wiese, C., and Zheng, Y. (2000). A new function for the γ -tubulin ring complex as A microtubule minus- end cap. Nature Cell Biology 2, 358–364.

35. Thawani, A., & Petry, S. (2021). Molecular insight into how γ-TuRC makes microtubules. Journal of cell science, 134(14), jcs245464.

36. Petry, S., Groen, A.C., Ishihara, K., Mitchison, T.J., and Vale, R.D. (2013). Branching Microtubule Nucleation in Xenopus Egg Extracts Mediated by Augmin and TPX2. Cell 152, 768–777.

37. Akhmanova, A., and Steinmetz, M.O. (2019). Microtubule minus-end regulation at a glance. JCell Sci 132, jcs227850.

38. Akhmanova, A., and Hoogenraad, C.C. (2015). Microtubule Minus-End-Targeting Proteins Review. Current Biology 25, R162–R171.

39. Baines, A.J., Bignone, P.A., biology, M.K.M., 2009 The CKK Domain (DUF1781) Binds Microtubules and Defines the CAMSAP/ssp4 Family of Animal Proteins. Academic.Oup.com

40. Jiang, K., Hua, S., Mohan, R., Grigoriev, I., Yau, K.W., Liu, Q., Katrukha, E.A., Altelaar, A.F.M., Heck, A.J.R., Hoogenraad, C.C., et al. (2014). Microtubule Minus-End Stabilization by Polymerization-Driven CAMSAP Deposition. Developmental Cell 28, 295–309.

41. Meunier, S., Shvedunova, M., Van Nguyen, N., Avila, L., Vernos, I., and Akhtar, A. (2015). An epigenetic regulator emerges as microtubule minus-end binding and stabilizing factor in mitosis. Nature Communications 6, 1–10.

42. Lin, T. C., Neuner, A., & Schiebel, E., Targeting of γ-tubulin complexes to microtubule organizing centers: conservation and divergence. Trends in cell biology, 25(5), 296–307 (2015).

43. Wu J, Akhmanova A. Microtubule-Organizing Centers. Annu Rev Cell Dev 33:51-75 (2017).

44. Mi Hye Song, Nicholas B Miliaras, Nina Peel, Kevin F O'Connell, Centrioles: some self-assembly required. Current Opinion in Cell Biology, Volume 20, Issue 6, (2008).

45. Dong Gang, Building a ninefold symmetrical barrel: structural dissections of centriole assembly. Open Biol.5150082150082 (2015).

46. Magescas J, Zonka JC, Feldman JL. A two-step mechanism for the inactivation of microtubule organizing center function at the centrosome. Elife. 2019 Jun 27;8:e47867. doi: 10.7554/eLife.47867. PMID: 31246171; PMCID: PMC6684319.

47. Nigg EA., Origins and consequences of centrosome aberrations in human cancers. Int. J. Cancer 119, 2717–2723 (2006).

48. Satir P, Christensen ST. Overview of structure and function of mammalian cilia. Annu. Rev. Physiol. 69, 377–400 (2007).

49. Bettencourt-Dias M, Hildebrandt F, Pellman D, Woods G, Godinho SA., Centrosomes and cilia in human disease. Trends Genet. 27, 307–315 (2011).

50. Adams M, Smith UM, Logan CV, Johnson CA. Recent advances in the molecular pathology, cell biology and genetics of ciliopathies. J. Med. Genet. 45, 257–267 (2008).

51. O'Connell KF, Caron C, Kopish KR, Hurd DD, Kemphues KJ, Li Y, White JG., The C. elegans zyg-1 gene encodes a regulator of centrosome duplication with distinct maternal and paternal roles in the embryo. Cell 105, 547–558 (2001).

52. Kemp CA, Kopish KR, Zipperlen P, Ahringer J, O'Connell KF., Centrosome maturation and duplication in C. elegans require the coiled-coil protein SPD-2. Dev. Cell6, 511–523 (2004).

53. Pelletier L, Ozlu N, Hannak E, Cowan C, Habermann B, Ruer M, Muller-Reichert T, Hyman AA., The Caenorhabditis elegans centrosomal protein SPD-2 is required for both pericentriolar material recruitment and centriole duplication. Curr. Biol. 14, 863–873 (2004).

54. Kirkham M, Muller-Reichert T, Oegema K, Grill S, Hyman AA., SAS-4 is a C. elegans centriolar protein that controls centrosome size. Cell 112, 575–587 (2003).

55. Leidel S, Gonczy P., SAS-4 is essential for centrosome duplication in C. elegans and is recruited to daughter centrioles once per cell cycle. Dev. Cell 4, 431–439 (2003).

56. Delattre M, Leidel S, Wani K, Baumer K, Bamat J, Schnabel H, Feichtinger R, Schnabel R, Gonczy P., Centriolar SAS-5 is required for centrosome duplication in C. elegans. Nat. Cell Biol. 6, 656–664 (2004).

57. Dammermann A, Muller-Reichert T, Pelletier L, Habermann B, Desai A, Oegema K., Centriole assembly requires both centriolar and pericentriolar material proteins. Dev. Cell 7, 815–829 (2004).

58. Leidel S, Delattre M, Cerutti L, Baumer K, Gonczy P., SAS-6 defines a protein family required for centrosome duplication in C. elegans and in human cells. Nat. Cell Biol. 7, 115–125 (2005).

59. Schwarz, A., Sankaralingam, P., O'Connell, K. F., & Müller-Reichert, T. (2018). Revisiting Centrioles in Nematodes-Historic Findings and Current Topics. Cells, 7(8), 101.

60. Shimanovskaya, E.; Viscardi, V.; Lesigang, J.; Lettman, M.M.; Qiao, R.; Svergun, D.I.; Round, A.; Oegema, K.; Dong, G., Structure of the C. elegans ZYG-1 cryptic polo box suggests a conserved mechanism for centriolar docking of Plk4 kinases. Structure 22, 1090–1104 (2014).

61. Park, S.Y.; Park, J.E.; Kim, T.S.; Kim, J.H.; Kwak, M.J.; Ku, B.; Tian, L.; Murugan, R.N.; Ahn, M.; Komiya, S.; et al. Molecular basis for unidirectional scaffold switching of human Plk4 in centriole biogenesis. Nature structural & molecular biology, 21(8), 696–703 (2014)

62. Sonnen, K.F.; Gabryjonczyk, A.M.; Anselm, E.; Stierhof, Y.D.; Nigg, E.A. Human Cep192 and Cep152 cooperate in Plk4 recruitment and centriole duplication. J. Cell Sci. Journal of cell science, 126(Pt 14), 3223–3233 (2013).

63. Cizmecioglu, O.; Arnold, M.; Bahtz, R.; Settele, F.; Ehret, L.; Haselmann-Weiss, U.; Antony, C.; Hoffmann, I. Cep152 acts as a scaffold for recruitment of Plk4 and CPAP to the centrosome. J. Cell Biol., 191, 731–739 (2010).

64. Kim, T.S.; Park, J.E.; Shukla, A.; Choi, S.; Murugan, R.N.; Lee, J.H.; Ahn, M.; Rhee, K.; Bang, J.K.; Kim, B.Y.; et al. Hierarchical recruitment of Plk4 and regulation of centriole biogenesis by two centrosomal scaffolds, Cep192 and Cep152. Proc. Natl. Acad. Sci. USA, 110, E4849–E4857 (2013).

65. Stevens, N.R.; Dobbelaere, J.; Brunk, K.; Franz, A.; Raff, J.W. Drosophila Ana2 is a conserved centriole duplication factor. J. Cell Biol., 188, 313–323 (2010).

66. Stevens, N.R.; Roque, H.; Raff, J.W. D Sas-6 and Ana2 coassemble into tubules to promote centriole duplication and engagement. Dev. Cell, 19, 913–919 (2010).

67. Vulprecht, J.; David, A.; Tibelius, A.; Castiel, A.; Konotop, G.; Liu, F.; Bestvater, F.; Raab, M.S.; Zentgraf, H.; Izraeli, S.; et al. Stil is required for centriole duplication in human cells. J. Cell Sci., 125, 1353–1362 (2012).

68. Lettman, M.M.; Wong, Y.L.; Viscardi, V.; Niessen, S.; Chen, S.H.; Shiau, A.K.; Zhou, H.; Desai, A.; Oegema, K. Direct binding of SAS-6 to ZYG-1 recruits SAS-6 to the mother centriole for cartwheel assembly. Dev. Cell, 25, 284–298 (2013).

69. Dzhindzhev, N.S.; Tzolovsky, G.; Lipinszki, Z.; Schneider, S.; Lattao, R.; Fu, J.; Debski, J.; Dadlez, M.; Glover, D.M. Plk4 phosphorylates Ana2 to trigger Sas6 recruitment and procentriole formation. Curr. Biol., 24, 2526–2532 (2014).

70. Ohta, M.; Ashikawa, T.; Nozaki, Y.; Kozuka-Hata, H.; Goto, H.; Inagaki, M.; Oyama, M.; Kitagawa, D. Direct interaction of Plk4 with STIL ensures formation of a single procentriole per parental centriole. Nat. Commun., 5, 5267 (2014).

71. Kratz, A.S.; Barenz, F.; Richter, K.T.; Hoffmann, I. Plk4-dependent phosphorylation of STIL is required for centriole duplication. Biol. Open, 4, 370–377 (2015).

72. Moyer, T.C.; Clutario, K.M.; Lambrus, B.G.; Daggubati, V.; Holland, A.J. Binding of STIL to Plk4 activates kinase activity to promote centriole assembly. J. Cell Biol., 209, 863–878 (2015).

73. McLamarrah, T.A.; Buster, D.W.; Galletta, B.J.; Boese, C.J.; Ryniawec, J.M.; Hollingsworth, N.A.; Byrnes, A.E.; Brownlee, C.W.; Slep, K.C.; Rusan, N.M.; et al. An ordered pattern of Ana2 phosphorylation by Plk4 is required for centriole assembly. J. Cell Biol., 217, 1217–1231 (2018).

74. Ohta, M.; Watanabe, K.; Ashikawa, T.; Nozaki, Y.; Yoshiba, S.; Kimura, A.; Kitagawa, D. Bimodal binding of STIL to Plk4 controls proper centriole copy number. Cell Rep., 23, 3160–3169 (2018).

75. Pelletier, L.; O'Toole, E.; Schwager, A.; Hyman, A.A.; Müller-Reichert, T. Centriole assembly in Caenorhabditis elegans. Nature 2006, 444, 619–623.

76. Delattre, M.; Canard, C.; Gonczy, P. Sequential protein recruitment in C. elegans centriole formation. Curr. Biol. 16, 1844–1849 (2006).

77. Kirkham, M.; Müller-Reichert, T.; Oegema, K.; Grill, S.; Hyman, A.A. SAS-4 is a C. elegans centriolar protein that controls centrosome size. Cell , 112, 575–587 (2003).

78. Leidel, S.; Gonczy, P. SAS-4 is essential for centrosome duplication in C. elegans and is recruited to daughter centrioles once per cell cycle. Dev. Cell , 4, 431–439 (2003).

79. Basto, R.; Lau, J.; Vinogradova, T.; Gardiol, A.; Woods, C.G.; Khodjakov, A.; Raff, J.W. Flies without centrioles. Cell , 125, 1375–1386 (2006).

80. Gopalakrishnan, J.; Mennella, V.; Blachon, S.; Zhai, B.; Smith, A.H.; Megraw, T.L.; Nicastro, D.; Gygi, S.P.; Agard, D.A.; Avidor-Reiss, T. Sas-4 provides a scaffold for cytoplasmic complexes and tethers them in a centrosome. Nat. Commun. , 2, 359 (2011).

81. Zheng, X.; Gooi, L.M.; Wason, A.; Gabriel, E.; Mehrjardi, N.Z.; Yang, Q.; Zhang, X.; Debec, A.; Basiri, M.L.; Avidor-Reiss, T.; et al. Conserved TCP domain of Sas-4/CPAP is essential for pericentriolar material tethering during centrosome biogenesis. Proc. Natl. Acad. Sci. USA , 111, E354–363 (2014).

82. Zhao, L.; Jin, C.; Chu, Y.; Varghese, C.; Hua, S.; Yan, F.; Miao, Y.; Liu, J.; Mann, D.; Ding, X.; et al. Dimerization of CPAP orchestrates centrosome cohesion plasticity. J. Biol. Chem., 285, 2488–2497 (2010).

83. Cottee, M.A.; Muschalik, N.; Wong, Y.L.; Johnson, C.M.; Johnson, S.; Andreeva, A.; Oegema, K.; Lea, S.M.; Raff, J.W.; van Breugel, M. Crystal structures of the CPAP/STIL complex reveal its role in centriole assembly and human microcephaly. Elife, 2, e01071 (2013).

84. Hung, L.Y.; Chen, H.L.; Chang, C.W.; Li, B.R.; Tang, T.K. Identification of a novel microtubule-destabilizing motif in CPAP that binds to tubulin heterodimers and inhibits microtubule assembly. Mol. Biol. Cell, 15, 2697–2706 (2004).

85. Cormier, A.; Clement, M.J.; Knossow, M.; Lachkar, S.; Savarin, P.; Toma, F.; Sobel, A.; Gigant, B.; Curmi, P.A. The PN2-3 domain of centrosomal P4.1-associated protein implements a novel mechanism for tubulin sequestration. J. Biol. Chem., 284, 6909–6917 (2009).

86. Bianchi, S.; Rogala, K.B.; Dynes, N.J.; Hilbert, M.; Leidel, S.A.; Steinmetz, M.O.; Gonczy, P.; Vakonakis, I. Interaction between the Caenorhabditis elegans centriolar protein SAS-5 and microtubules facilitates organelle assembly. Mol. Biol. Cell , 29, 722–735 (2018).

87. Hatzopoulos, G.N.; Erat, M.C.; Cutts, E.; Rogala, K.B.; Slater, L.M.; Stansfeld, P.J.; Vakonakis, I. Structural analysis of the G-box domain of the microcephaly protein CPAP suggests a role in centriole architecture. Structure , 21, 2069–2077 (2013).

88. Kong, D.; Farmer, V.; Shukla, A.; James, J.; Gruskin, R.; Kiriyama, S.; Loncarek, J. Centriole maturation requires regulated Plk1 activity during two consecutive cell cycles. J. Cell Biol. , 206, 855–865 (2014).

89. Sugioka, K.; Hamill, D.R.; Lowry, J.B.; McNeely, M.E.; Enrick, M.; Richter, A.C.; Kiebler, L.E.; Priess, J.R.; Bowerman, B. Centriolar SAS-7 acts upstream of SPD-2 to regulate centriole assembly and pericentriolar material formation. Elife , 6, e20353 (2017).

90. Novak, Z.A.; Conduit, P.T.; Wainman, A.; Raff, J.W. Asterless licenses daughter centrioles to duplicate for the first time in Drosophila embryos. Curr. Biol. , 24, 1276–1282 (2014).

91. Viswanadha, R., Sale, W.S., and Porter, M.E. (2017). Ciliary Motility: Regulation of Axonemal Dynein Motors. Cold Spring Harb Perspect Biol 9, a018325–24.

92. Carvalho-Santos, Z., Azimzadeh, J., Pereira-Leal, J.B., and Bettencourt-Dias, M. (2011). Tracing the origins of centrioles, cilia, and flagella. J Cell Biol 194, 165–175.

93. Alberts B, Johnson A, Lewis J, et al. Molecular Biology of the Cell. 4th edition. New York: Garland Science; 2002. Mitosis. Available from: https://www.ncbi.nlm.nih.gov/books/NBK26934/#

94. Petry, S., and Vale, R.D. (2015). Microtubule nucleation at the centrosome and beyond. Nature Cell Biology 17, 1089–1093.

95. Prosser, S.L., and Pelletier, L. (2017). Mitotic spindle assembly in animal cells: a fine balancing act. Nature Publishing Group 18, 187–201

96. Dionne, L.K., Wang, X.-J., and Prekeris, R. (2015). Midbody: from cellular junk to regulator of cell polarity and cell fate. Current Opinion in Cell Biology 35, 51–58.

97. Basnet, N., Nedozralova, H., Crevenna, A.H. et al. Direct induction of microtubule branching by microtubule nucleation factor SSNA1. Nat Cell Biol 20, 1172–1180 (2018).

98. Ramos-Morales, F., Infante, C., Fedriani, C., Bornens, M., & Rios, R. M. NA14 is a novel nuclear autoantigen with a coiled-coil domain. The Journal of biological chemistry, 273(3), 1634–1639 (1998).

99. Nozawa, K., Ikeda, K., Satoh, M., Reeves, W. H., Stewart, C. M., Li, Y. C., Yen, T. J., Rios, R. M., Takamori, K., Ogawa, H., Sekigawa, I., Takasaki, Y., & Chan, E. K. Autoantibody to NA14 is an independent marker primarily for Sjogren's syndrome. Frontiers in bioscience (Landmark edition), 14(10), 3733–3739 (2009)

100. Fox R. I. Sjögren's syndrome. Lancet (London, England), 366(9482), 321–331 (2005).

101. Lévêque, M. F., Berry, L., & Besteiro, S. An evolutionarily conserved SSNA1/DIP13 homologue is a component of both basal and apical complexes of Toxoplasma gondii. Scientific reports, 6, 27809 (2016).

102. Pfannenschmid, F., Wimmer, V. C., Rios, R. M., Geimer, S., Kröckel, U., Leiherer, A., Haller, K., Nemcová, Y., & Mages, W. Chlamydomonas DIP13 and human NA14: a new class of proteins associated with microtubule structures is involved in cell division. Journal of cell science, 116(Pt 8), 1449–1462 (2003).

103. Rodríguez-Rodríguez, M., Treviño, M. A., Laurents, D. V., Arranz, R., Valpuesta, J. M., Rico, M., Bruix, M., & Jiménez, M. A. Characterization of the structure and self-recognition of the human centrosomal protein NA14: implications for stability and function. Protein engineering, design & selection : PEDS, 24(12), 883–892 (2011).

104. Price HP, Hodgkinson MR, Curwen RS, MacLean LM, Brannigan JA, Carrington M, et al. The Orthologue of Sjögren's Syndrome Nuclear Autoantigen 1 (SSNA1) in Trypanosoma brucei Is an Immunogenic Self-Assembling Molecule. PLoS ONE 7(2): e31842 (2012).

105. Goyal, U., Renvoisé, B., Chang, J., & Blackstone, C. Spastin-interacting protein NA14/SSNA1 functions in cytokinesis and axon development. PloS one, 9(11), e112428 (2014).

106. Janke C. The tubulin code: molecular components, readout mechanisms, and functions. The Journal of cell biology, 206(4), 461–472 (2014).

107. Lawrence, E. J., Arpag, G., Arnaiz, C., & Zanic, M. SSNA1 stabilizes dynamic microtubules and detects microtubule damage. eLife, 10, e67282 (2021).

108. W.M. Stanley, Thomas F. Anderson, Electron micrographs of protein molecules, Journal of Biological Chiemistry, Volume 146, Issue 1 (1942)

109. Harris J. R. (2015). Transmission electron microscopy in molecular structural biology: A historical survey. Archives of biochemistry and biophysics, 581, 3–18.

110. Brenner, S., & Horne, R. W. (1959). A negative staining method for high resolution electron microscopy of viruses. Biochimica et biophysica acta, 34, 103–110.

111. De Carlo, S., & Harris, J. R. (2011). Negative staining and cryo-negative staining of macromolecules and viruses for TEM. Micron (Oxford, England : 1993), 42(2), 117–131.

112. Dubochet, J., Lepault, J., Freeman, R., Berriman, J.A., Homo, J.-C., Electron microscopy of frozen water and acqueous solutions, (1982) Blackwell Science Ltd

113. Orlova EV, Saibil HR. Structural analysis of macromolecular assemblies by electron microscopy. Chem Rev. 2011 Dec 14;111(12):7710-48. doi: 10.1021/cr100353t. Epub 2011 Sep 16. PMID: 21919528; PMCID: PMC3239172.

114. Egelman EH. A robust algorithm for the reconstruction of helical filaments using single-particle methods. Ultramicroscopy. 2000 Dec;85(4):225-34. doi: 10.1016/s0304-3991(00)00062-0. PMID: 11125866.

115. De Rosier, D. J., & Klug, A. (1968). Reconstruction of three dimensional structures from electron micrographs. Nature, 217(5124), 130–134.

116. Kühlbrandt W. (2014). Biochemistry. The resolution revolution. Science (New York, N.Y.), 343(6178), 1443–1444.

117. Chung J, Kim HM. The Nobel Prize in Chemistry 2017: High-Resolution Cryo-Electron Microscopy. AM 2017;47;218-222

118. Yip, K. M., Fischer, N., Paknia, E., Chari, A., & Stark, H. (2020). Atomic-resolution protein structure determination by cryo-EM. Nature, 587(7832), 157–161.

119. Gibson, D. G., Young, L., Chuang, R. Y., Venter, J. C., Hutchison, C. A., 3rd, & Smith, H. O. (2009). Enzymatic assembly of DNA molecules up to several hundred kilobases. Nature methods, 6(5), 343–345.

120. Shelanski, M. L., Gaskin, F. & Cantor, C. R. Microtubule assembly in the absence of added nucleotides. Proc. Natl Acad. Sci. USA 70, 765–768 (1973)

121. Paolo Di Tommaso, Sebastien Moretti, Ioannis Xenarios, Miquel Orobitg, Alberto Montanyola, Jia-Ming Chang, Jean-François Taly, Cedric Notredame, T-Coffee: a web server for the multiple sequence alignment of protein and RNA sequences using structural information and homology extension, Nucleic Acids Research, Volume 39, Issue suppl_2, 1 July 2011, Pages W13–W17

122. Jumper J, Evans R, Pritzel A, Green T, Figurnov M, Ronneberger O, Tunyasuvunakool K, Bates R, Žídek A, Potapenko A, Bridgland A, Meyer C, Kohl SAA, Ballard AJ, Cowie A, Romera-Paredes B, Nikolov S, Jain R, Adler J, Back T, Petersen S, Reiman D, Clancy E, Zielinski M, Steinegger M, Pacholska M, Berghammer T, Bodenstein S, Silver D, Vinyals O, Senior AW, Kavukcuoglu K, Kohli P, Hassabis D. Highly accurate protein structure prediction with AlphaFold. Nature. 2021 Aug;596(7873):583-589.

doi: 10.1038/s41586-021-03819-2. Epub 2021 Jul 15. PMID: 34265844; PMCID: PMC8371605.

123. Punjani, A., Rubinstein, J., Fleet, D. et al. cryoSPARC: algorithms for rapid unsupervised cryo-EM structure determination. Nat Methods 14, 290–296 (2017).

124. Schindelin J, Arganda-Carreras I, Frise E, Kaynig V, Longair M, Pietzsch T, Preibisch S, Rueden C, Saalfeld S, Schmid B, Tinevez JY, White DJ, Hartenstein V, Eliceiri K, Tomancak P, Cardona A. Fiji: an open-source platform for biological-image analysis. Nat Methods. 2012 Jun 28;9(7):676-82.

125. Pettersen EF, Goddard TD, Huang CC, Meng EC, Couch GS, Croll TI, Morris JH, Ferrin TE. UCSF ChimeraX: Structure visualization for researchers, educators, and developers. Protein Sci. 2021 Jan;30(1):70-82. doi: 10.1002/pro.3943. Epub 2020 Oct 22. PMID: 32881101; PMCID: PMC7737788.

126. Emsley P, Lohkamp B, Scott WG, Cowtan K. Features and development of Coot. Acta Crystallogr D Biol Crystallogr. 2010 Apr;66(Pt 4):486-501. doi: 10.1107/S0907444910007493. Epub 2010 Mar 24. PMID: 20383002; PMCID: PMC2852313.

127. Liebschner D, Afonine PV, Baker ML, Bunkóczi G, Chen VB, Croll TI, Hintze B, Hung LW, Jain S, McCoy AJ, Moriarty NW, Oeffner RD, Poon BK, Prisant MG, Read RJ, Richardson JS, Richardson DC, Sammito MD, Sobolev OV, Stockwell DH, Terwilliger TC, Urzhumtsev AG, Videau LL, Williams CJ, Adams PD. Macromolecular structure determination using X-rays, neutrons and electrons: recent developments in Phenix. Acta Crystallogr D Struct Biol. 2019 Oct 1;75(Pt 10):861-877. doi: 10.1107/S2059798319011471. Epub 2019 Oct 2. PMID: 31588918; PMCID: PMC6778852.

128. Wallace AC, Laskowski RA, Thornton JM. LIGPLOT: a program to generate schematic diagrams of protein-ligand interactions. Protein Eng. 1995 Feb;8(2):127-34. doi: 10.1093/protein/8.2.127. PMID: 7630882.

129. Iyer J, DeVaul N, Hansen T, Nebenfuehr B (2019) Using Microinjection to Generate Genetically Modified Caenorhabditis elegans by CRISPR/Cas9 Editing. Methods Mol Biol 1874:431–457.

130. Paix A, Folkmann A, Rasoloson D, Seydoux G (2015) High Efficiency, Homology-Directed Genome Editing in Caenorhabditis elegans Using CRISPR-Cas9 Ribonucleoprotein Complexes. Genetics 201 (1):47–54.

131. O'Connell KF, Golden A (2014) Confocal imaging of the microtubule cytoskeleton in C. elegans embryos and germ cells. Methods Mol Biol 1075:257–272.

132. Kapoor S, Kotak S. Centrosome Aurora A gradient ensures single polarity axis in C. elegans embryos. Biochem Soc Trans. 2020 Jun 30;48(3):1243-1253.

133. Zorba A, Buosi V, Kutter S, Kern N, Pontiggia F, Cho YJ, Kern D. Molecular mechanism of Aurora A kinase autophosphorylation and its allosteric activation by TPX2. Elife. 2014 May 27;3:e02667.

134. Woodruff JB, Ferreira Gomes B, Widlund PO, Mahamid J, Honigmann A, Hyman AA. The Centrosome Is a Selective Condensate that Nucleates Microtubules by Concentrating Tubulin. Cell. 2017 Jun 1;169(6):1066-1077.e10.

135. Hori A, Toda T. Regulation of centriolar satellite integrity and its physiology. Cell Mol Life Sci. 2017 Jan;74(2):213-229.

136. Tollenaere MA, Mailand N, Bekker-Jensen S. Centriolar satellites: key mediators of centrosome functions. Cell Mol Life Sci. 2015 Jan;72(1):11-23.

137. Cabral G, Sans SS, Cowan CR, Dammermann A. Multiple mechanisms contribute to centriole separation in C. elegans. Curr Biol. 2013 Jul 22;23(14):1380-7.

138. Peel N, Stevens NR, Basto R, Raff JW. Overexpressing centriole-replication proteins in vivo induces centriole overduplication and de novo formation. Curr Biol. 2007 May 15;17(10):834-43. doi: 10.1016/j.cub.2007.04.036. Epub 2007 May 3. PMID: 17475495; PMCID: PMC1885955.

139. Holland AJ, Lan W, Niessen S, Hoover H, Cleveland DW. Polo-like kinase 4 kinase activity limits centrosome overduplication by autoregulating its own stability. J Cell Biol. 2010 Jan 25;188(2):191-8. doi: 10.1083/jcb.200911102. PMID: 20100909; PMCID: PMC2813471.

140. Miller JG, Liu Y, Williams CW, Smith HE, O'Connell KF. The E2F-DP1 Transcription Factor Complex Regulates Centriole Duplication in Caenorhabditis elegans. G3 (Bethesda). 2016 Jan 15;6(3):709-20. doi: 10.1534/g3.115.025577. PMID: 26772748; PMCID: PMC4777132.

141. Peel N, Iyer J, Naik A, Dougherty MP, Decker M, O'Connell KF. Protein Phosphatase 1 Down Regulates ZYG-1 Levels to Limit Centriole Duplication. PLoS Genet. 2017 Jan 19;13(1):e1006543. doi: 10.1371/journal.pgen.1006543. PMID: 28103229; PMCID: PMC5289615.

142. Piel M, Meyer P, Khodjakov A, Rieder CL, Bornens M. The respective contributions of the mother and daughter centrioles to centrosome activity and behavior in vertebrate cells. J Cell Biol. 2000 Apr 17;149(2):317-30. doi: 10.1083/jcb.149.2.317. PMID: 10769025; PMCID: PMC2175166.

143. Duensing A, Liu Y, Perdreau SA, Kleylein-Sohn J, Nigg EA, Duensing S. Centriole overduplication through the concurrent formation of multiple daughter centrioles at single maternal templates. Oncogene. 2007 Sep 20;26(43):6280-8. doi: 10.1038/sj.onc.1210456. Epub 2007 Apr 16. PMID: 17438528; PMCID: PMC2586811.

Acknowledgements

I thank and express my gratitude to Dr. Naoko Mizuno for believing in me and offering the opportunity to pursue my career goals. Her support influenced positively my research and ultimately my personal ambitions. I particularly appreciate Naoko's mentorship and constructive criticism that oftentimes was greater than my expectations. I also thank Dr. Christian Biertümpfel. He always helped and supported me with endless recommendations to tackle everyday problems and scientific goals. I would like to thank my PhD supervisor Prof. Dr. Veit Hornung. He allowed me to progress my career as international student. Extended thanks also go to Prof. Dr. Elena Conti, for accepting the role of being my additional supervisor, as well as my thesis advisory committee.

I thank my research collaborators Dr. Jason Pfister and Dr. Kevin O'Connell. They partnered with my research project and such joint effort improved the quality of my research and professional skills. My gratitude also goes to all the people in the core facilities at the NIH and MPI of Biochemistry for their technical support. Many thanks to Dr. Ulrich Baxa (MICEF Cryo-Electron Microscopy Core), Dr. Di Wu, Dr. Grzegorz Piszczek (NHLBI Biophysics Core Facility), and Dr. Duck-Yeon Lee (NHLBI Biochemistry Core). Thanks to my past and present colleagues Nirakar, Satish, Chris, Scott, Ryan, Keni, Victor, Yurika, Pelayo, Sophie, Julia, Thien, John, Jienyu, and King.

I thank my family very much, as well as my relatives, for their unwavering love and emotional support. A special thanks to my wonderful nieces, Gaia Luna and Francesca. You all have been my safe space and comfort, and none of this would have been possible without you.

Thanks to my friends Lawrence and Lorenzo S. Your support has been essential in US. Extended thanks also go to my lifelong friends Luca, Dunia, Euplio, Lorenzo S., Adamo, Giuseppe, Lorenzo B., Matteo M., Marco, Matteo D. C., Mattia, Andrea, Stefano, Lorenzo S., Francesca, and Piero. Despite the distance, you have always been there for me.